

PREDICTING GAS-SOLID BUBBLING BED FLOWS USING CONTINUUM MODELING

By

DEEPAK RANGARAJAN

A DISSERTATION PRESENTED TO THE GRADUATE SCHOOL
OF THE UNIVERSITY OF FLORIDA IN PARTIAL FULFILLMENT
OF THE REQUIREMENTS FOR THE DEGREE OF
DOCTOR OF PHILOSOPHY

UNIVERSITY OF FLORIDA

2012

© 2012 Deepak Rangarajan

ACKNOWLEDGMENTS

Graduate school has been a tremendous learning experience for me, and I am deeply indebted to many people who have made these four years truly unforgettable and enjoyable. My sincere gratitude goes to my advisor, Prof. Jennifer Curtis, for her guidance and support. Her patience and encouragement throughout the program helped me overcome many a hurdle. I would like to thank my research collaborators from University of Michigan, Dr. Alexander Mychkovsky and Prof. Steven Ceccio, for laying the foundations of my research project, providing the experimental facility, and guiding me with the experimental work. I would also like to thank my collaborators from University of New South Wales, Tomo Shiozawa, Dr. Yansong Shen and Prof. Aibing Yu, for guiding me on the blast furnace project and providing computational resources. I would like to extend my gratitude to Dr. Sofiane Benyahia of NETL for helping me with MFIX and entertaining the numerous questions I have had over the last four years. A special thanks to my research group mate, Dr. Yu Guo, for sharing valuable technical discussions which I have been able to benefit from. Finally, I would like to thank my family and all my friends for supporting me throughout the program.

TABLE OF CONTENTS

	<u>page</u>
ACKNOWLEDGMENTS.....	3
LIST OF TABLES.....	7
LIST OF FIGURES.....	8
LIST OF ABBREVIATIONS.....	11
ABSTRACT.....	16
CHAPTER	
1 INTRODUCTION.....	18
Bubbling Fluidized Beds.....	18
Prior Work and Motivation.....	19
Modeling.....	19
Experiment.....	21
Quantifying Pseudo-2D Experimental Arrangement.....	22
Industrial Application.....	22
Thesis Objectives and Outline.....	23
2 EXPERIMENTAL MEASUREMENTS.....	25
Background.....	25
Experimental Setup.....	26
Results and Discussion.....	29
Profiles of Mean Velocity.....	29
Single-Phase Fluctuating Velocity Validation.....	29
Profiles of Fluctuating Velocity.....	30
Discussion of Variation in Centerline Fluctuating Velocity.....	30
Coupling through mean flow variables.....	31
Coupling through fluctuating velocities.....	32
Summary.....	33
3 SINGLE-PHASE NUMERICAL STUDY.....	44
Background.....	44
Simulation Setup.....	48
Validation.....	49
Results.....	50
Analysis and Discussion.....	51
Summary.....	54

4	VALIDATING A GAS-SOLID CONTINUUM MODEL	69
	Background.....	69
	Model Description	72
	Governing Equations.....	72
	Gas-Solid Drag.....	73
	Gas-Phase Stress	74
	Solid-Phase Kinetic and Collisional Stress	74
	Solid-Phase Frictional Stress	76
	Turbulence Interaction.....	78
	Boundary Conditions	79
	Model Summary	80
	Simulation Setup.....	80
	Results and Discussion.....	82
	Study 1: Determining Multiplier in Frictional Pressure Expression	82
	Study 2: Determining Frictional Viscosity Model.....	84
	Study 3: Determining Turbulence Modulation Term	86
	Study 4: Validation of the Final Continuum Model.....	88
	Summary	91
5	INDUSTRIAL APPLICATION.....	114
	Background.....	114
	Model Description	116
	Method of Solution.....	117
	Results and Discussion.....	119
	Jet Inlet Velocity	120
	Particle Diameter.....	121
	Outlet Pressure	121
	Initial Bed Height	122
	Jet Location	122
	Initial Porosity	123
	Particle Downward Extraction.....	124
	Jet Angle	124
	Domain Geometry	125
	Summary	125
6	CONCLUSIONS AND RECOMMENDATIONS.....	136
	Experimental Measurements	136
	Single-Phase Numerical Study	137
	Validating a Gas-Solid Continuum Model	137
	Industrial Application.....	138
APPENDIX		
A	MODEL EQUATIONS FOR CHAPTER 5	140

B EXPERIMENT REPEATABILITY	144
LIST OF REFERENCES	145
BIOGRAPHICAL SKETCH	154

LIST OF TABLES

<u>Table</u>		<u>page</u>
2-1	Experimental cases considered.....	35
2-2	LDV parameters and settings.	35
3-1	Input parameters corresponding to an inlet jet Reynolds number Re_j of 67,344.	56
4-1	Comparison of closure models between MFIX and present study.....	93
4-2	System parameters.	94
4-3	Details of the meshes employed. Arrangement shows “(number of cells) size of each cell”.	95
4-4	Closure for the undetermined terms in each study.	95
4-5	Contribution of unsteady mean velocity to the total fluctuations along the centerline at $y = 100$ mm.	96
5-1	Model parameters specified.....	127
5-2	Physical properties specified.	127
5-3	Operating parameters that were varied.	128

LIST OF FIGURES

<u>Figure</u>	<u>page</u>
2-1	Photograph and description of experimental setup..... 36
2-2	System dimensions. 36
2-3	Mean axial velocity profiles at $y/D_j = 10.87$ for different experimental cases.. 37
2-4	Comparison of fluctuating velocity in the Empty bed, case 1, with single-phase turbulent jet data from literature. 38
2-5	Radial profiles of gas axial fluctuating velocity for different fluidization ratios at different axial locations. 39
2-6	Radial profiles of particle axial fluctuating velocity for different fluidization ratios at different axial locations. 40
2-7	Axial gas fluctuating velocity along the centerline for different experimental cases. 41
2-8	Axial particle fluctuating velocity along the centerline for different experimental cases..... 41
2-9	Variation with different experimental cases.. 42
2-10	Variation in maximum axial velocity for different experimental cases.. 43
3-1	Influence of initial conditions..... 57
3-2	An ideal planar jet..... 58
3-3	Typical laboratory setup. 58
3-4	Simulation domain and boundary conditions. 59
3-5	Validation of k-epsilon model..... 60
3-6	Effect of aspect ratio..... 61
3-7	Momentum budget along the centerline ($y = 0, z = w/2$)..... 63
3-8	Momentum budget along the centerline ($y = 0, z = w/2$)..... 64
3-9	Turbulent energy budget along the centerline ($y = 0, z = w/2$)..... 65
3-10	Turbulent energy budget along the centerline ($y = 0, z = w/2$)..... 66

3-11	Momentum budget at $x = 71h$ and $z = w/2$..	67
3-12	Plot showing the minimum value of AR which can be considered unaffected by bounding wall influence for a given x/h	68
4-1	The significance of turbulent and frictional, stresses relative to drag, in a bubbling fluidized bed with a jet injection.).....	97
4-2	Simulation domain and boundary conditions employed.....	98
4-3	Illustration of mesh arrangement.....	99
4-4	Sensitivity of the fluidization curve to frictional pressure multiplier and final match with experiment.....	100
4-5	Effect of frictional viscosity expression in predicting the fluidization curve. $Fr = 0.05$ Pa.....	100
4-6	Photographs of the experiment at increasing intervals of 1 s. The black portion represents voids and the white portion represents bed particles.....	101
4-7	Gas volume fraction prediction of Savage frictional viscosity.....	102
4-8	Gas volume fraction prediction of Srivastava and Sundaresan frictional viscosity.....	103
4-9	Frictional viscosity values on a log scale for $V_{fl} = V_{mf}$ at $t = 15$ s.....	104
4-10	Influence of gas turbulence modulation term on the gas fluctuating velocity at $y = 100$ mm for $V_{fl} = 0$	105
4-11	Streamwise velocity profiles for single phase jet.....	106
4-12	Streamwise velocity profiles for $V_{fl} = 0$	107
4-13	Streamwise velocity profiles for $V_{fl} = 0.7V_{mf}$	108
4-14	Streamwise velocity profiles for $V_{fl} = V_{mf}$	109
4-15	Streamwise velocity profiles for $V_{fl} = 1.3V_{mf}$	110
4-16	Streamwise velocity profiles for $V_{fl} = 1.5V_{mf}$	111
4-17	Effect of fluidization rate on velocity half-widths at $y = 100$ mm.....	112
4-18	Effect of fluidization rate on streamwise mean velocity along the centerline at $y = 100$ mm.....	112

4-19	Effect of fluidization rate on streamwise fluctuating velocity along the centerline at $y = 100$ mm.	113
5-1	Simulation domain for the lower part of ironmaking blast furnace.	129
5-2	Time evolution of raceway size and shape for the base case.	129
5-3	Flow visualization along the plane $y = 0.5$ m at $t = 2$ s for the base case.	130
5-4	Effect of inlet jet velocity on raceway size and shape.	131
5-5	Effect of particle diameter on raceway size and shape.	131
5-6	Effect of outlet pressure on raceway size and shape.	132
5-7	Effect of initial bed height on raceway size and shape.	132
5-8	Effect of jet location on raceway size and shape.	133
5-9	Effect of initial porosity on raceway size and shape.	133
5-10	Effect of solids downward extraction on raceway size and shape.	134
5-11	Modified simulation domain.	134
B-1	Repeatability in gas fluctuating intensity at $y/D_j = 10.87$ for Case 5, $V_{fl}/V_{mf} = 1.15$	144
B-2	Repeatability in particle fluctuating intensity at $y/D_j = 10.87$ for Case 5, $V_{fl}/V_{mf} = 1.15$	144

LIST OF ABBREVIATIONS

AR	jet nozzle aspect ratio
$C_{1\varepsilon}, C_{2\varepsilon}, C_{3\varepsilon}, C_{\mu}, \sigma_k, \sigma_\varepsilon$	constants in k-epsilon gas turbulence model
C_D	drag coefficient
D_j	inlet jet diameter [m]
d_p	particle diameter [m]
D_p	particle diameter [m]
e	particle-particle restitution coefficient
E	constant in wall function formulation
e_w	particle-wall restitution coefficient
\underline{F}_D	interphase drag force per unit volume [$\text{kgm}^{-2}\text{s}^{-2}$]
Fr	constant in frictional pressure expression [$\text{kgm}^{-1}\text{s}^{-2}$]
\underline{g}	acceleration due to gravity [ms^{-2}]
g_0	radial distribution function at contact
h	jet height [m]
H_i	initial height of the bed [m]
H_j	inlet jet height from the bottom [m]
I	intensity [V]
\underline{I}	identity tensor
J_s	granular energy dissipation due to inelastic collisions [m^2s^{-3}]
k	gas-phase turbulent kinetic energy [m^2s^{-2}]
k_{sg}	cross-correlation [m^2s^{-2}]

L, H, W	column width, height and thickness [m]
L_p	inlet pipe length [m]
m_s	solids downward extraction rate [kg s^{-1}]
MW	molecular weight of gas [g/mol]
N	number of ice crystal or bed particle bursts
P	pressure [$\text{kg m}^{-1} \text{s}^{-2}$]
P_k	turbulent kinetic energy production [$\text{m}^2 \text{s}^{-3}$]
P_o	outlet pressure [$\text{kg m}^{-1} \text{s}^{-2}$]
r	constant in frictional pressure expression
Re	Reynolds number
Re_p	particle Reynolds number, $Re_p = (v_g - v_p)d_p/v_g$
s	constant in frictional pressure expression
\underline{S}_s	solid rate of strain tensor [s^{-1}]
St	Stokes number
t_r	response time [s]
t	time [s]
T	temperature of gas [K]
\bar{U}	mean velocity [m s^{-1}]
u	fluctuating velocity when used in Chapter 3 [m s^{-1}]
\underline{u}	velocity [m s^{-1}]
U, V, W	streamwise, transverse and spanwise components of mean velocity when used in Chapter 3 [m s^{-1}]
\underline{u}'	fluctuating velocity (turbulent contribution) when used in Chapter 4 [m s^{-1}]

U_j	inlet horizontal jet velocity [ms^{-1}]
v	vertical component of mean velocity [ms^{-1}]
v'	fluctuating axial velocity when used in Chapter 2 [ms^{-1}]
v'	vertical component of fluctuating velocity (turbulent contribution) when used in Chapter 4 [ms^{-1}]
v'_{mean}	vertical component of fluctuating velocity (mean contribution) [ms^{-1}]
v'_{total}	vertical component of fluctuating velocity (mean + turbulent contributions) [ms^{-1}]
V_{fi}	uniform distributor gas velocity [ms^{-1}]
V_j	vertical inlet jet velocity [ms^{-1}]
V_{mf}	minimum fluidization velocity [ms^{-1}]
w	spanwise width [m]
x, y, z	coordinate distances [m]
$x_{1/2}$	jet plume half-width defined as the radial distance at which $v=0.5v_m$ [m]
$y_{1/2}$	jet half-width defined as $U(y_{1/2})=0.5U_c$ [m]

Greek Symbols

Δx	width of computational cell next to wall [m]
α	angle of jet with the horizontal [deg]
$\acute{\alpha}$	constant in granular theory
β	gas-solids drag force coefficient [$\text{kgm}^{-3}\text{s}^{-1}$]
$\underline{\underline{\delta}}$	identity tensor when used in Chapter 3
δ	angle of internal friction [deg]
$\Delta P/\Delta H$	pressure drop per unit height [$\text{kgm}^{-2}\text{s}^{-2}$]

δ_w	angle of wall friction [deg]
ε	gas turbulent energy dissipation [m^2s^{-3}]
ε_i	initial gas volume fraction
ε_m	volume fraction of phase m
η	constant depending on particle restitution coefficient
θ	granular temperature [m^2s^{-2}]
K_s	solids granular conductivity [$\text{kgm}^{-1}\text{s}^{-1}$]
K_v	von Karmen constant
μ	viscosity [$\text{kgm}^{-1}\text{s}^{-1}$]
ν	laminar kinematic viscosity [m^2s^{-1}]
ν_T	turbulent kinematic viscosity [m^2s^{-1}]
π_k	turbulence enhancement due to granular energy exchange [$\text{kgm}^{-1}\text{s}^{-3}$]
π_k^{drag}	drag contribution to gas turbulence enhancement [$\text{kgm}^{-1}\text{s}^{-3}$]
π_k^{wake}	wake contribution to gas turbulence enhancement [$\text{kgm}^{-1}\text{s}^{-3}$]
π_θ	granular energy enhancement due to turbulence exchange [$\text{kgm}^{-1}\text{s}^{-3}$]
ρ	density [kgm^{-3}]
$\underline{\underline{\sigma}}$	stress tensor [$\text{kgm}^{-1}\text{s}^{-2}$]
$\underline{\underline{\tau}}$	shear stress tensor [$\text{kgm}^{-1}\text{s}^{-2}$]
φ	specularity coefficient

Subscripts

c	centerline, defined as $y = 0$ and $z = w/2$
$c/$	value at the jet axis or centerline, at a given axial distance

<i>g</i>	gas phase
<i>i, k</i>	vector component
<i>j</i>	inlet jet conditions

Superscripts

<i>kc</i>	kinetic and collisional
<i>f</i>	frictional
<i>max</i>	maximum packing
<i>min</i>	intermediate packing

Abstract of Dissertation Presented to the Graduate School
of the University of Florida in Partial Fulfillment of the
Requirements for the Degree of Doctor of Philosophy

PREDICTING GAS-SOLID BUBBLING BED FLOWS USING CONTINUUM MODELING

By

Deepak Rangarajan

August 2012

Chair: Jennifer S. Curtis
Major: Chemical Engineering

The continuum approach, which treats particles as a continuous fluid-like phase, is a versatile and computationally feasible tool to model industrial-scale flows of jet injection into fluidized beds. In order to appropriately describe the closure relations and to test the validity of model predictions, however, comprehensive experimental measurements are needed at the macroscopic and microscopic scales.

Experimental studies concerning jet injection into fluidized beds have been limited to the measurement and analysis of mean velocity profiles. Here, laser Doppler measurements of fluctuating intensities of both gas and particle velocities inside the jet plume are presented as a function of the emulsion fluidized state. A qualitative analysis based on the coupling that occurs between the two phases is proposed to explain the observations.

Jet injection experiments are often conducted in pseudo-2D geometry and this requires that the role played by bounding walls be quantified. As a first step, a single-phase study on the effect of spanwise width on a rectangular jet with sidewalls is conducted using a standard k-epsilon model with wall functions. An order of magnitude

analysis reveals the role played by spanwise turbulent shear terms, as the aspect ratio is decreased at high streamwise distances.

Next, a continuum model that includes description for solid frictional stress and a turbulent gas phase is evaluated against experimental measurements of mean and fluctuating velocities inside the jet plume of a bubbling fluidized bed with vertical jet injection. The main uncertainties in closure relations are systematically determined using appropriate experimental data. In general, the model shows good agreement with experimental results. Trends in the centerline mean and fluctuating velocities with change in the fluidized state are also captured favorably. Main deviations between the model and experiment are noted and possible reasons for the mismatch discussed.

Finally, the continuum model is applied to study the influence of various operating parameters on the size and shape of the raceway (void zone) formed in an industrial-scale blast furnace operation. The results show how the raceway is affected by jet velocity, outlet pressure, particle size, bed height, inlet height, downward extraction, injection angle, and domain geometry.

CHAPTER 1 INTRODUCTION

Bubbling Fluidized Beds

When gas is introduced upwards through a bed of particles and the velocity of the gas is increased, a point is reached when the upward drag force exerted by the gas on the particles is equal to the apparent weight of the particles in the bed. The bed is then said to be fluidized and the gas velocity is called minimum fluidization velocity [1].

Beyond minimum fluidization velocity, particle-free voids or bubbles often start appearing in the fluidized bed. The bubbling behavior depends on both gas and particle properties. Geldart [2] classification of powders can be used to qualitatively estimate the bubbling behavior of particles at ambient conditions. Due to the favorable mixing capability of bubbling fluidized beds, they are commonly encountered in several physical processes such as drying, granulation, coating, heating and cooling, and over a wide range of industries such as food, agriculture, pharmaceutical, energy and mining.

Jet Injection into a Bubbling Fluidized Bed

Gas jets are frequently injected into bubbling fluidized beds for feeding reactants, enhancing mixing and stimulating solids flow [3]. For example, jets of steam and air are injected into a bubbling fluidized bed of coal or biomass during the gasification process. Typically, when a jet is introduced at high speeds, it results in the formation of a void region referred to as a jet plume. The jet plume is a region of vigorous mass, momentum and energy transfer and interacts with the bubbling emulsion region. Modeling jet injection into a fluidized bed of particles is important for better design and optimization of a variety of industrial reactors.

Prior Work and Motivation

Modeling

Describing jet injection into bubbling fluidized beds initially involved deriving empirical correlations for macroscopic quantities such as jet penetration length and jet expansion angle as a function of physical properties and operating conditions [4-6]. While empirical correlations are useful rules of thumb, they make many assumptions and do not provide all the information necessary to understand the flow. Moreover, these correlations determine parameters based on laboratory-scale experiments which make the expressions susceptible to scale-up issues. In recent years, with the advancement in computational resources, computational modeling has been the norm. Computational models solve differential equations based on first principles and provide all meaningful information about the flow, including microscopic details. Computational models that are capable of describing the flow behavior of particulate systems can be roughly divided into two groups, Discrete Element Models (DEM) and continuum models [7].

DEM models calculate the path and motion of each individual particle based on Newton's laws. The DEM approach benefits by its ability to easily vary the physical properties associated with individual particles (e.g. size or density). Moreover, local physical phenomena related to the particle flow behavior can be easily probed. However, the DEM approach cannot be used given current computational power and memory when the particle number exceeds 10^5 - 10^6 [8]. Given that the number of particles required to track the behavior of industrial-scale bubbling beds exceeds that limitation in particle number by more than several orders of magnitude, DEM is not a feasible approach.

Continuum models assume that particles form a continuous fluid-like phase and volume averaged continuity and momentum equations are derived for the gas and solid phases. This drastically reduces the number of differential equations required to be solved, but as a result of the averaging process, constitutive relations need to be developed to close the continuum equations. The development of these closure relations range from theoretical derivation to highly empirical correlations. Continuum modeling has been successfully applied in a wide range of particulate processes such as pneumatic conveying, fluidized beds, cyclones and hoppers [9-12]. It has been an economically beneficial tool for many industries [13]. However, a thorough understanding of continuum modeling, including the empiricism in its closure relations is necessary to ensure reliability and improvement of such models. This is generally achieved by conducting validation studies which compare model predictions against experimental data.

Validation studies that evaluate the performance of continuum models in predicting bubbling bed flows are plenty in literature [3, 14-21]. While a few of these studies compare detailed particle velocity profiles against experiments [17, 19, 21], a majority of them validate macroscopic quantities such as bubble size, bubble shape, bubble rise velocity, bed expansion, spout height, jet penetration length, jet expansion angle and holistic particle movement. While evaluations of macroscopic engineering properties are very important, they are not sufficient to ensure the fundamental accuracy of continuum models. In fact, the advantage of using continuum models over empirical correlations is that they are more fundamentally based, and this claim requires testing against detailed differential scale measurements. Moreover, most continuum validation studies analyze

the sensitivity of various closure relations on the overall model prediction. While such an approach gives useful insight on the physics of the specific flow being investigated, it is not very helpful towards developing a generally applicable continuum model, since the closure relations tend to be coupled. Instead, a systematic approach of first identifying where the main uncertainties and empiricism lie, and then developing a method to determine the unknown terms independently, will be more helpful in applying continuum modeling in a generalized framework.

Experiment

As mentioned earlier, modeling approaches are not without their shortcomings and cannot be used in the absence of careful experimental validation. Experimental work regarding jet injection into bubbling fluidized beds initially measured macroscopic properties of jet penetration length and shape [22], but have recently moved towards microscopic velocity measurements to complement more fundamental modeling approaches. Detailed experimental measurements are not only useful for validating computational models but also provide physical insight on the two-phase transport that occurs inside the jet plume region. Differential scale profiles of gas velocity, particle velocity and solids concentration have been reported inside the jet plume [23-27]. Typically, velocities have been measured using Pitot tube and high-speed camera until the recent work of Mychkovsky and Ceccio [27] who employed the technique of Laser Doppler Velocimetry (LDV) to measure the velocities of gas and particles simultaneously. Though the jet plume is a region of turbulent mixing, measurements of the fluctuations in gas or particle velocities haven't been reported in literature so far.

Quantifying Pseudo-2D Experimental Arrangement

Experiments of jet injection into fluidized beds are typically conducted in ‘two-dimensional’ transparent columns [26, 27]. These columns have a rectangular cross-section with a very small spanwise dimension that enables optical access to the plume region. Although experiments claim to be 2D, the role played by the walls needs to be quantified. This will help in deciding if two-dimensional simulations are sufficient or the more computationally expensive three-dimensional simulations are required for validation studies. As a first step towards tackling this two-phase problem, the role of spanwise width on single-phase jets in an empty column, needs to be studied. Though Computational Fluid Dynamics (CFD) provides a convenient way to quantify bounding wall influence, a systematic CFD study that investigates the effect of spanwise width on single-phase planar jets has not been reported in literature so far.

Industrial Application

An important application of jet injection into a bed of particles is in the ironmaking blast furnace operation. A blast furnace is a huge furnace in which iron ore and coke are dumped from the top and preheated air is blown at a high velocity sideways from the bottom through tubes called tuyeres. The resulting void region formed is referred to as a raceway. The purpose of the blast furnace operation is to chemically reduce iron ore into liquid iron and the temperatures of the blast air can be as high as 1300 °C. The extent of various smelting and reduction reactions that follow is determined by the mixing between the coke particles and the injected air, which in turn is related to the size and shape of the raceway formed [28, 29]. In-situ experimental investigation is difficult because of high temperature and harsh nature of flow which is why physical modeling is necessary [30]. As seen earlier, continuum modeling provides a versatile

and economically feasible tool to model such industrial-scale flows. Unfortunately, continuum studies of raceway properties which employ proper closure relations are lacking in literature.

Thesis Objectives and Outline

The objective of this thesis is to address the following four areas of research that would contribute to the modeling and industrial application of bubbling particulate flows.

1. Two-phase fluctuating velocity profile measurements inside the jet plume region of a bubbling fluidized bed with jet injection.
2. Single-phase CFD study that quantifies the role of sidewalls in wall-bounded jet flows.
3. Systematic continuum model validation of bubbling beds which evaluate model predictions against detailed experimental data.
4. Continuum model application in raceway formation inside a blast furnace.

This thesis is divided into 5 more chapters. Chapter 2 extends the recent work of Mychkovsky and Ceccio [27] which employed LDV to measure radial profiles of gas and particle mean velocities at various streamwise locations inside the jet plume of a bubbling fluidized bed. In Chapter 2, the measurement and analysis of the corresponding fluctuating intensities are presented as a function of the fluidized state of the emulsion. The effect of spanwise width in single-phase wall bounded jet flows is studied with the help of CFD in Chapter 3. In Chapter 4, appropriate closure relations that are necessary in a gas-solid continuum framework to describe bubbling bed flows are determined from currently available expressions in literature. The final model is then validated with the help of experimental measurements made in Chapter 2. Chapter 5 applies a state-of-the-art continuum model with appropriate closure relations to explore the influence of operating parameters on the raceway size and shape in the lower part

of a blast furnace operation. Finally, the conclusions and recommendations for future work are presented in Chapter 6.

CHAPTER 2 EXPERIMENTAL MEASUREMENTS

Background

Detailed and non-intrusive experimental measurements concerning jet injection into bubbling beds has been found lacking due to the harsh and semi-opaque nature of flow. An overview of the experimental work done to describe the penetration of gas jets in fluidized beds can be found in Filla *et al.* [31]. Some of the earlier works concentrated on obtaining integral or large scale properties which are observable at the macroscopic level, such as the plume size and shape, using photographic studies [22]. However, due to the chaotic nature of the flow, difficulties have been encountered in determining these properties accurately.

On the other hand, more recent experimental work focusing on the measurement of axial and radial profiles of flow variables within the jet plume region has proved to be more consistent and useful. Some of the profiles obtained so far include gas and solids velocities and solids concentration [23-27]. Typically, gas velocity has been obtained using Pitot tube, particle velocity using high-speed camera and solids concentration using direct, indirect and mixed methods. Mychkovsky and Ceccio [27] found self-similar Gaussian shaped curves for gas and particle mean velocities and Donodano *et al.* [23] concluded that voidage can be approximated by a two-level radial profile.

Though the jet plume is a region of turbulent mixing between the emulsion and the jet, there are no published experimental measurements of fluctuation in the velocities of either phase inside the region. Fluctuation measurements would help in the development of fundamentally rigorous models which include descriptions of turbulent flow that contribute to explaining the momentum transport. For example, experimental

data can be used to develop improved closure relations for fluctuating velocity interactions between the two phases in the gas-solid turbulence equations. The reason for the lack of these data can be attributed to the limitations of the experimental techniques used to date- namely, Pitot tubes and high-speed cameras, in measuring fluctuating velocities.

This study addresses the above issue by extending the recent work of Mychkovsky and Ceccio [27] which employed LDV to measure radial profiles of gas and particle mean velocities at various axial locations inside the plume as a function of the fluidization rate. In this work, the measurement and analysis of the corresponding fluctuating intensities are presented. The results show how the axial fluctuating intensities of gas and solid phase velocities inside the plume vary with change in the fluidized state of the emulsion.

Experimental Setup

Figure 2-1 presents a photograph and description of the experimental apparatus. A thin, two-dimensional, rectangular column enables optical access to the region within the jet plume. The column measured 457 mm in width, 1 m in height and 12.7 mm in thickness. The walls were made of transparent acrylic. The system dimension and chosen coordinate system are shown in Figure 2-2. A vertical jet inlet flush with the distributor surface and having a diameter, $D_j = 9.2$ mm, was placed at the origin. A quartz viewing window measuring 102 mm by 153 mm was inserted at a height $y = 50$ mm, for the velocity measurements. The gas was atmospheric air which was cooled to a temperature $T_j = -5^\circ\text{C}$ to produce ice crystals which enabled optical tracing of the gas. The ice crystals were formed by freezing water vapor naturally existing in air. The bed particles were high density polyethylene spheres with a Sauter mean diameter, d_p , of

838 μm and density, ρ_p , of 900 kg/m^3 . These particles fall into the Geldart B classification of powders, which bubble immediately upon reaching minimum fluidization. The minimum fluidization velocity, V_{mf} , of the emulsion was experimentally found to be 29 cm/s . Since the aim of the present study is to investigate the influence of the emulsion fluidization state, the distributor velocity V_{fl} was varied as $V_{fl}/V_{mf} = 0, 0.7, 1.0, 1.15, 1.3$ and 1.5 as separate cases (Table 2-1), while keeping other parameters, such as the inlet jet velocity (V_j) and the initial bed height (H_i), a constant at 92 m/s and 38 cm respectively. The fluidization air was first turned on, followed by the jet air. All measurements were made once a visually stable plume was formed, which took less than a second after turning on the jet inlet.

Particle and gas axial velocity measurements were obtained via a two-component LDV system comprising a 5W argon-ion laser and a TSI signal analyzer. The axial measurements were recorded through Channel 1 which used the green beam. Channel 2, employing the blue beam, was oriented along the transverse (radial) direction and used so that coincident Doppler bursts could be obtained. The details of the LDV configuration are summarized in Table 2-2. As mentioned earlier, extremely small ice crystals formed by the rapid cooling of the jet inlet air were used as seeding in order to enable gas velocity measurements. The Doppler bursts produced from the light reflected by both tracer ice crystals and bed particles were separated primarily based on the intensity of light emitted (I) as follows.

- Bed particles: $I > 500 \text{ mV}$, $10 \mu\text{s}$ coincidence
- Gas tracer ice crystals: $I < 200 \text{ mV}$, $0 \mu\text{s}$ coincidence

Further detail regarding the measurement technique can be found in Mychkovsky *et al.* [32]. Once two minutes worth of Doppler bursts (N) corresponding to either bed particles

or tracer ice crystals were obtained, the velocity statistics were calculated by standard correlations given below.

$$\bar{v} = \frac{\sum v}{N} \quad (2-1)$$

$$\bar{v}' = \sqrt{\frac{\sum (v - \bar{v})^2}{N}} \quad (2-2)$$

In the above equations, v is the instantaneous axial velocity obtained from each burst, \bar{v} , the mean and \bar{v}' , the standard deviation. Henceforth \bar{v} and \bar{v}' will be denoted simply as v and v' respectively. For each experiment, axial velocity profile measurements were made at locations of $y = 60, 70, 100$ and 130 mm. For each axial location, measurements were made every 1-2 mm in the transverse (radial) direction on either side of the jet axis until the dense nature of the plume-emulsion boundary prevented further optical access.

In order to obtain the fluctuating components of velocity, a good representation of the instantaneous velocities provided by the Doppler bursts must be available. The evolution of tracer and particle velocity statistics were checked for the 2 minutes of recorded bursts. A steady value for the gas and particle fluctuating velocity is reached after about 500 bursts. Hence to be conservative, only fluctuation measurements with counts greater than 1000 were considered. While measurements made at most locations had counts of more than a 1000, a few locations had insufficient number of bursts due to either poor seeding of tracer ice crystals (at higher axial locations and fluidization rates) or low particle concentrations (towards the boundary of the jet plume). These data points were eliminated. This is the reason why no results are presented for $V_{fl}/V_{mf} = 1.5$ (case 7) at $y/D_j = 14.13$.

To check the reproducibility of the fluctuating velocities, the case with a distributor velocity of $V_{fl}/V_{mf} = 1.15$ (Case 5) was conducted three times. It was found that the variation in the fluctuating intensity was between 5 to 15% for both gas and particle phase velocities. The major source of these random errors is estimated to be from the chaotic nature of plume boundary swaying. Other sources of error include precision of the LDV measurement technique and the flow meters, varying static effects of the bounding walls, and a small amount of particle attrition arising from the harsh nature of the flow.

Results and Discussion

Profiles of Mean Velocity

The mean velocity profiles are found to be axially self-similar and Gaussian shaped, which is consistent with literature [31]. The transverse (radial) profiles obtained at $y/D_j = 10.87$ are shown in Figure 2-3 for different experimental cases. Analysis of the effect of fluidization on the mean axial velocity inside the jet plume of a bubbling bed can be found in Mychkovsky and Ceccio [27].

Single-Phase Fluctuating Velocity Validation

The fluctuating intensity in the velocity of a gas jet through the empty column also referred to as the “Empty Bed” (Case 1) is compared to other planar jet experimental data in Figure 2-4. It must be noted that the data previously reported in literature has been restricted to one half of the domain, namely $x/x_{1/2} \geq 0$ and has been reflected along the centerline. Figure 2-4 shows good agreement with Miller and Comings [33] but poor agreement with Gutmark and Wygnanski [34]. This is because the axial locations of the measurements made by Miller and Comings [33] and in the present study both happen to lie within the potential core or non self-similar region of turbulence. On the other

hand, measurements of Gutmark and Wygnanski [34] were made at axial locations beyond $y/D_j = 95$ which is in the self-similar region. No significant effect of the bounding walls in the present work is observable.

Profiles of Fluctuating Velocity

The transverse (radial) profiles of the intensity of fluctuations in the axial velocity for different experimental cases for both gas and particle phases are shown at four axial distances of $y/D_j = 6.52, 7.61, 10.87$ and 14.13 respectively, in Figures 2-5 and 2-6. To provide a reference state for comparison between the fluctuations in the two phases, Empty Bed (Case 1) gas fluctuating intensities are added along with the particle phase profiles. It can be seen that the particle fluctuating intensities are approximately 50% greater than the gas fluctuating intensity. In general, the shapes of the profiles of both the phases are similar to the Empty Bed (Case 1) profile. However, more deviation in the shape can be observed at larger fluidizing rates for the particle phase. This is probably due to the macroscopic or integral phenomenon of “fluttering”, which is the fluctuating motion of the plume boundary demarcating the emulsion and the jet plume regions, that occurs in the flow. This fluttering was visually observed to be more prominent when the emulsion was at a higher fluidized state, causing deviation in fluctuating velocity profile shape from the Empty Bed. Its influence was observed in both the mean and fluctuating velocities of the particle phase. The next section provides a more detailed analysis of the effect of fluidization on the fluctuating velocities by looking along the centerline of the jet.

Discussion of Variation in Centerline Fluctuating Velocity

Figure 2-7 and Figure 2-8 show the fluctuating intensity in the axial velocity of the two phases along the centerline of the jet for different experimental cases at four axial

distances of $y/D_j = 6.52, 7.61, 10.87$ and 14.13 . Some significant trends can be observed from these figures. Firstly, the fluctuating intensities tend to increase in the axial direction for the same experimental case. Secondly, there is an increase in gas turbulence in the Spouted Bed (Case 2) as compared to the Empty Bed (Case 1). Thirdly, increasing the distributor gas velocity tends to initially decrease and then increase the fluctuations in both phases. Further, the fact that the particle and the gas velocity fluctuations complement each other is illustrated.

In order to explain the above observed behavior, it is important to identify the multiphase turbulence interaction that is taking place between the two phases. The turbulence coupling that happens between the gas and solid phases can be divided into two contributions. One is the indirect contribution that occurs through mean flow variables while the other is the direct contribution that occurs via fluctuating components.

Coupling through mean flow variables

It can be postulated that the effect of particle phase on the fluctuating behavior of gas phase and vice versa occurs through the mean flow variables, namely, gas phase plume half-width, void fraction and maximum axial velocity, for a given axial location within the jet plume. It can be assumed that the relationship of gas turbulence intensity is direct with respect to the plume half-width, which is an indicator of the eddy length scale, and inverse with respect to the maximum axial velocity, which is an indicator of the mean velocity. On the other hand, the relationship of particle fluctuating intensity is direct with respect to the void fraction, which is an indicator of the mean free path, and inverse with respect to the maximum particle axial velocity.

Figure 2-9 and 2-10 show how the mean flow variables change with level of bed fluidization [27]. When moving from the Empty bed to the Spouted bed case, the gas flow rate inside the jet plume decreases due to the lack of gas entrainment from the surrounding packed bed and the jet spreading width also decreases due to the bed particles constricting the flow. However, the decrease in the maximum mean velocity caused by the lack of entrainment is much more significant than the reduction in the plume width. This decrease in mean velocity results in an increase in gas turbulence intensity. Starting with Case 4, which is the minimum fluidization case, increasing fluidizing air rate widens the jet spreading and increases void fraction as gas and particles from the emulsion phase and the jet plume, interact more freely. Thus, the increase in fluctuating intensity with fluidizing rate beyond minimum fluidization can be attributed to the increasing plume half-width for gas and void fraction for particles. It is also expected that the large scale unsteadiness in the flow caused by the bubbling emulsion action enhances fluctuations at high fluidization rates.

However, before reaching minimum fluidization it is seen that increasing fluidizing air rate decreases the fluctuating intensities. The additional gas flow within the voids of a packed bed facilitates a higher rate of gas and particles to be entrained into the jet from the emulsion. Hence, while the system cannot deform easily and there is negligible influence of the change in plume half-width and void fraction, the small increase in the gas and particle velocities within the plume causes the turbulence intensity to decrease in both phases (Case 3).

Coupling through fluctuating velocities

Although the variation in the fluctuating intensity with fluidization level for both phases can be explained based on a mean flow analysis, it is unclear how the two-

phase coupling at the fluctuating velocity level affects the magnitude of the fluctuations in each phase. Particle velocity fluctuating intensities (which are Eulerian values measured using LDV as opposed to Lagrangian) everywhere exceed gas fluctuating intensities in the jet plume. This is because the 838 micron polyethylene spheres possess high inertia, and, hence, the details of the particle motion are governed by particle-particle interactions, not by gas-phase turbulence. The fact that particle motion is unlikely to be affected by gas-phase turbulence inside the plume can be noted from the high of Stokes Number (St), which is the ratio of particle response time to gas response time. Defining the particle response time and gas response time, respectively, as,

$$t_{r,p} = \frac{\rho_p d_p^2}{18\mu_f} \quad (2-3)$$

$$t_{r,g} = \frac{D_j}{V_j} \quad (2-4)$$

the Stokes number is on the order of $\sim 10^4$.

In addition, the particle Reynolds numbers (Re_p), calculated based on the mean velocity measurements, are in the range $\sim 1500-3000$ everywhere along the plume centerline. Such high particle Reynolds numbers should give rise to gas turbulence enhancement due to vortex shedding in the particle wake. Hestroni [35] proposed that this vortex shedding mechanism would be significant when $Re_p > 400$.

Summary

There exists a need to measure gas and particle phase velocity fluctuations inside the plume region of a jet injected into a fluidized bed, in order to better understand transport in bubbling beds and to build more fundamental and reliable two-phase turbulence models. This study addresses this need by reporting measured radial

profiles of axial velocity fluctuations for different fluidized states of the emulsion, using laser Doppler velocimetry. The corresponding analysis also provides qualitative insight on the role of emulsion fluidization in the turbulent flow through variations in fluctuating velocities along the jet axis with change in fluidization rate. It is estimated that the gas flow within a packed bed causes additional entrainment of gas and particles into the jet plume from the emulsion phase with negligible influence of changes in jet spreading width and void fraction. This results in a small decrease in the intensity of velocity fluctuations in both phases on increasing distributor gas rate when below minimum fluidization. On the other hand, free mixing between the emulsion and the jet is achieved once minimum fluidization is reached. This widens the jet spreading width and increases the void fraction, thereby increasing fluctuating intensity with increase in distributor gas rate. It is expected that the particle phase enhances gas turbulence, though the relative importance of this mechanism compared to the coupling through mean flow variables is unclear.

In Chapter 2, the LDV technique of Mychkovsky *et al.* [32] has been successfully extended to extract profiles of velocity fluctuations of both phases. This data adds to the repository of experimental data collected which now includes the fluidization curve, bulk flow videos, mean and fluctuating velocity measurements [36, 37]. Before these comprehensive measurements can be used to validate computational models, the effect of the pseudo-2D geometry of the experimental setup employed has to be examined. With this issue as one of the motivations, a more general study on the effect of spanwise width on a rectangular turbulent jet with sidewalls is conducted in Chapter 3.

Table 2-1. Experimental cases considered.

Case	Description
1	No particles (Empty bed)
2	$V_{fl} = 0$ (Spouted bed)
3	$V_{fl} = 0.7 V_{mf}$
4	$V_{fl} = V_{mf}$
5	$V_{fl} = 1.15 V_{mf}$
6	$V_{fl} = 1.3 V_{mf}$
7	$V_{fl} = 1.5 V_{mf}$

Table 2-2. LDV parameters and settings.

	Ch 1	Ch 2
Laser Power per Beam (mW)	90	55
Beam Diameter (microns)	90	85
PMT Gain (mV)	450	450
Burst Threshold (mV)	250	150
Frequency Downmixing (MHz)	0	0
Band Pass Filter (MHz)	5-50	20-65
Bragg Shift Frequency (MHz)	40	40
Fringe Spacing (microns)	3.74	3.55
Velocity Range (m/s)	131 to -37	71 to -89
Coincidence Interval (μ s)	10	10

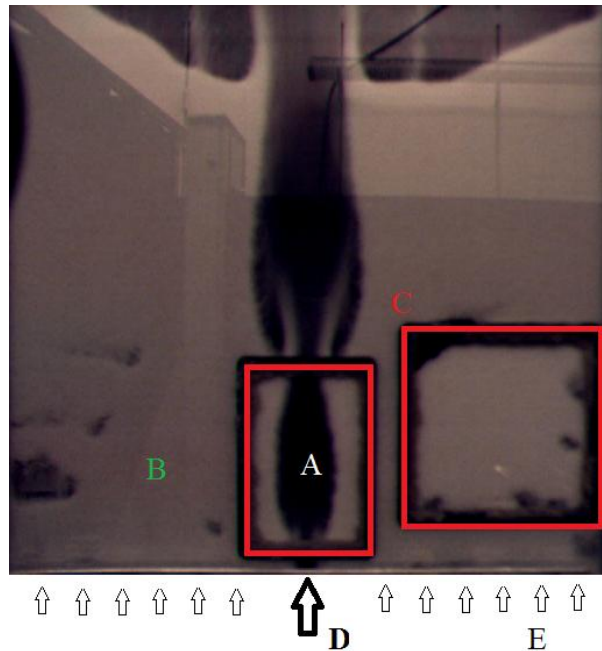


Figure 2-1. Photograph and description of experimental setup. A: Jet plume region; B: Emulsion region; C: Dark lines in the photograph caused by adhesive (not to be confused with voids in the flow); D: High velocity gas jet inlet; E: Distributor gas inlet to fluidize the bed particles.

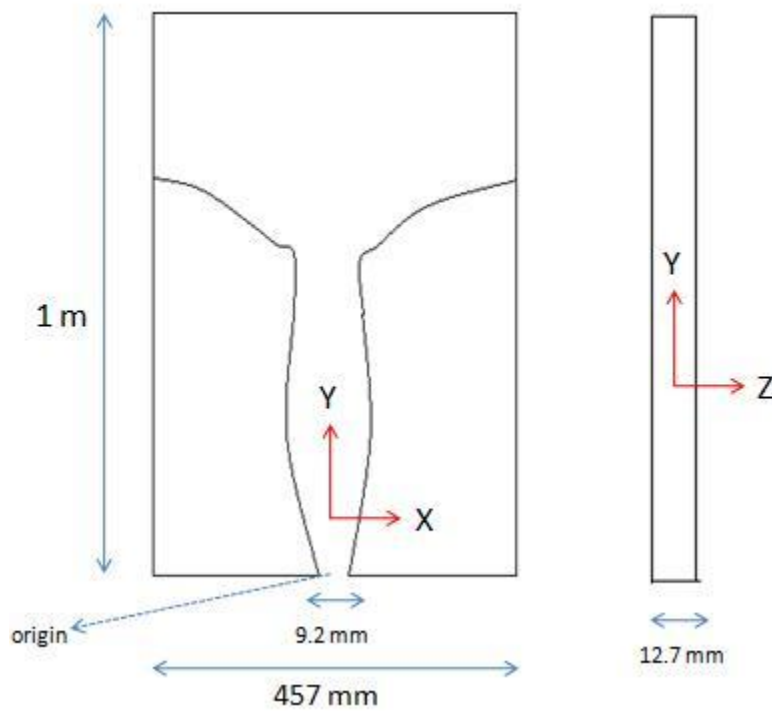


Figure 2-2. System dimensions.

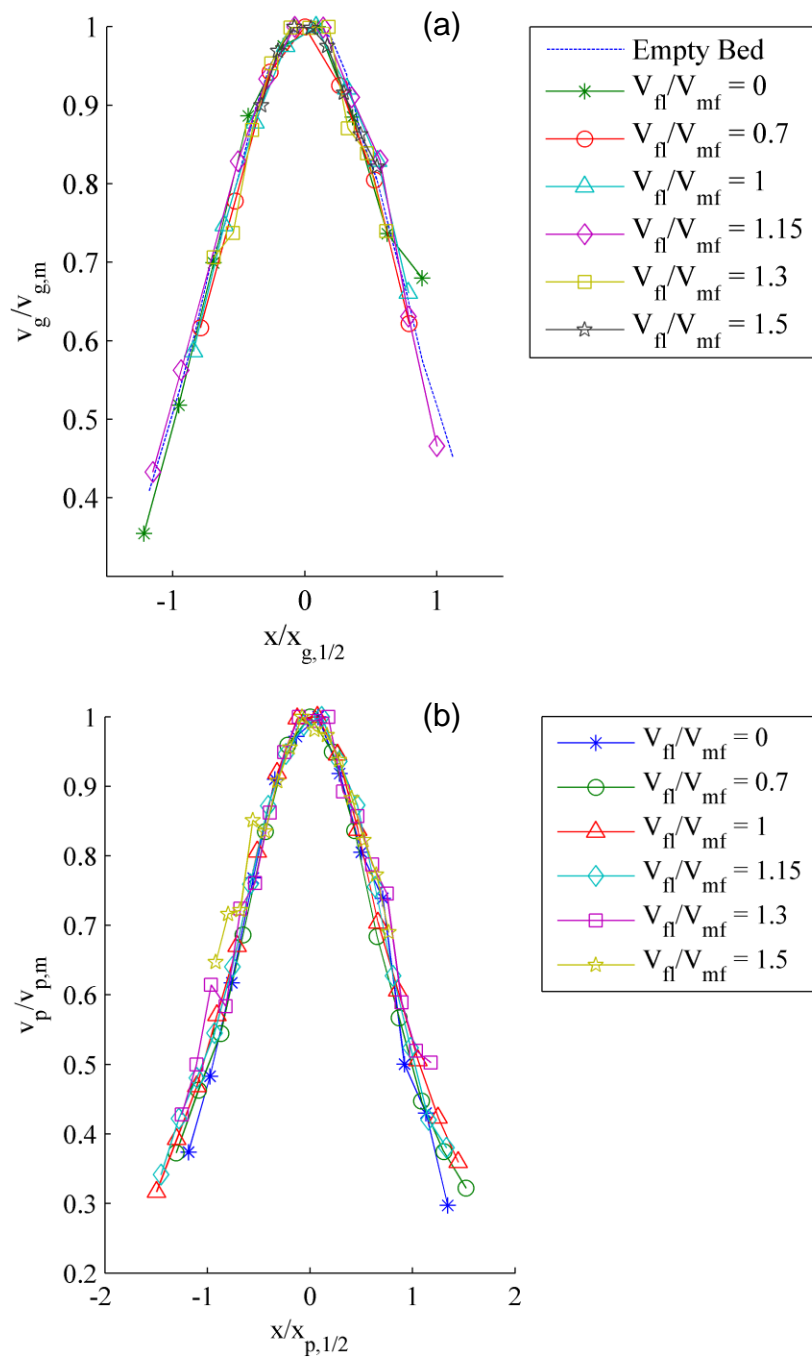


Figure 2-3. Mean axial velocity profiles at $y/D_j = 10.87$ for different experimental cases. (a) Gas, and (b) Particle.

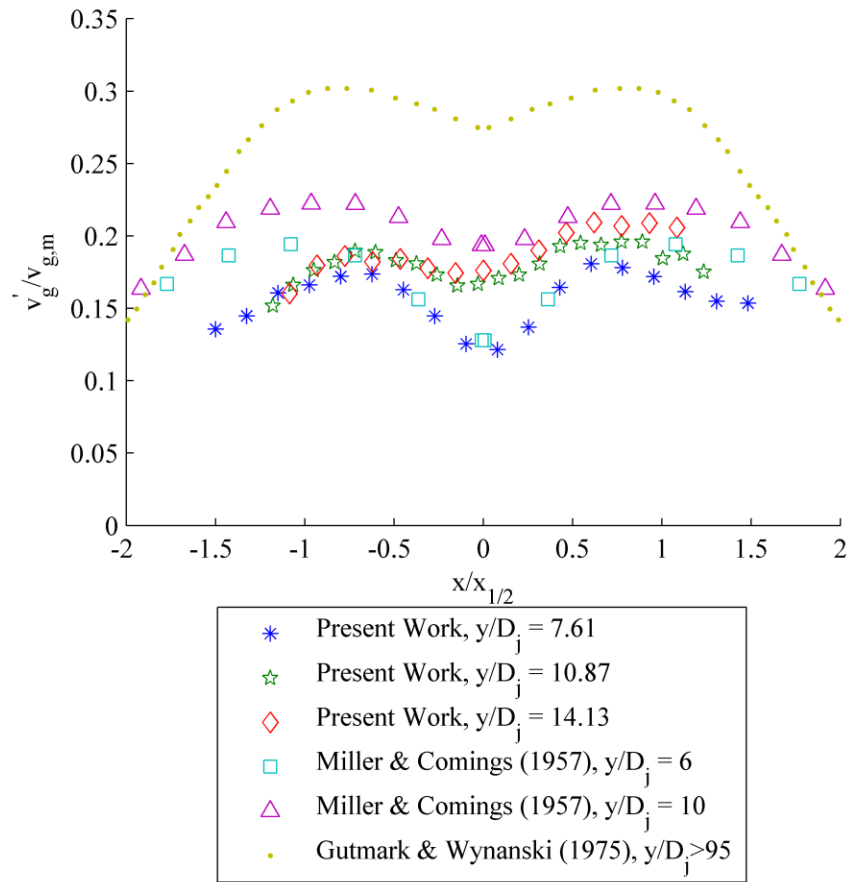


Figure 2-4. Comparison of fluctuating velocity in the Empty bed, case 1, with single-phase turbulent jet data from literature.

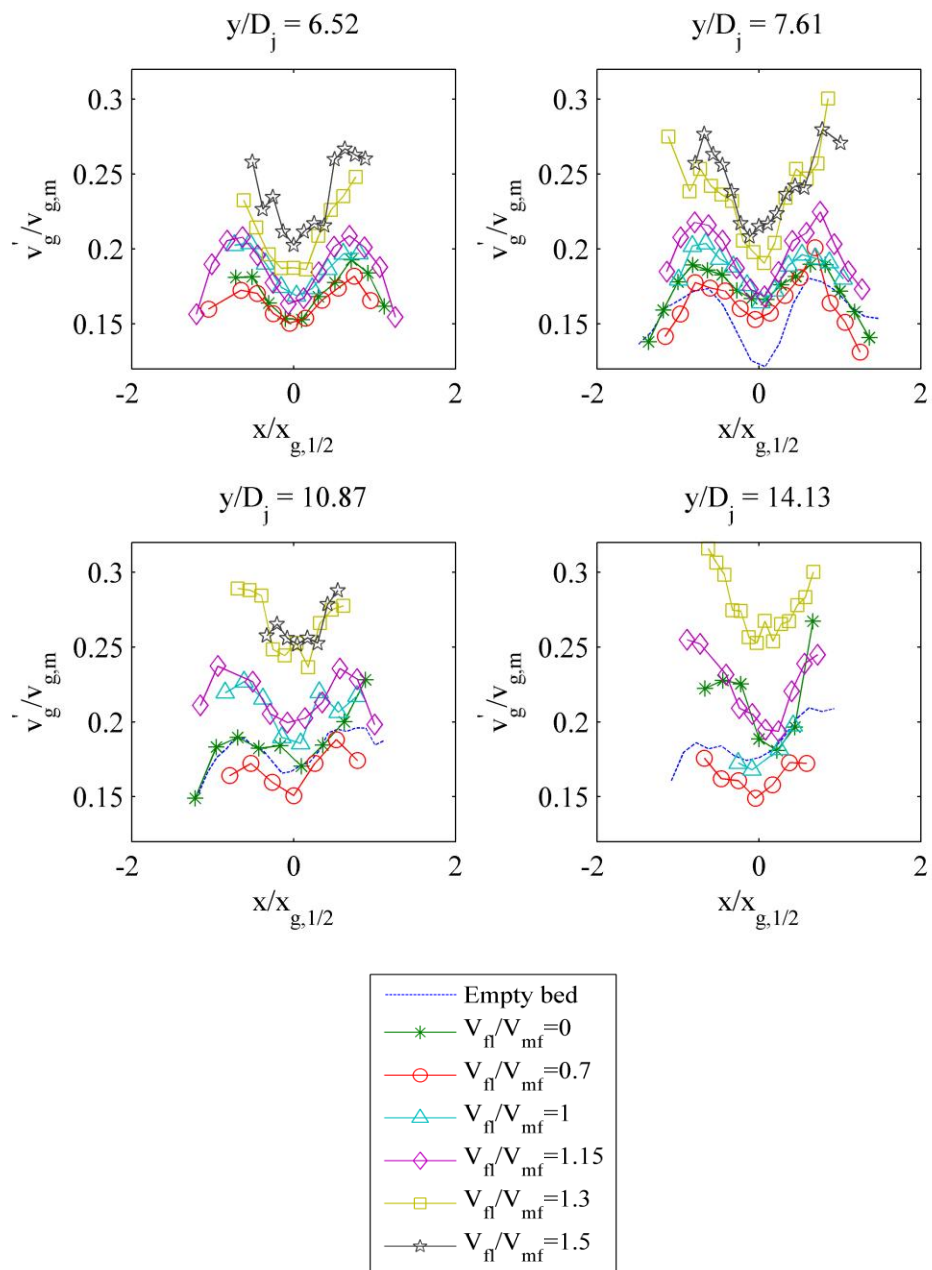


Figure 2-5. Radial profiles of gas axial fluctuating velocity for different fluidization ratios at different axial locations.

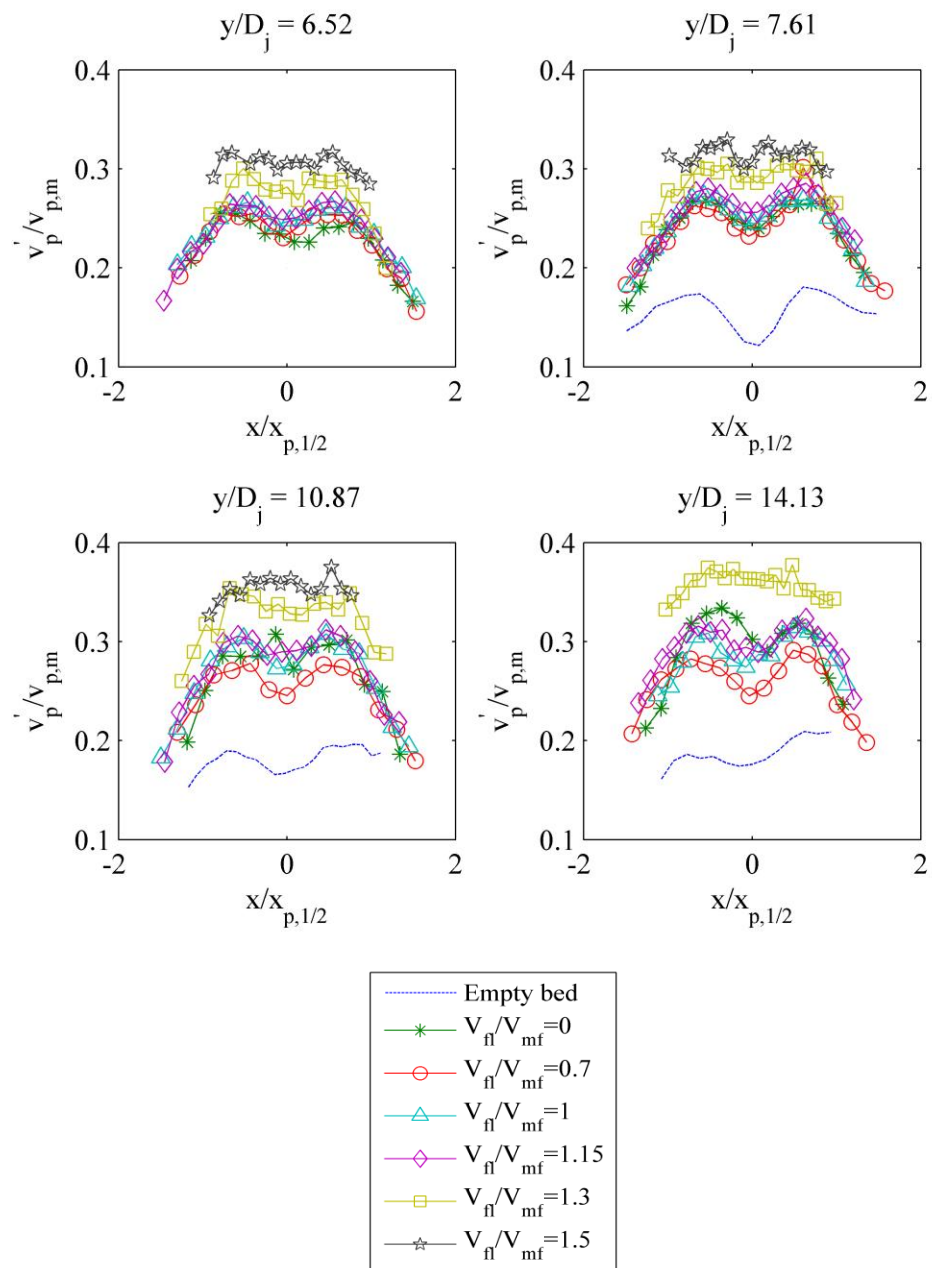


Figure 2-6. Radial profiles of particle axial fluctuating velocity for different fluidization ratios at different axial locations.

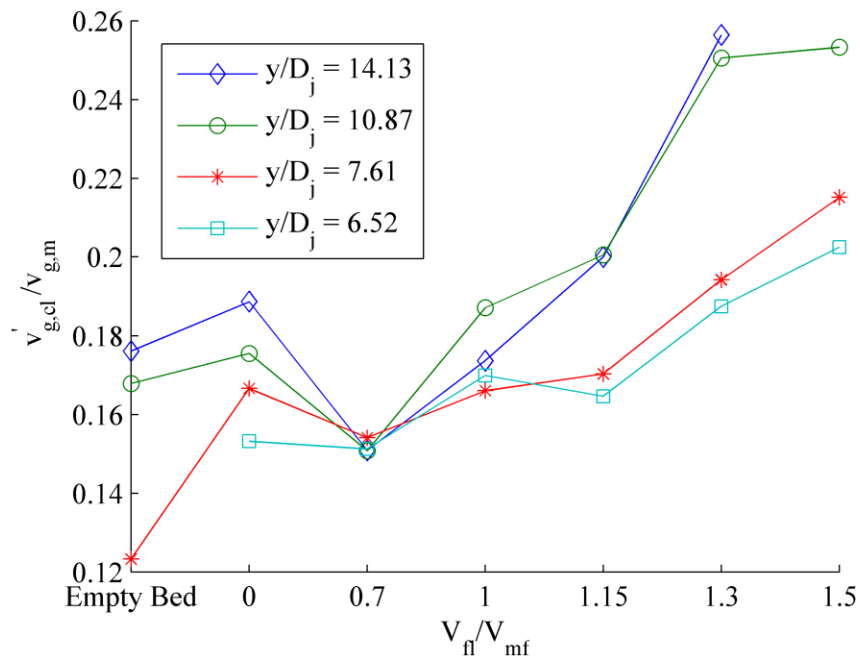


Figure 2-7. Axial gas fluctuating velocity along the centerline for different experimental cases.

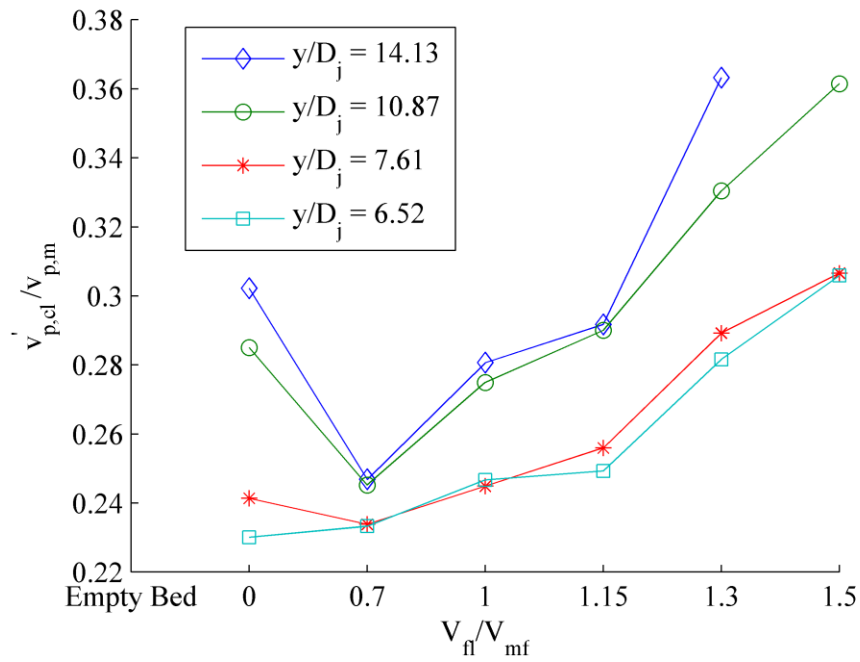


Figure 2-8. Axial particle fluctuating velocity along the centerline for different experimental cases.

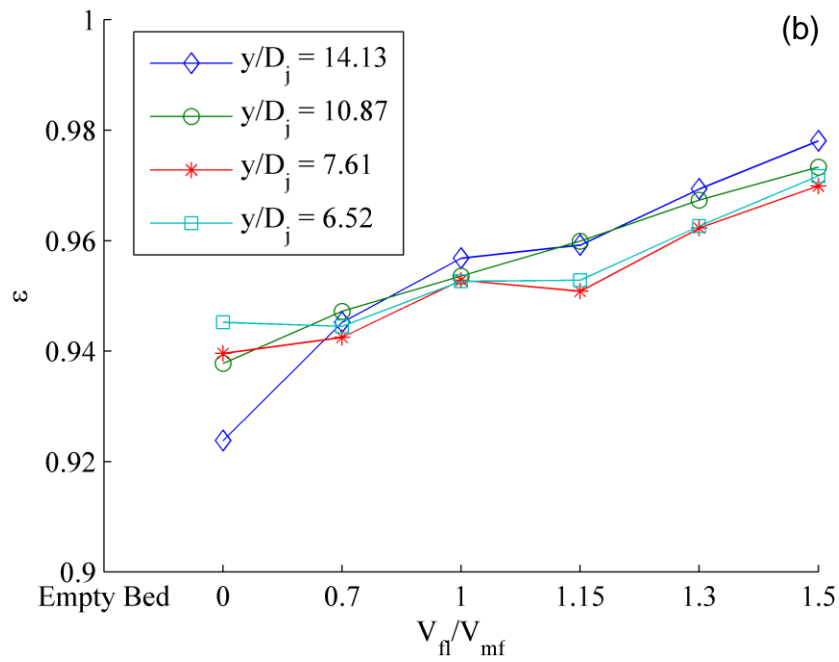
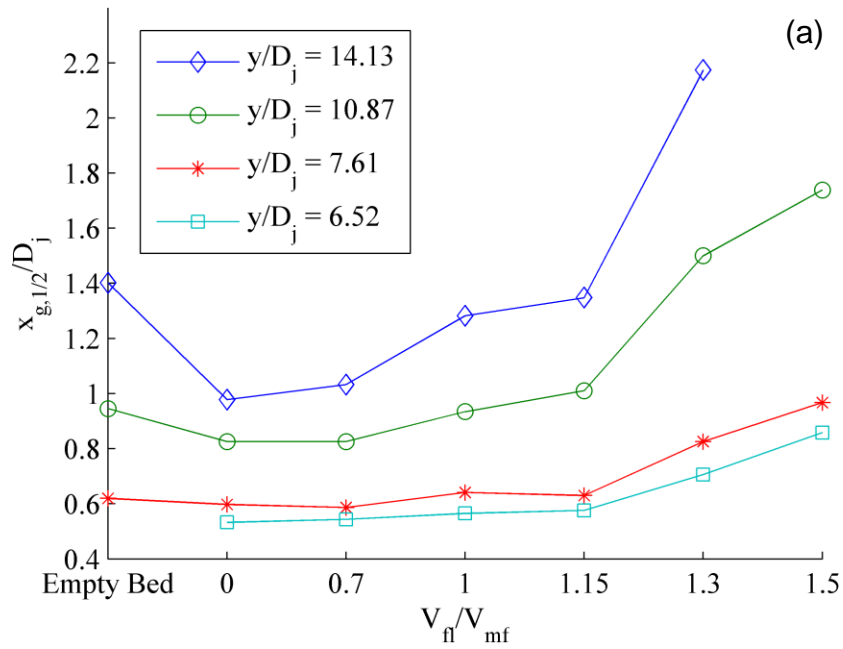


Figure 2-9. Variation with different experimental cases. (a) Gas plume half-width, and (b) Void fraction.

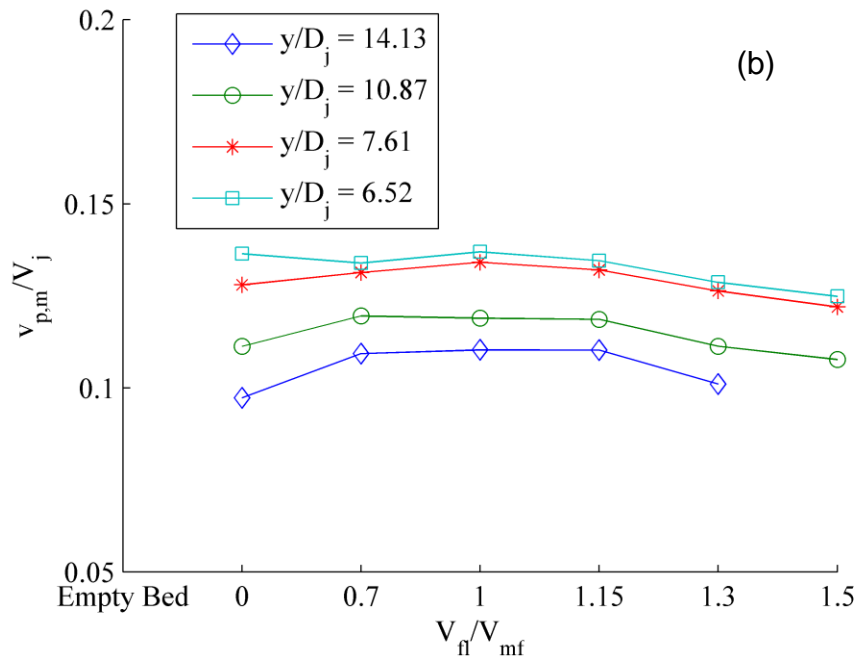
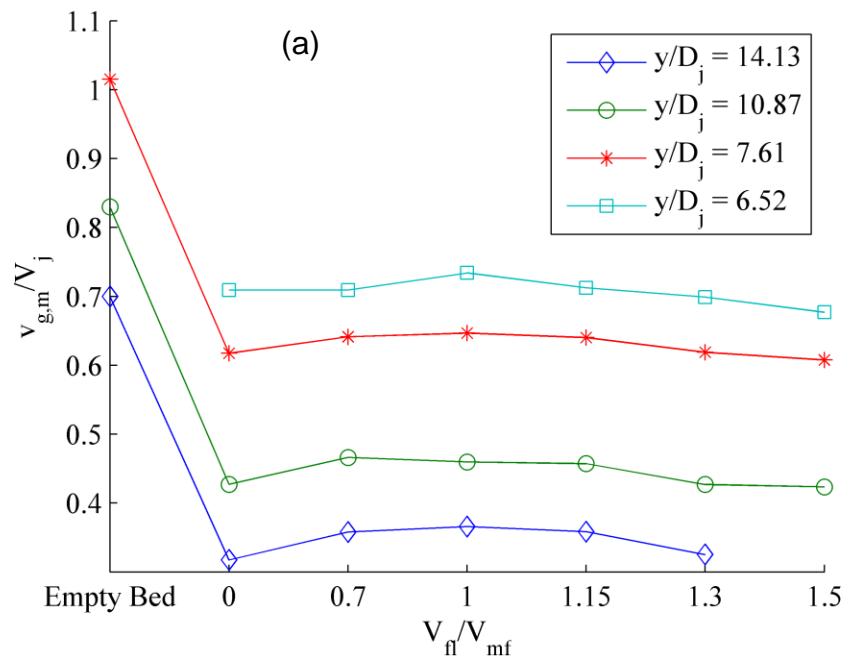


Figure 2-10. Variation in maximum axial velocity for different experimental cases. (a) Gas, and (b) Particles.

CHAPTER 3 SINGLE-PHASE NUMERICAL STUDY

Background

Various aspects of planar turbulent jets, due to their importance in understanding the fundamental nature of turbulence and their engineering applications, have been studied extensively for more than seven decades. Some of the most significant experimental works are those of Heskestad [38], who first measured the mean and fluctuating velocity profiles in the self-preserving region of a plane jet, Bradbury [39], who studied the flow behavior of a two-dimensional jet in the presence of co-flow, Gutmark and Wygnanski [34], who extended the measurements to include 3rd and 4th order moments, two-point correlations and intermittency factors at axial locations of up to 120 jet diameters, Everitt and Robins [40], who investigated the structure and development of turbulent jets in still air and in moving streams, and Browne *et al.* [41], who studied the turbulence behavior in the interaction region of a slightly heated planar jet and presented turbulence parameters such as Prandtl number, probability density function, skewness and flatness factors. For the sake of the present study, which is focused on the evolution of centerline mean velocity, centerline turbulence intensity and jet half-width as a function of downstream distance from the jet orifice, the major findings of these works can be summarized as follows.

Planar or 2D jet flow can be divided into two regions based on streamwise location – the potential core region and the self-similar region. The potential core region is characterized by a constant mean velocity and increasing turbulence intensity with increasing streamwise distance along the jet axis. The self-similar region is characterized by a mean velocity dependence of $x^{-1/2}$ and a constant turbulence

intensity along the jet axis, as well as a linear increase in jet half-width with increasing streamwise distance. While the physics of plane jets are now more or less well established, the exact influence of experimental conditions on the results is still under investigation.

The influence of experimental conditions on planar jet flows can be roughly divided into two categories. One category is the nature of the velocity profile at the exit of the jet nozzle, termed as initial conditions, which are determined by the flow feeding to the jet nozzle, and the other is the experimental geometry, termed as boundary conditions, which are determined by the physical domain into which the jet flow takes place. The influence of the velocity profile at the exit of the jet has been noted by numerous authors and studied extensively both experimentally and numerically [42-45]. Neglecting the difference in experimental geometry of Heskestad [38], Gutmark and Wygnakasi [34] and Browne *et al.* [41], which will be shown to be a good assumption later in this study, an example of the effect of the inlet velocity profile on planar jet flow is illustrated in Figure 3-1. While the velocity profile at the nozzle exit in the Gutmark and Wygnanski [34] case and in the case of Browne *et al.* [41] were predominantly top hat, that of Heskestad [1] was highly non-uniform resulting in deviation in the slope of the mean decay rate for Heskestad's case when compared to the other two (Figure 3-1a). On the other hand, as noted by Browne *et al.* [41], the fact that their exit profiles were laminar results in a different asymptotic turbulent kinetic energy value (Figure 3-1b) when compared to the turbulent exit profiles of the other two studies.

The present study falls into the second category, which involves the investigation of the influence of boundary conditions on planar jet flows. An ideal plane jet is the flow

that occurs when a fluid is issued through a rectangular nozzle which is infinitely long in the spanwise direction (z) as depicted in Figure 3-2. The resulting flow is statistically two-dimensional. However, due to practical constraints, laboratory experiments are carried out using a rectangular nozzle of height (h) and width (w) and are often confined between sidewalls as shown in Figure 3-3. Such an arrangement has been used in all the experimental studies mentioned above and range in aspect ratios ($AR = w/h$) from 19-102. While most authors simply assume that the AR is large enough to neglect any effect of sidewalls on their results, a quantitative estimate of the AR that ensures that the flow can still be approximated as statistically two-dimensional is needed. Moreover, with recent progress in the area of particle-laden jet flows, many workers resort to using a geometry similar to Figure 3-3 with much smaller AR s (on the order of 2) which enables optical access to specific regions within the dense flows, but still assume two-dimensionality [26, 36]. Hence, it is essential to quantify how small one may make the AR and still expect the flow behavior to be free from the influence of sidewalls for the streamwise distances where measurements are made.

The relevant works which have looked into this issue include Hitchman *et al.* [46], Alnahhal and Panidis [47], Krothapalli *et al.* [48] and Deo *et al.* [49]. Hitchman *et al.* [12] compared a planar jet with and without sidewalls for a nozzle aspect ratio of 60. They made measurements of the mean centerline velocity up to a dimensionless streamwise distance of 80 and found a greater decay rate for the confined jet compared to a jet issuing into a free stream. Alnahhal and Panidis [47] performed an experiment similar to Hitchman *et al.* [46] for a nozzle aspect ratio of 15. They made mean centerline velocity measurements up to a dimensionless streamwise distance of 30 and found an

influence of the sidewalls on the jet flow behavior. Unfortunately, the findings of Hitchman *et al.* [46] and Alnahhal and Panidis [47] are not directly comparable to the present study, as these studies explored deviations in the flow between a free jet and a confined jet versus a confined jet at different aspect ratios, as investigated here.

Krothapalli *et al.* [48] performed experiments with varied jet aspect ratios, but with no sidewalls, and found that the flow is characterized by three distinct regions- the potential core, the 2D self-preserving and the axisymmetric self-preserving regions, and that the onset of the axisymmetric region is a function of aspect ratio. An experimental study similar to Krothapalli *et al.* [48] was attempted in the presence of sidewalls by Deo *et al.* [49]. They found that an increase in the AR leads to an increase in the length of the potential core region, virtual origin and magnitude of mean field troughs in skewness and spikes in flatness. They concluded that even an AR of 72 is insufficient to ensure statistical two-dimensionality within a distance of 85 jet diameters. Although the experiments by Deo *et al.* [49] are directly comparable to the present investigation, their findings imply that most of the benchmark experimental data for planar jet flow (e.g. Gutmark and Wygnakasi [34]) are significantly influenced by the presence of sidewalls. Hence, this conclusion is difficult to accept, and suggests that their experiments may have been affected by initial conditions in the process of varying the AR .

One major drawback in literature with regard to studies on the influence of boundary conditions on planar jet flows is the absence of any numerical study. Numerical turbulence models provide a simplistic and definitive way of ensuring uniform initial conditions and are thus advantageous to independently identify the influence of the experimental domain. Their performance, especially that of k-epsilon model, in

predicting free-shear and wall bounded flows has been well-established over the years [50]. The present study attempts at filling this apparent void through a computational fluid dynamic study on the effect of aspect ratio on rectangular jets with sidewalls.

Simulation Setup

The simulation domain and boundary conditions that were employed are shown in Figure 3-4. Since the aim of the present work is to study the effects of sidewalls alone, the domain was made very large in the x and y directions so that the solution is unaffected by boundary conditions imposed at $x = L$ and $y = H$. Top-hat inlet conditions for the mean velocity and turbulence were imposed at the jet orifice corresponding to a Reynolds number, $Re_j = 67,344$. The input parameters are summarized in Table 3-1. Seven different aspect ratios of $AR = 2, 4, 8, 12, 16, 20$ and 40 were considered. The code used for the numerical simulation is a United States Department of Energy open source code called Multiphase Flows with Interphase Exchanges (MFX) [51], which takes a finite volume approach to solve the three-dimensional Reynolds averaged Navier-Stokes equations coupled with the k-epsilon turbulence model. Standard wall functions are incorporated with the k-epsilon model. The constants in the k and ϵ equations were the default values of $C_{1\epsilon} = 1.44$, $C_{2\epsilon} = 1.92$, $C_\mu = 0.09$, $\sigma_k = 1.0$ and $\sigma_\epsilon = 1.3$. A detailed description of the k-epsilon model and wall functions employed can be found in the MFX documentation (<https://mfix.netl.doe.gov>). After specifying stagnant initial conditions, the model equations were solved in a transient and compressible fashion and each simulation was run till a steady state was reached. The maximum residual at convergence was $1e-3$ for the continuity and momentum equations combined and $1e-4$ for the k and epsilon equations. A structured but non-uniform mesh of 504,000 grids with more grids close to the jet centerline was chosen after ensuring

that the mesh produced a grid insensitive solution. Each simulation took approximately 10 days corresponding to 0.5 s of simulation time running in a parallel mode on two, 2.8 GHz Intel Core processors at the University of Florida high performance cluster.

Validation

To evaluate the performance of the k-epsilon model in capturing the bounded 3D free-shear flow, a comparative study is performed using OpenFoam [52] with two other commonly accepted high Re turbulence models with standard wall functions, namely, the k-omega [53] and the LRR Reynolds-stress models [54]. The OpenFoam simulations employ the same boundary conditions, mesh, and residuals criteria as the MFX simulations. The simulation took approximately 3 days for the two-equation models and 7 days for the Reynolds stress model on a 2.8 GHz Intel Core processor. The results are plotted in Figure 3-5. The small variation in the k-epsilon results between OpenFoam and MFX is attributed to the difference in the numerical discretization method employed. While both OpenFoam and MFX are based on the SIMPLE algorithm [55] and both use first-order Gauss upwind and Gauss linear discretization schemes for the convection and diffusion terms respectively, they differ in time discretization, the places where the field variables are stored and the way boundary conditions are imposed. OpenFoam employs a collocated grid arrangement compared to MFX's staggered grid and does not use a ghost cell approach to impose boundary conditions as done in MFX. Experimental data of Gutmark and Wygnanski [34], involving planar jet studies with a top hat turbulent inlet profile and an AR of 38, are also shown for validation of the turbulence models and the numerical schemes. The k-omega model for $AR = 40$ performs poorly as it overestimates the centerline velocity decay rate, turbulent kinetic energy intensity, as well as the jet half-width when

compared to the k-epsilon and the Reynolds stress models, and the experimental data. The $AR = 40$ and $AR = 2$ behavior captured by the k-epsilon matches reasonably well with the Reynolds-stress model suggesting that there is no significant shortcoming in the k-epsilon model by assuming the eddy-viscosity approximation and its associated assumption of isotropy.

Results

Figure 3-6 shows the variation in the streamwise mean velocity, turbulent kinetic energy and jet half-width, respectively, as a function of downstream distance for different AR s at $y = 0$ and $z = w/2$ (centerline). The results of a two-dimensional simulation, where the transport equations along the z -direction are not solved, are taken to be representative of a truly planar solution and added in the plots. Figure 3-6a shows that in the planar solution, as one would expect, the mean velocity scales as $x^{-1/2}$ everywhere except in the so-called potential core region, which ends approximately 8 jet diameters from the orifice. It is evident from these plots that all AR s follow two-dimensional behavior up to a certain streamwise distance after which they gradually deviate. The high AR s of 40 and 20 show very minimal deviation within the streamwise distance considered, except in the turbulent kinetic energy intensity (Figure 3-6b). The deviation from planar behavior shown by the small AR s of 2, 4, 8, 12 and 16 is characterized by a decrease in centerline decay rate (Figure 3-6a), drop in turbulent kinetic energy intensity (Figure 3-6b) and a decrease in jet half-width (Figure 3-6c). Sensitivity to the input parameters were probed by halving the inlet Reynolds number (Re_j), turbulent kinetic energy (k_j) and dissipation (ϵ_j) for the case of $AR = 2$ and negligible difference was observed suggesting that these results are not dependent on the exact values of the inlet parameters.

Analysis and Discussion

In order to explain the observed influence of spanwise bounding width on the jet behavior, an order of magnitude approach is undertaken. All the terms in the governing equations are back-calculated using simple finite difference approximations from the solution grid. Since a two-equation turbulence model is employed, the Reynolds stresses can be written using the eddy viscosity assumption as

$$-\overline{u_i u_k} = -\frac{2}{3} k \delta_{ik} + \nu_T \left(\frac{\partial \overline{U}_i}{\partial x_k} + \frac{\partial \overline{U}_k}{\partial x_i} \right) \quad (3-1)$$

Now, the momentum equation along the x direction yields

$$\begin{aligned} U \frac{\partial U}{\partial x} + V \frac{\partial U}{\partial y} + W \frac{\partial U}{\partial z} + \frac{2}{3} \frac{\partial k}{\partial x} + \frac{\partial}{\partial x} \left[-2\nu_T \left(\frac{\partial U}{\partial x} \right) \right] + \frac{\partial}{\partial y} \left[-\nu_T \left(\frac{\partial U}{\partial y} + \frac{\partial V}{\partial x} \right) \right] \\ + \frac{\partial}{\partial z} \left[-\nu_T \left(\frac{\partial U}{\partial z} + \frac{\partial W}{\partial x} \right) \right] = -\frac{1}{\rho} \frac{\partial P}{\partial x} + \nu \left[\frac{\partial^2 U}{\partial x^2} + \frac{\partial^2 U}{\partial y^2} + \frac{\partial^2 U}{\partial z^2} \right] \end{aligned} \quad (3-2)$$

Also noting that for the k -epsilon model, the turbulent viscosity is given by

$$\nu_T = C_\mu k^2 / \varepsilon \quad (3-3)$$

At the centerline ($y = 0$, $z = w/2$), the most significant terms of Eq. 3-2 are plotted in Figure 3-7a for $AR = 40$ and in Figure 3-7b for $AR = 2$. The momentum budget along the centerline is primarily satisfied by a balance between the streamwise convection term, $U \frac{\partial U}{\partial x}$, and the transverse (y) turbulent diffusion term, $\nu_T \frac{\partial^2 U}{\partial y^2}$. The pressure and turbulent kinetic energy terms are seen to play a role only very close to the jet inlet, within the potential core region. The spanwise (z) turbulent diffusion term, $\nu_T \frac{\partial^2 U}{\partial z^2}$ is zero throughout the centerline suggesting the lack of development of a significant velocity profile in the z direction within the streamwise length L considered. On the other hand, in Figure 3-7b, when $AR = 2$, the spanwise turbulent diffusion term, $\nu_T \frac{\partial^2 U}{\partial z^2}$, plays a

significant role in the momentum budget throughout the centerline except close to the jet orifice. Focusing in on the region $x/h > 20$ (Figure 3-8) reveal that at upstream locations ($x/h \sim 20-50$), the role of the spanwise turbulent diffusion term in $AR = 2$ (Figure 3-8b) is to reduce the streamwise convection term when compared to $AR = 40$ (Figure 3-8a). The spanwise turbulent diffusion term helps balance the transverse turbulent diffusion term, which remains roughly unchanged in both cases. Thus, the decrease in the rate of centerline decay observed in the streamwise mean velocity for small AR s can be attributed to the reduction in the streamwise convective term by the spanwise turbulent diffusion term.

Similarly, an order of magnitude analysis of the terms in the turbulent kinetic energy equation is performed as follows. The turbulent kinetic energy equation for the k -epsilon model with $\sigma_k = 1$ is

$$\begin{aligned} \frac{\partial k}{\partial t} + U \frac{\partial k}{\partial x} + V \frac{\partial k}{\partial y} + W \frac{\partial k}{\partial z} \\ = \frac{\partial}{\partial x} \left[(v + v_T) \frac{\partial k}{\partial x} \right] + \frac{\partial}{\partial y} \left[(v + v_T) \frac{\partial k}{\partial y} \right] + \frac{\partial}{\partial z} \left[(v + v_T) \frac{\partial k}{\partial z} \right] + P_k - \varepsilon \end{aligned} \quad (3-4)$$

where the production term is given by

$$\begin{aligned} P_k = 2v_T \left[\left(\frac{\partial U}{\partial x} \right)^2 + \left(\frac{\partial V}{\partial y} \right)^2 + \left(\frac{\partial W}{\partial z} \right)^2 \right] + v_T \left(\frac{\partial U}{\partial y} + \frac{\partial V}{\partial x} \right)^2 + v_T \left(\frac{\partial U}{\partial z} + \frac{\partial W}{\partial x} \right)^2 \\ + v_T \left(\frac{\partial W}{\partial y} + \frac{\partial V}{\partial z} \right)^2 \end{aligned} \quad (3-5)$$

The major terms in the energy budget at $y = 0$ are shown for $AR = 40$ and $AR = 2$ in Figure 3-9. The energy equation is satisfied primarily by a balance in the streamwise convective term, $U \frac{\partial k}{\partial x}$, the transverse turbulent diffusion term, $v_T \frac{\partial^2 k}{\partial y^2}$, the spanwise turbulent diffusion term, $v_T \frac{\partial^2 k}{\partial z^2}$ and the dissipation term, ε . Analogous to the momentum

budget, while the role of the spanwise turbulent diffusion term is absent for $AR = 40$, it is significant when $AR = 2$. Figure 3-10 which focuses in on the region upstream of the centerline ($x/h \sim 20-50$) reveal that the role of the spanwise turbulent diffusion term in the energy budget of $AR = 2$ is to increase the magnitude of the streamwise convection term when compared to $AR = 40$. This increase in streamwise convective decay of turbulence, supplemented by a reduction in the centerline mean velocity decay (Figure 3-6a) is responsible for the drastic drop in the turbulent kinetic energy intensity observed in Figure 3-6b for small AR s.

Finally, the observation of reduced half-width for small AR s (Figure 3-6c) can be explained through an order of magnitude analysis of terms in the streamwise momentum equation (Eq. 3-2) at a fixed x location. The momentum budget at $x = 71h$ and $z = w/2$ is shown for $AR = 40$ and $AR = 2$ in Figure 3-11. At this downstream location, two additional convective terms, namely the transverse convection due to mean velocity, $V \frac{\partial U}{\partial y}$, and the transverse convection due to turbulent viscosity gradient, $\left(\frac{\partial v_T}{\partial y}\right) \left(\frac{\partial U}{\partial y}\right)$, are also significant. Again the spanwise turbulent diffusion term, $v_T \frac{\partial^2 U}{\partial z^2}$ in $AR = 2$, is responsible for increasing the magnitude of the transverse convection terms when compared to $AR = 40$. This results in greater shear and steeper fall in the streamwise velocity along the transverse direction, giving rise to the reduced jet half-width at small AR s.

Thus, the findings of an order of magnitude analysis of the streamwise momentum budget at $y = 0$, $z = w/2$ and $x = 71h$, $z = w/2$ and the turbulent kinetic energy budget at $y = 0$, $z = w/2$ suggests that the mean and turbulent velocity profiles which develop along the spanwise (z) direction due to the high Reynolds number flow between the

bounding walls, analogous to the developing flow between parallel plates, are responsible for causing a reduction in streamwise momentum and turbulent energy convection and an increase in transverse momentum convection.

Now, having established that the influence of the bounding walls at the centerline is through the spanwise turbulent diffusion terms, $\nu_T \frac{\partial^2 U}{\partial z^2}$ and $\nu_T \frac{\partial^2 k}{\partial z^2}$ in the mean velocity and turbulent kinetic energy equations respectively, it is possible to find the exact streamwise location where these terms become significant for different AR s. This is done by comparing them to the corresponding transverse diffusion terms, $\nu_T \frac{\partial^2 U}{\partial y^2}$ and $\nu_T \frac{\partial^2 k}{\partial y^2}$ which are known to be important.

Figure 3-12 shows the streamwise distance when the spanwise diffusion terms become 10% of the corresponding transverse terms as a function of AR . It is seen that spanwise width first affects the mean velocity equation before affecting the turbulence energy as one moves downstream and both show a linear variation with AR . The AR and range of x/h used in some published experimental papers are also shown in Figure 3-12. It is evident that most turbulent jet works are well inside the region which is free from the influence of bounding walls, except Mychkovsky (2010), which lies on the borderline and is still estimated to have minimal wall influence.

Summary

There exists a need to quantify how wide an experimental setup of a rectangular jet with sidewalls can be to accurately assume two-dimensionality, especially when measurements are being made at high streamwise distances. A computational fluid dynamics study using a standard k-epsilon turbulence model was conducted in order to

address this issue. It was found that the turbulent shear/diffusion terms in the spanwise direction arising from the developing flow between the bounding walls cause a decrease in the mean velocity decay rate and a drop in turbulent kinetic energy intensity along the centerline, as well as a decrease in jet half-width when compared to the planar case. The exact streamwise distance where these terms become significant was estimated as a function of jet nozzle aspect ratio. It was found that the most widely accepted single-phase planar jet studies found in literature lie in the region free from the influence of bounding walls. The performance of the k-epsilon model in predicting such a flow was also evaluated favorably.

Thus, the results of a single-phase k-epsilon study suggests negligible role of sidewalls in the experimental setup employed in Chapter 2. In the Chapter 4, a gas-solid continuum model is evaluated against collected experimental data. Two-dimensionality has been assumed in the simulations.

Table 3-1. Input parameters corresponding to an inlet jet Reynolds number Re_j of 67,344.

Parameter	Description	Value
U_j	Jet inlet velocity	90 m/s
k_j	Inlet turbulent kinetic energy	19 m ² /s ²
ϵ_j	Inlet turbulence dissipation	2.164e4 m ² /s ³
ρ_j	Inlet density	1.342 kg/m ³
$h/2$	Half-height of the jet	4.6 mm
L	Length	1 m
H	Height	1 m
w	Width	Varied
μ	Viscosity	1.65e-5 kg/(ms)
T	Gas temperature for ideal gas equation	-5 °C
MW	Molecular weight for ideal gas equation	29 g/mol
P_o	Outlet pressure	1.013e5 Pa

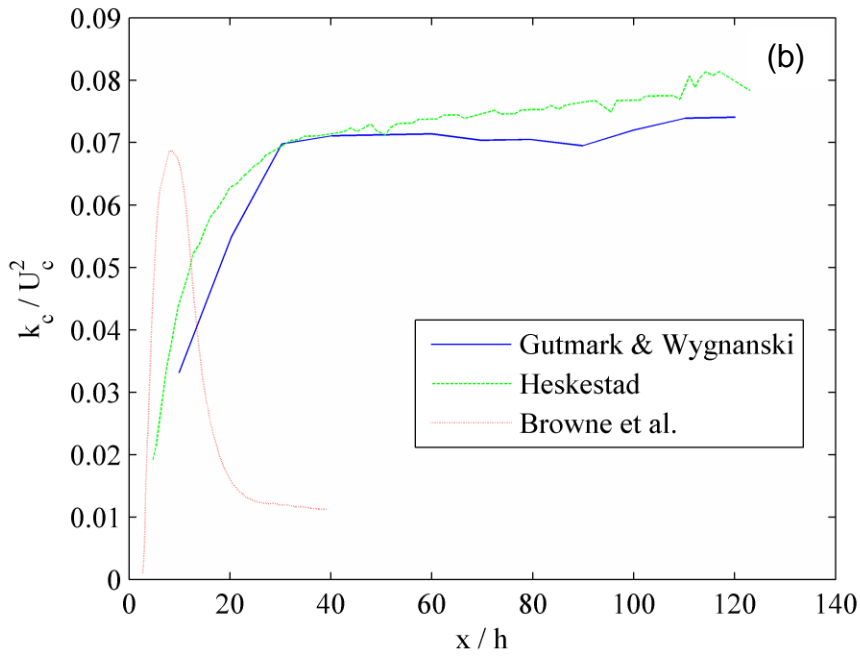
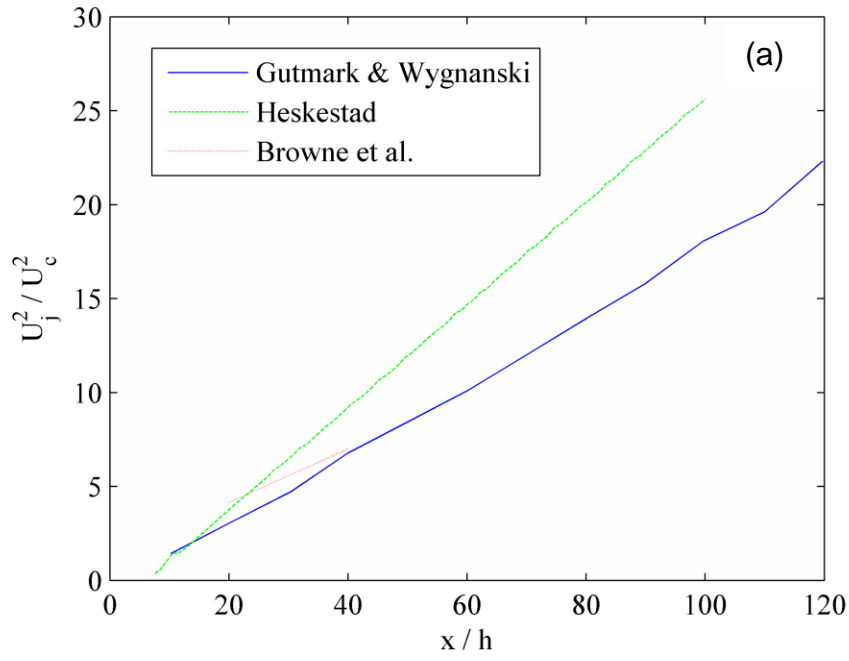


Figure 3-1. Influence of initial conditions. (a) Mean velocity decay along the centerline. (b) Turbulent kinetic energy intensity evolution along the centerline.

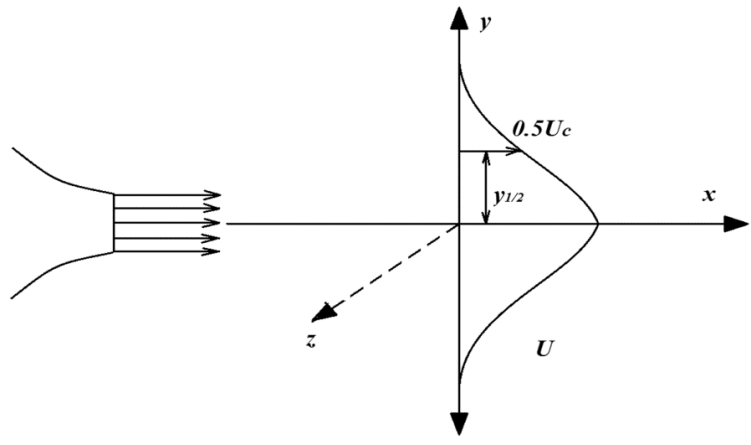


Figure 3-2. An ideal planar jet.

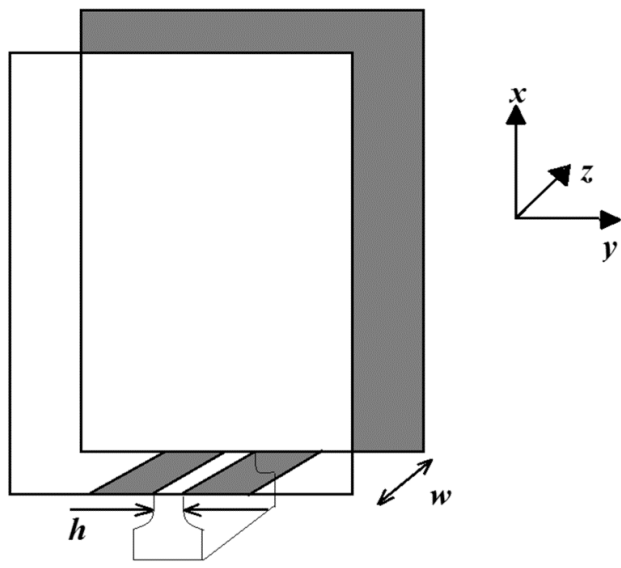


Figure 3-3. Typical laboratory setup.

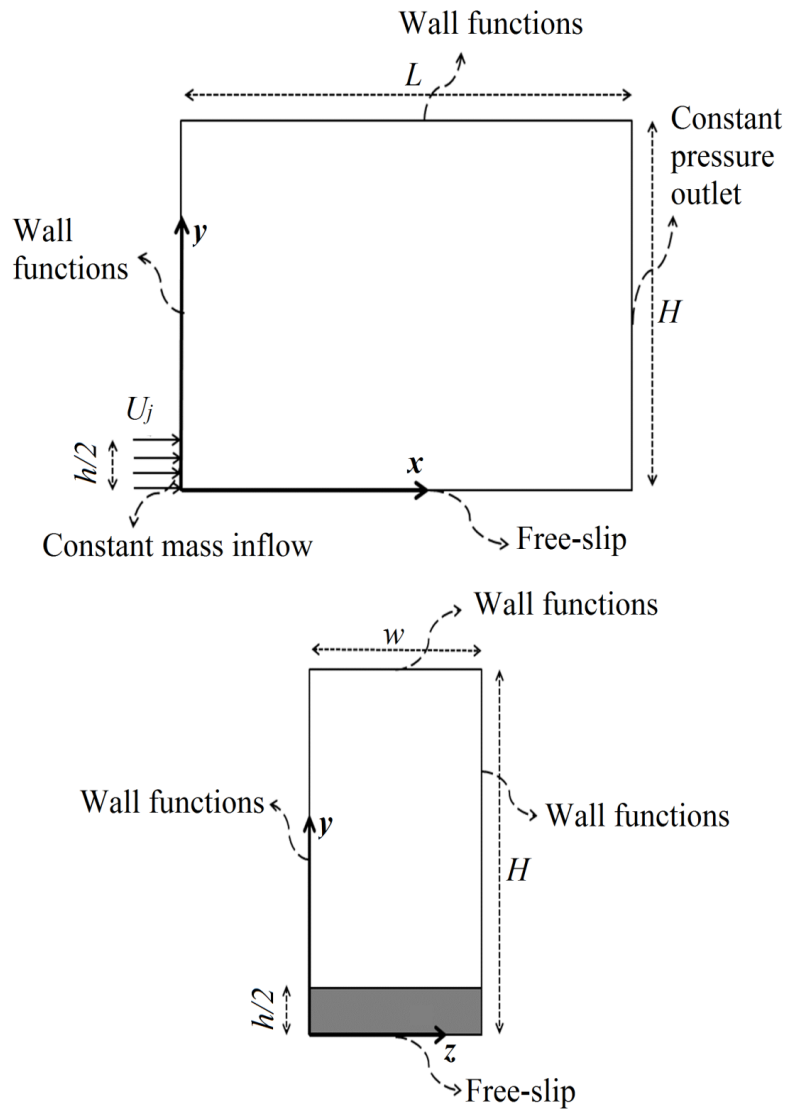


Figure 3-4. Simulation domain and boundary conditions.

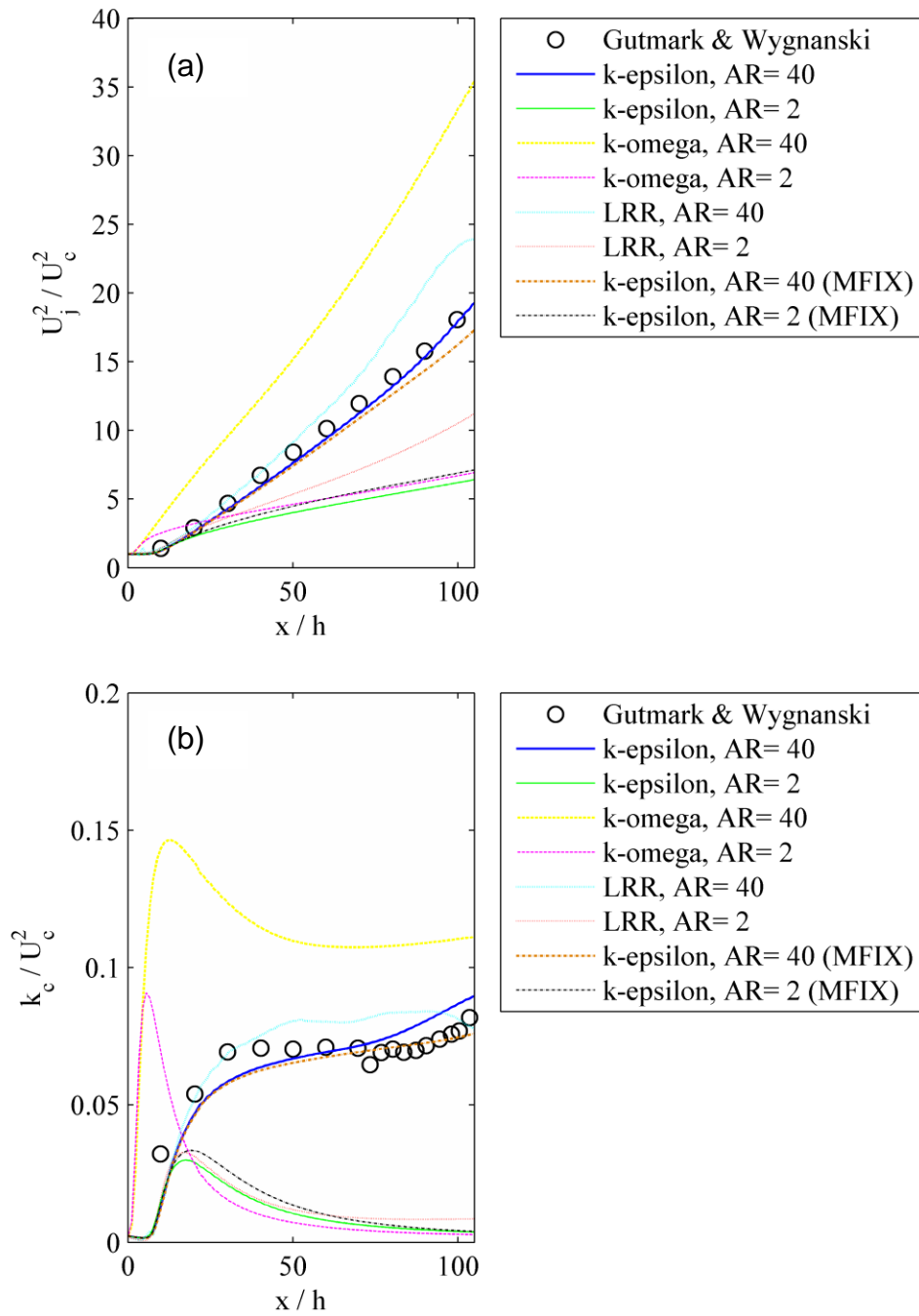


Figure 3-5. Validation of k-epsilon model. (a) Centerline decay in mean streamwise velocity. (b) Centerline turbulent intensity evolution. (c) Evolution of half-width.

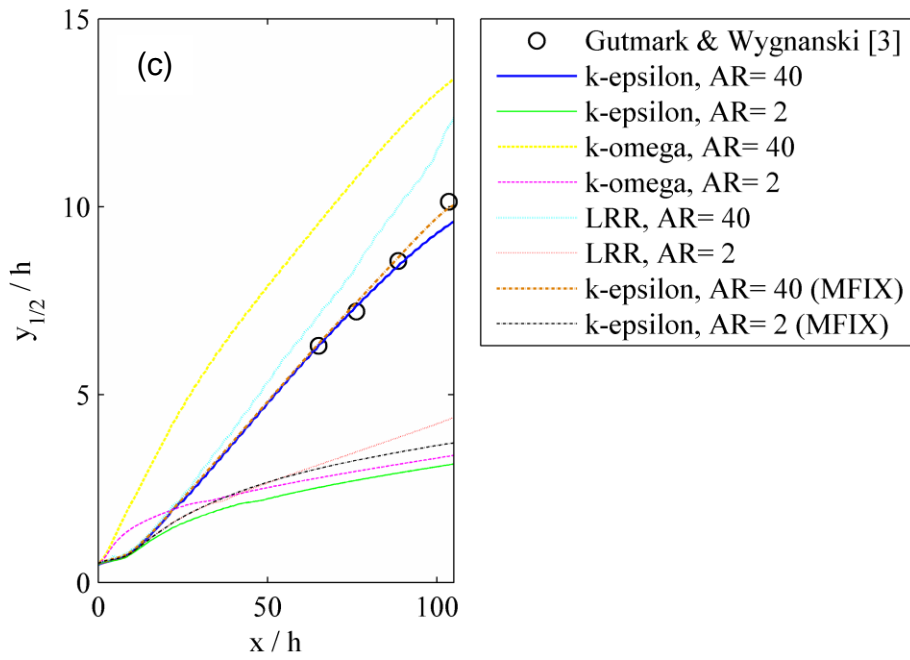


Figure 3-5. continued.

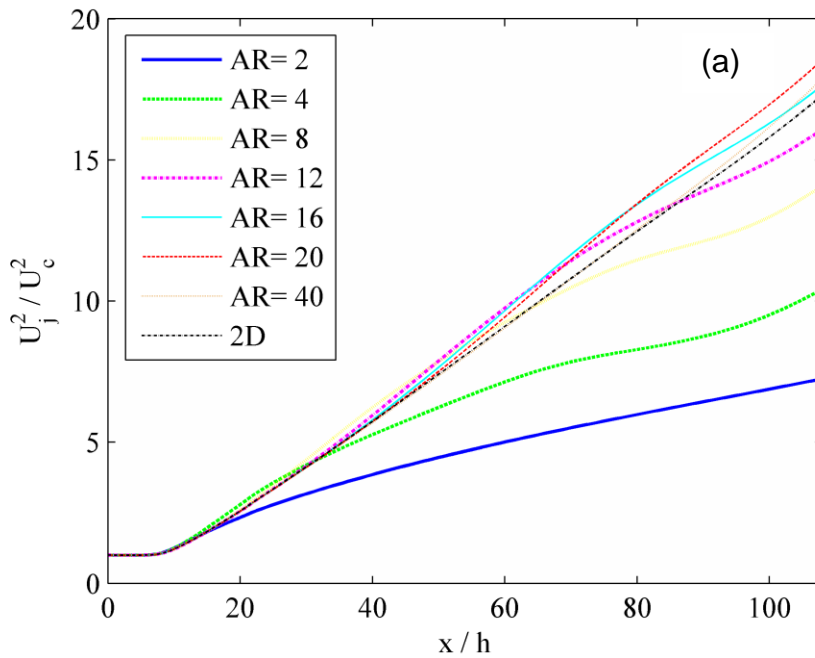


Figure 3-6. Effect of aspect ratio. (a) Centerline mean velocity decay. (b) Evolution of turbulent kinetic energy along the centerline. (c) Streamwise evolution of jet half-width.

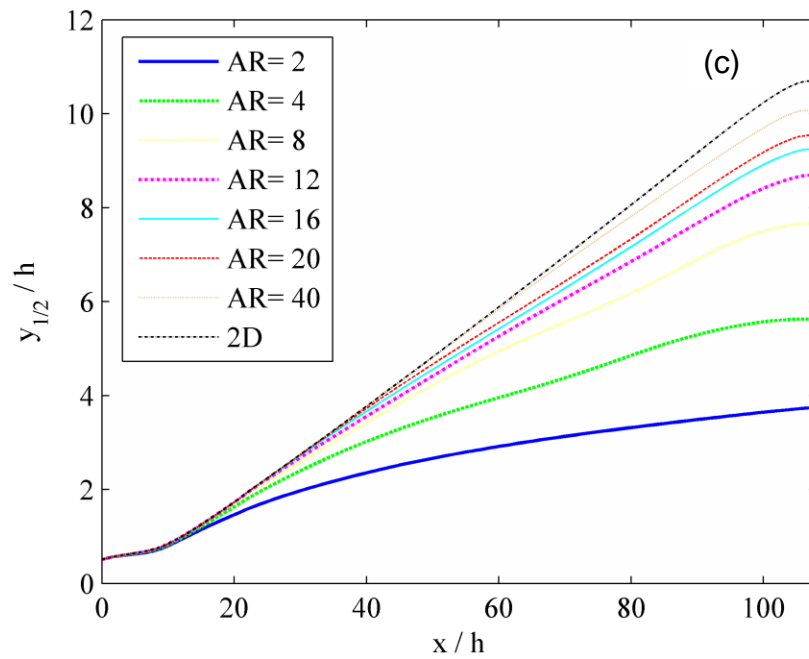
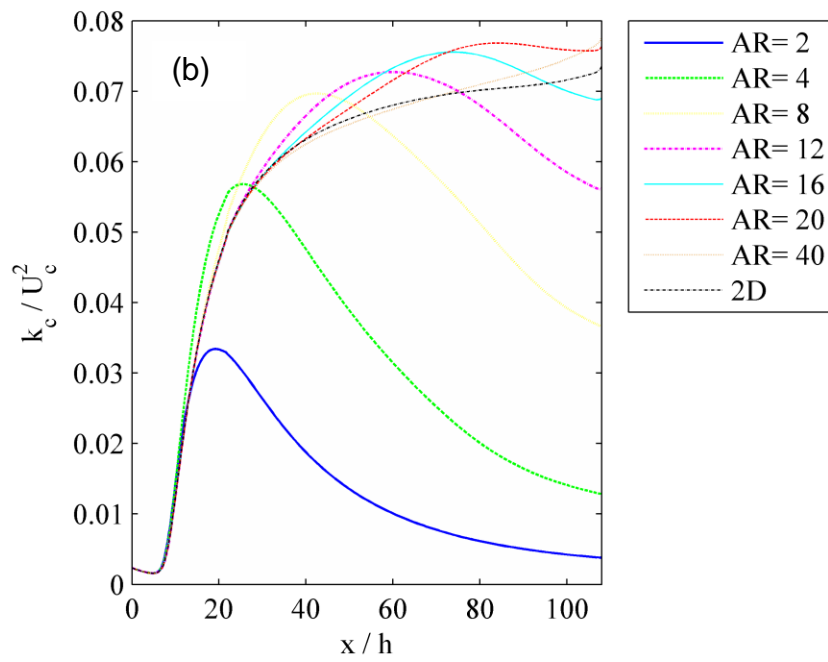


Figure 3-6. continued.

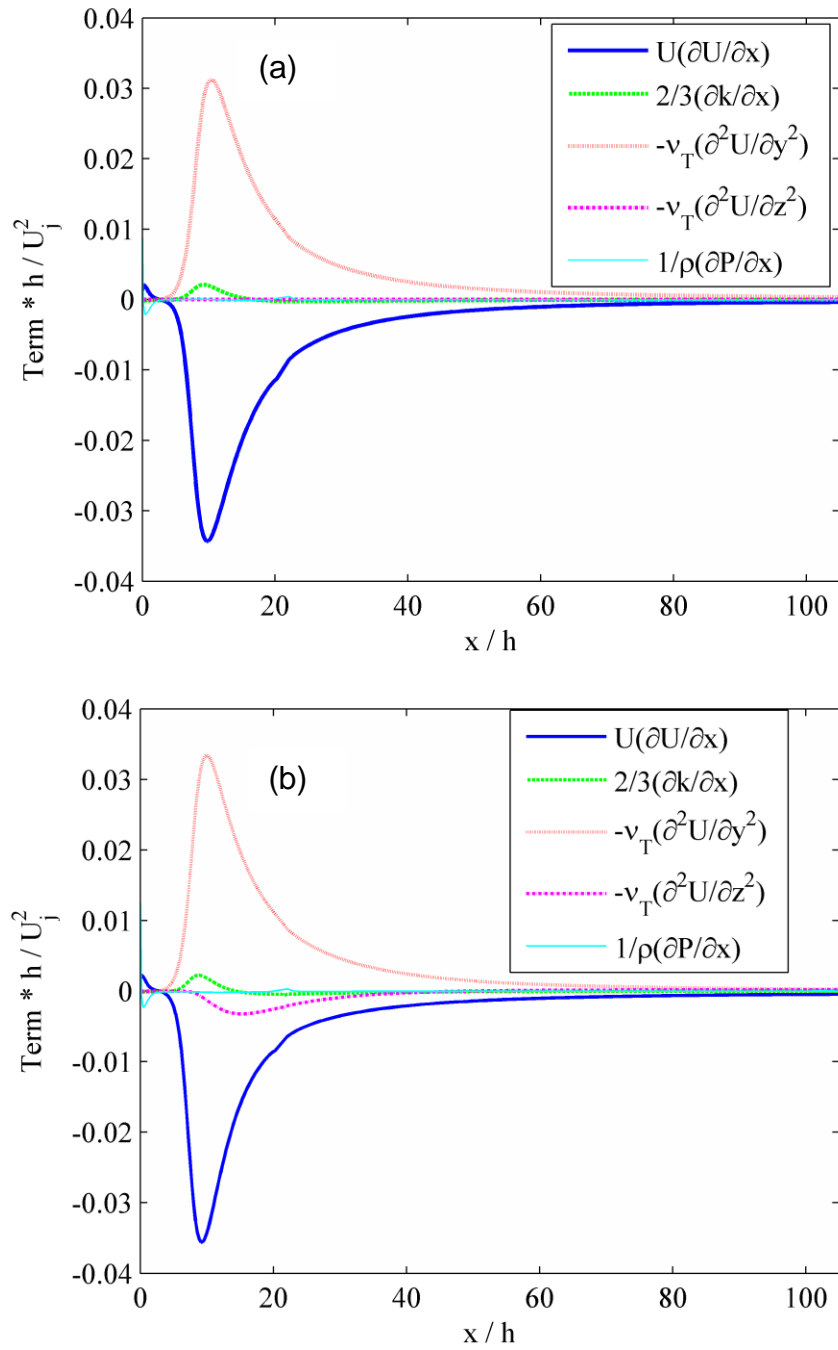


Figure 3-7. Momentum budget along the centerline ($y = 0$, $z = w/2$). (a) $AR = 40$. (b) $AR = 2$.

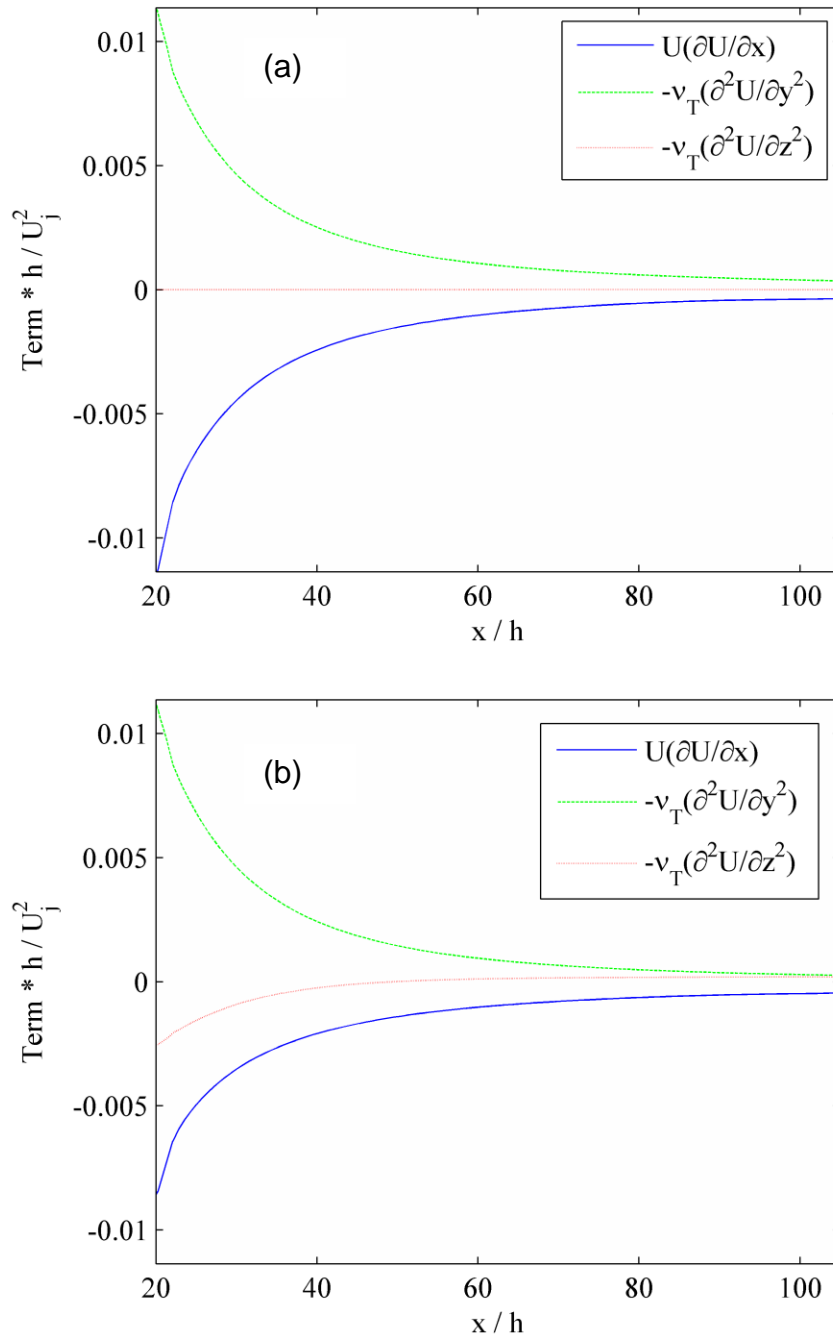


Figure 3-8. Momentum budget along the centerline ($y = 0$, $z = w/2$). (a) $AR = 40$. The spanwise turbulent diffusion term is absent. (b) $AR = 2$. The spanwise turbulent diffusion term plays a significant role.

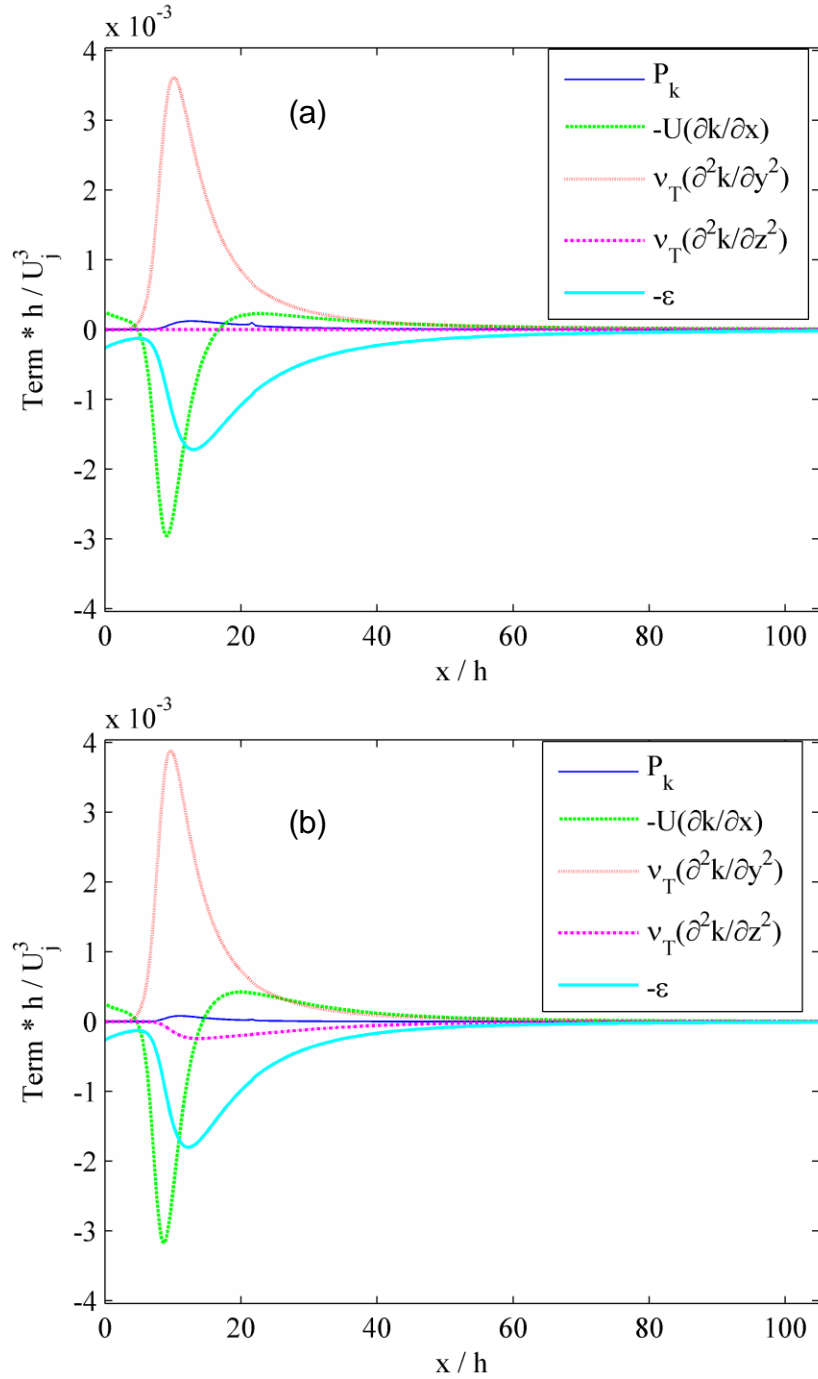


Figure 3-9. Turbulent energy budget along the centerline ($y = 0, z = w/2$). (a) $AR = 40$.
 (b) $AR = 2$.

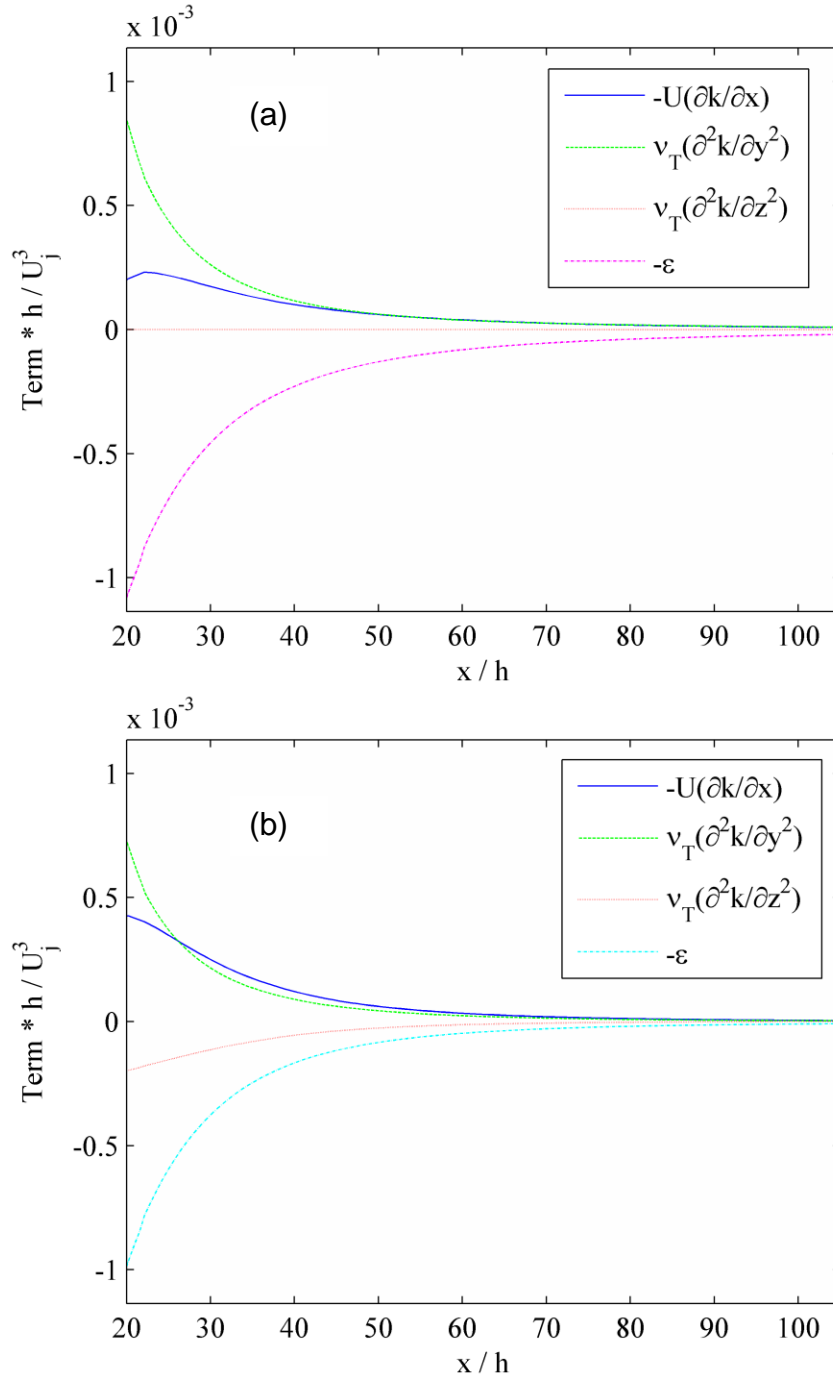


Figure 3-10. Turbulent energy budget along the centerline ($y = 0, z = w/2$). (a) $AR = 40$. The spanwise turbulent diffusion term is absent. (b) $AR = 2$. The spanwise turbulent diffusion term plays a significant role.

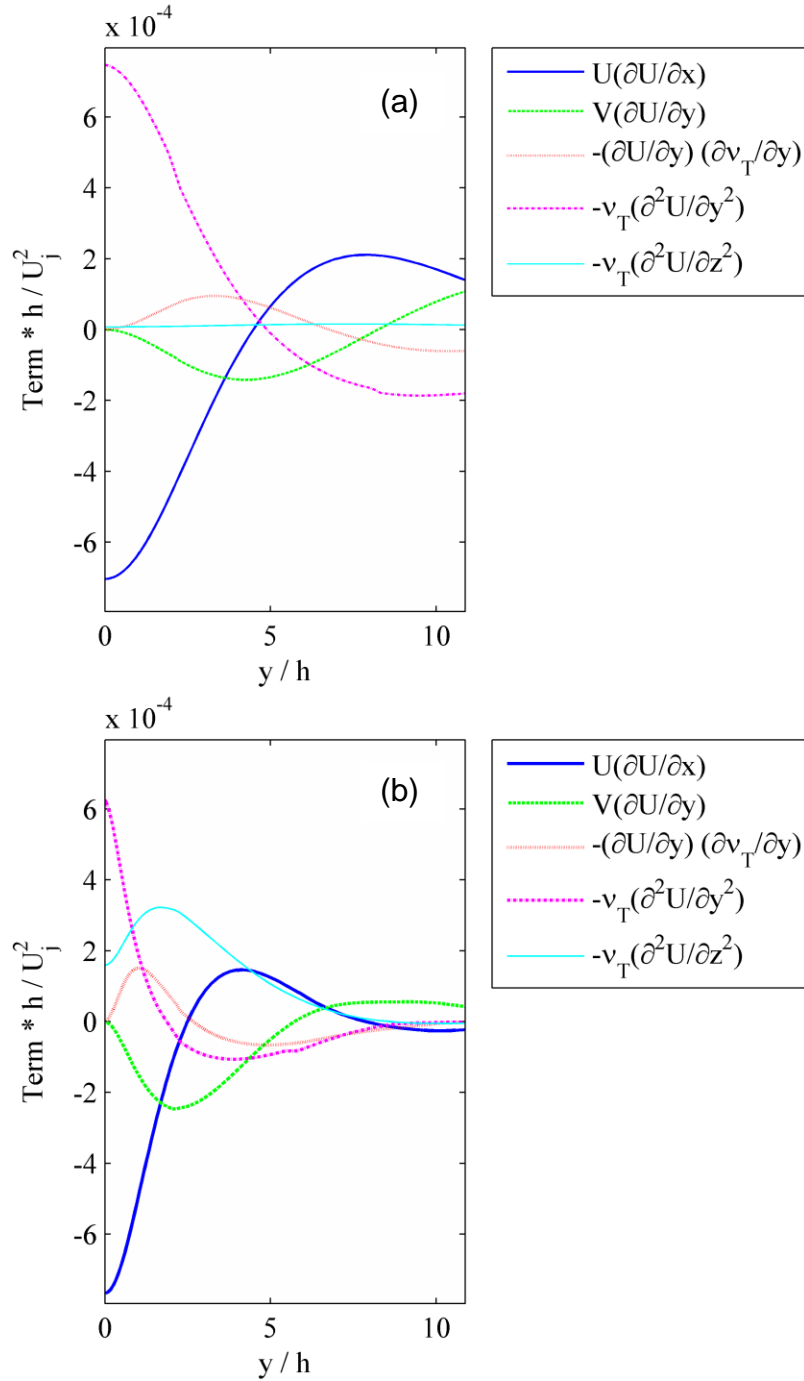


Figure 3-11. Momentum budget at $x = 71h$ and $z = w/2$. (a) $AR = 40$. The spanwise diffusion term is absent. (b) $AR = 2$. The spanwise diffusion term plays a significant role.

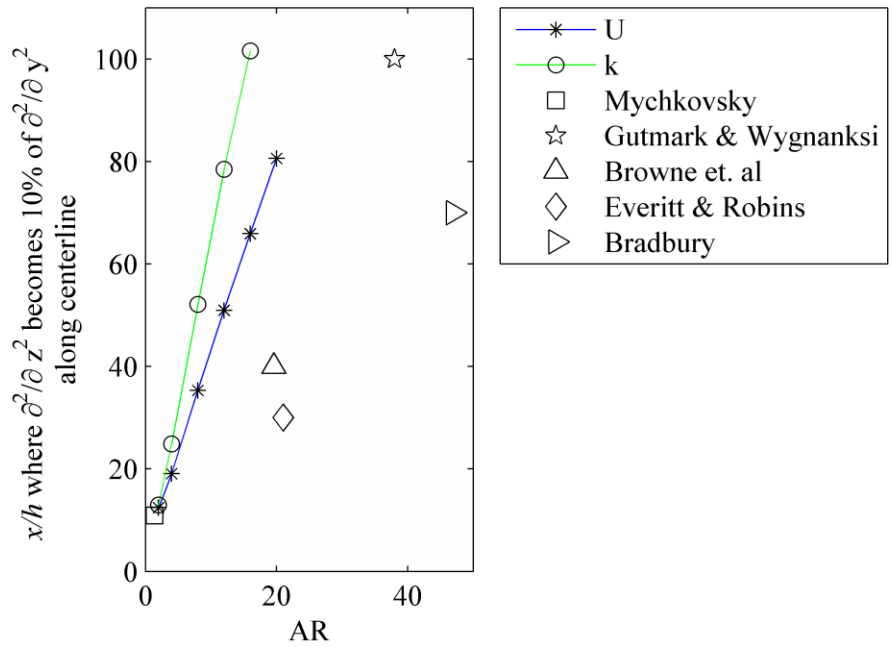


Figure 3-12. Plot showing the minimum value of AR which can be considered unaffected by bounding wall influence for a given x/h .

CHAPTER 4 VALIDATING A GAS-SOLID CONTINUUM MODEL

Background

As mentioned in Chapter 1, continuum modeling, where the particles are assumed to form a continuous fluid-like phase, is the preferred modeling approach for bubbling beds. Constitutive relations are therefore necessary to close the continuum equations. However, appropriate description of these closure relations is a major challenge with continuum modeling.

The closure models required in the continuum framework are solid-phase kinetic and collisional stress, solid-phase frictional stress, gas-phase stress and gas-solid drag. Further, if the gas phase is turbulent, a two-phase turbulence model that accounts for fluctuating energy transfer between the two phases is also required. An overview of closure model descriptions that have been employed in the continuum framework can be found in Curtis and van Wachem [13], van Wachem and Almstedt [7] and van Wachem *et al.* [16]. Closure models can be characterized as well-established or not well-established based on three factors – physical basis of their derivation, existence of empirical parameters, and the flow regimes, particularly concentration range, over which they have been tested. As will be noted when describing the continuum model later in this work, while the descriptions for solid-phase kinetic and collisional stress, gas-phase stress and gas-solid drag can be considered fairly well-established, the main uncertainties lie in the descriptions for solid-phase frictional stress and turbulence interaction. In predominantly dense flows ($\epsilon_s > 20\%$) the gas phase turbulence may be neglected and in relatively dilute flows ($\epsilon_s < 50\%$) the frictional contribution to solid stress can be neglected. However, in bubbling flows with a high-speed jet injection, the

solids volume fraction ranges from less than 1% in the jet plume region to close to maximum packing in the dense emulsion region, hence both these closures are significant in accurately predicting the flow details (Figure 4-1).

Since continuum modeling fundamentally assumes that particles behave like a continuous fluid phase and encompasses some empiricism in closure relations, validating model predictions against experimental measurements is crucial in identifying the detail to which continuum modeling can be successfully applied. Validation studies involving continuum modeling of gas-solid bubbling bed flows have been conducted by numerous authors as discussed below.

Bubbling bed flows can be generally classified as uniformly fluidized beds and jet injection studies. Continuum modeling of bubbles formed in uniform fluidized beds compare model predictions and experimental measurements of bubble size, bubble shape, bed expansion, bubble rise velocity, solids distribution and bed dynamics [14-16, 56, 57]. Experimental data are typically obtained from a variety of imaging techniques such as radioactive particle tracking, optical probe, and electrical capacitance tomography. Validation studies involving jet injection into a packed bed have been mostly spouted bed studies [17-19, 58-61]. These compare fountain height, spout diameter and minimum spouting velocity using data from digital camera and pressure transducer [18, 58]. More detailed evaluations of solids concentration, particle velocity and granular temperature profiles have been made inside the spout region with the help of experimental data obtained from optical fiber probe and PIV techniques [17, 19, 59-61]. However, no comparisons were made against gas velocity profiles. In the case of jet injection into a fluidized bed leading to a single bubble formation, comparisons

between model and experiments have been made for bubble size and shape [16] and also time-averaged porosity distribution as new bubbles form and rise continuously [20, 62]. The experimental data used for validation come from high-speed camera and optical probe measurements made for a jet injection velocity of 10 m/s and at minimum fluidization conditions. In the case of jet injection leading to spout formation in fluidized beds the vector plot of particle movement near the spout and area-averaged particle flux have been validated against experimental PIV measurements by Zhonghua and Mujumdar [60]. In their study, a jet velocity of 20 m/s was considered at a fluidization ratio of 1.5 times the minimum fluidization velocity. While most studies concerning jet injection into a fluidized bed deal with relatively low jet velocities (less than 20 m/s) where the turbulence in the gas phase is typically suppressed by particles, a few continuum modeling studies of high-speed jet injection can be found in literature [3, 63]. Horizontal jets of velocity up to 250 m/s injected into a fluidized bed were modeled and evaluations were made only against macroscopic properties of jet penetration length and expansion angle.

To summarize earlier validation studies, even the most detailed comparisons between experiment and continuum modeling of bubbling bed flows have been limited to particle velocity and granular temperature profiles. Also, there are very few works that evaluate high-speed jet injection into a fluidized bed. In the present study, both gas and particle, mean and fluctuating velocity profiles inside a high-speed jet plume with varying fluidization levels are evaluated against the recent experimental work that employed laser Doppler velocimetry [27, 37]. The experiments also provide the

fluidization curve measured using a pressure gauge and digital videos of particle movement.

The aim of the present work is two-fold:

- To determine appropriate closure relations that are necessary in a continuum model to describe bubbling beds with a high-speed jet injection, by conducting a series of test cases with increasing complexity.
- Evaluate the bubbling bed continuum model predictions against two-phase experimental velocity measurements which have been made at a detailed level.

Model Description

Governing Equations

The governing equations follow from the volume averaged equations of Anderson and Jackson [64] applied to gas-solid flows. Continuity and momentum balance equations are solved for each phase as shown below.

$$\frac{\partial \varepsilon_g}{\partial t} + \nabla \cdot (\varepsilon_g \underline{u}_g) = 0 \quad (4-1)$$

$$\frac{\partial \varepsilon_s}{\partial t} + \nabla \cdot (\varepsilon_s \underline{u}_s) = 0 \quad (4-2)$$

$$\rho_g \varepsilon_g \left[\frac{\partial \underline{u}_g}{\partial t} + \underline{u}_g \cdot \nabla \underline{u}_g \right] = -\varepsilon_g \nabla p_g + \nabla \cdot (\varepsilon_g \underline{\underline{\tau}}_g) - \underline{F}_D + \varepsilon_g \rho_g \underline{g} \quad (4-3)$$

$$\rho_s \varepsilon_s \left[\frac{\partial \underline{u}_s}{\partial t} + \underline{u}_s \cdot \nabla \underline{u}_s \right] = -\varepsilon_s \nabla p_g + \nabla \cdot \underline{\underline{\sigma}}_s + \underline{F}_D + \varepsilon_s \rho_s \underline{g} \quad (4-4)$$

Here, t is time, ε_g the gas volume fraction, ε_s solids volume fraction (note that the conservation of total volume requires an additional independent relation between volume fractions such that $\varepsilon_g + \varepsilon_s = 1$), \underline{u}_g the gas mean velocity, \underline{u}_s solids mean velocity, ρ_g the gas density, ρ_s solids density, p_g the gas pressure and \underline{g} the acceleration due to gravity.

In order to close the above set of equations, constitutive relations are needed for the gas-phase stress, $\underline{\tau}_g$, drag force per unit volume, \underline{F}_D , and solid-phase stress, $\underline{\sigma}_s$. The solid-phase stress is further divided into two additive components, the kinetic and collisional component $\underline{\sigma}_s^{kc}$, and the frictional component $\underline{\sigma}_s^f$.

Gas-Solid Drag

Drag models represent the momentum transfer between the mean velocity components of both phases. The drag force per unit volume (\underline{F}_D) is given by,

$$\underline{F}_D = \beta (\underline{u}_g - \underline{u}_s) \quad (4-5)$$

Model development for the friction coefficient β has been mainly semi-theoretical in literature. Drag models contain physical parameters and have been tested over a wide range of flow regimes over the years. Though there are multiple expressions for friction coefficient in literature there is fairly good agreement on the Wen and Yu [65] expression when dealing with fluidization flows [66-69]. Therefore, the well-established Wen and Yu [65] drag expression is used to close the gas-solid drag force in the present continuum model.

$$\beta = \frac{3}{4} C_D \frac{\rho_g \varepsilon_g \varepsilon_s |\underline{u}_g - \underline{u}_s|}{d_p} \varepsilon_g^{-2.65} \quad (4-6)$$

$$C_D = \begin{cases} \frac{24(1 + 0.15Re^{0.687})}{Re}, & Re < 1000 \\ 0.44, & Re > 1000 \end{cases} \quad (4-7)$$

$$Re_p = \frac{d_p \varepsilon_g |\underline{u}_g - \underline{u}_s|}{\mu_g} \quad (4-8)$$

Where d_p = particle diameter, C_D = drag coefficient and Re_p = particle Reynolds number.

Gas-Phase Stress

In order to describe the turbulent gas phase, a standard high Reynolds number k-epsilon model modified to account for the presence of a particle phase is adopted. Such an approach has been successfully employed in many turbulent two-phase flows [59, 69-71].

$$\rho_g \varepsilon_g \left[\frac{\partial k}{\partial t} + \underline{u}_g \cdot \nabla k \right] = \nabla \cdot \left(\varepsilon_g \frac{\mu_g^t}{\sigma_k} \nabla k \right) + \varepsilon_g \underline{\underline{\tau}}_g : \nabla \underline{u}_g - \varepsilon_g \rho_g \varepsilon + \pi_k \quad (4-9)$$

$$\rho_g \varepsilon_g \left[\frac{\partial \varepsilon}{\partial t} + \underline{u}_g \cdot \nabla \varepsilon \right] = \nabla \cdot \left(\varepsilon_g \frac{\mu_g^t}{\sigma_\varepsilon} \nabla \varepsilon \right) + \varepsilon_g \frac{\varepsilon}{k} \left(C_{1\varepsilon} \underline{\underline{\tau}}_g : \nabla \underline{u}_g - \rho_g C_{2\varepsilon} \varepsilon \right) + C_{3\varepsilon} \frac{\varepsilon}{k} \pi_k \quad (4-10)$$

$$\underline{\underline{\tau}}_g = \mu_g^e \left[\nabla \underline{u}_g + \nabla \underline{u}_g^T - \frac{2}{3} (\nabla \cdot \underline{u}_g) \underline{\underline{I}} \right] \quad (4-11)$$

$$\mu_g^t = \rho_g C_\mu \frac{k^2}{\varepsilon}; \mu_g^e = \mu_g + \mu_g^t \quad (4-12)$$

Most terms in the above equations are analogous to the single-phase turbulence model. The k and ε equations represent the balance of convective and diffusive transport with the production and dissipation of turbulent kinetic energy and turbulent energy dissipation respectively. The main change in the two-phase equations is in the presence of a turbulence modulation term, π_k . This term represents the enhancement or damping of turbulent kinetic energy due to the presence of a particle phase. The closure for this term is not well-established in literature and will be discussed in the turbulence interaction terms section. The model constants in the k-epsilon equations are specified to be $\sigma_k = 1.0$, $\sigma_\varepsilon = 1.3$, $C_{1\varepsilon} = 1.44$, $C_{2\varepsilon} = 1.92$, $C_{3\varepsilon} = 1.22$ and $C_\mu = 0.09$.

Solid-Phase Kinetic and Collisional Stress

The stress experienced by the particles due to translation and instantaneous collisions is referred to as solid-phase kinetic and collisional stress ($\underline{\underline{\sigma}}_s^{kc}$). Kinetic and

collisional stress depends on the magnitude of particle velocity fluctuations (\underline{u}'_s), also called granular temperature, θ .

$$\theta = \frac{1}{3} \left(\underline{u}'_s \cdot \underline{u}'_s \right) \quad (4-13)$$

Therefore, a granular energy balance is solved along with the other governing equations.

$$\frac{3}{2} \rho_s \varepsilon_s \left[\frac{\partial \theta}{\partial t} + \underline{u}_s \cdot \nabla \theta \right] = \nabla \cdot (\kappa_s \nabla \theta) + \underline{\underline{\sigma}}_s^{kc} : \nabla \underline{u}_s - \varepsilon_s \rho_s J_s + \pi_\theta \quad (4-14)$$

This balance generates three additional terms that require closure, namely, granular conductivity (κ_s), collisional dissipation (J_s) and the granular temperature modulation (π_θ). The solid-phase kinetic and collisional stress, granular conductivity and collisional dissipation are expressed in terms of granular temperature, in a fashion analogous to the kinetic theory of gases but accounting for inelastic particle collisions and the fact that particles occupy space (Eq. 4-15 to 4-21). These equations were theoretically derived by Lun *et al.* [72] for spherical particles, with restitution coefficient e , in vacuum. A slightly modified version of Lun *et al.* [72] proposed by Agrawal *et al.* [73] that accounts for interstitial gas, is adopted to describe the solids viscosity and solids conductivity in the present study.

$$\underline{\underline{\sigma}}_s^{kc} = \left(-p_s^{kc} + \eta \mu_b^{kc} \nabla \cdot \underline{u}_g \right) \underline{\underline{I}} + \mu_s^{kc} \left[\nabla \underline{u}_s + \nabla \underline{u}_s^T - \frac{2}{3} (\nabla \cdot \underline{u}_s) \underline{\underline{I}} \right] \quad (4-15)$$

$$p_s^{kc} = \varepsilon_s \rho_s \theta (1 + 4\eta \varepsilon_s g_0) \quad (4-16)$$

$$\mu_s^{kc} = \left(\frac{2+\alpha}{3} \right) \left[\frac{\mu_s^{kc*}}{g_0 \eta (2-\eta)} \left(1 + \frac{8}{5} \eta \varepsilon_s g_0 \right) \left(1 + \frac{8}{5} \eta (3\eta - 2) \varepsilon_s g_0 \right) + \frac{3}{5} \eta \mu_b^{kc} \right]; \alpha = 1.5 \quad (4-17)$$

$$\begin{aligned} \mu_s^{kc*} &= \frac{\rho_s \varepsilon_s g_0 \theta \mu^k}{\rho_s \varepsilon_s g_0 \theta + \left(\frac{2\beta \mu^{kc}}{\rho_s \varepsilon_s} \right)}; \mu^{kc} = \frac{5}{96} \rho_s d_p \sqrt{\pi \theta}; \mu_b^{kc} = \frac{256}{5\pi} \mu^{kc} \varepsilon_s^2 g_0; \eta \\ &= (1 + e)/2 \end{aligned} \quad (4-18)$$

$$\kappa_s = \left(\frac{\kappa_s^*}{g_0}\right) \left[\left(1 + \frac{12}{5}\eta\varepsilon_s g_0\right) \left(1 + \frac{12}{5}\eta^2(4\eta - 3)\varepsilon_s g_0 + \frac{64}{25\pi}(41 - 33\eta)\eta^2(\varepsilon_s g_0)^2\right) \right] \quad (4-19)$$

$$\kappa_s^* = \frac{\rho_s \varepsilon_s g_0 \theta \kappa}{\rho_s \varepsilon_s g_0 \theta + \left(\frac{6\beta\kappa}{5\rho_s \varepsilon_s}\right)}, \kappa = \frac{75\rho_s d_p \sqrt{\pi\theta}}{48\eta(41 - 33\eta)} \quad (4-20)$$

$$J_s = \frac{48}{\sqrt{\pi}}\eta(1 - \eta)\frac{\varepsilon_s g_0}{d_p}\theta^{3/2} \quad (4-21)$$

The above equations, also referred to as granular kinetic theory, have been applied in gas-solid flows successfully over dilute [69, 73] and dense regimes [19, 63, 66, 74], and there is generally good agreement in literature. The radial distribution function at contact (g_0) is expressed using the analytical equation of Carnahan and Starling [75] in the present study.

$$g_0 = \frac{1}{(1 - \varepsilon_s)} + \frac{3\varepsilon_s}{2(1 - \varepsilon_s)^2} + \frac{\varepsilon_s^2}{2(1 - \varepsilon_s)^3} \quad (4-22)$$

The closure for the interaction term, π_θ , will be described in the turbulence interaction term section.

Solid-Phase Frictional Stress

In the emulsion region of flow where solids volume fractions are high, an appropriate description of stress that accounts for the sustained contacts between particles is necessary while describing solid-phase stress. This stress, termed as frictional stress ($\underline{\underline{\sigma}}_s^f$), is typically written in Newtonian form and added to the stress predicted by the granular kinetic theory, which assumes instantaneous collisions.

$$\underline{\underline{\sigma}}_s^f = -p_s^f \underline{\underline{I}} + \mu_s^f \left(\nabla \underline{\underline{u}}_s + \nabla \underline{\underline{u}}_s^T \right) \quad (4-23)$$

$$\underline{\underline{\sigma}}_s = \underline{\underline{\sigma}}_s^{kc} + \underline{\underline{\sigma}}_s^f \quad (4-24)$$

Empirical theories derived from soil mechanics concepts have been traditionally employed to model the frictional pressure (p_s^f) and viscosity (μ_s^f) terms in the above equation. Numerous friction model validation studies [15, 62, 66, 76-78] can be found in literature ranging from simple flows such as bin discharge [66, 76] to more complex bubbling bed flows [77]. Frictional models contain many empirical constants and there is no consensus on the best form of frictional stress yet.

Two commonly used expressions for frictional pressure come from Syamlal *et al.* [51] and Johnson *et al.* [79]. The Syamlal *et al.* [51] expression is a power law function of solids volume fraction that is activated only when the solids volume fraction exceeds the maximum packing limit. Numerous authors have recognized the deficiency of this model which predicts no frictional stress below the packing limit [76, 78]. Therefore, in the present investigation, a widely accepted form of frictional pressure based on Johnson *et al.* [79] is employed and the granular assembly is assumed to deform without any volume change (critical state).

$$p_s^f = \begin{cases} 10^{25}(\varepsilon_s - \varepsilon_s^{max})^{10}, & \varepsilon_s > \varepsilon_s^{max} \\ Fr \frac{(\varepsilon_s - \varepsilon_s^{min})^r}{(\varepsilon_s^{max} - \varepsilon_s)^s}, & \varepsilon_s^{max} \geq \varepsilon_s > \varepsilon_s^{min} \\ 0, & \varepsilon_s \leq \varepsilon_s^{min} \end{cases} \quad (4-25)$$

However, the above expression contains material-dependent empirical constants, Fr , r , s and ε_s^{min} which need to be determined. Following the arguments of Johnson *et al.* [79], the values of $r = 2$, and $s = 5$ are chosen such that frictional pressure increases very rapidly as ε_s approaches ε_s^{max} and $\varepsilon_s^{min} = 0.5$ is chosen so that frictional forces vanish when the solids volume is below 50%. Johnson *et al.* [79] chose the multiplier, Fr , to match the material's random packing fraction and studied flow down an inclined

chute. However, a more appropriate calibration for Fr is necessary for fluidized bed flows, as is attempted in the present investigation.

Frictional viscosity has been traditionally modeled from approaches of Schaeffer [80], Savage [81] and Srivastava and Sundaresan [66]. All the three approaches are largely based on soil mechanics and assume that frictional viscosity is directly proportional to the normal stress or frictional pressure. Savage [81] model assumes that frictional viscosity decreases with increase in fluctuations in the solid strain rate, whereas the Schaeffer model [80] assumes that frictional viscosity decreases with increase in the mean strain rate. The Srivastava and Sundaresan [66] model is an ad-hoc combination of the other two models. Since different authors have employed different approaches successfully, a comparative study with experiment is necessary in order to determine the frictional viscosity model most suitable for the present application.

Turbulence Interaction

The inter-phase interaction terms seen in the granular energy equation and the turbulent kinetic energy equation, π_θ and π_k , represent the energy transfer between the fluctuating velocity components of both phases across the interface. Many authors have proposed various approaches to close these terms [67, 68, 82, 83]. There is fairly good agreement on the fundamental form of the interaction term in the granular energy equation, π_θ .

$$\pi_\theta = \beta \left(\overline{u'_g \cdot u'_s} - \overline{u'_s \cdot u'_s} \right) = \beta (k_{sg} - 3\theta) \quad (4-26)$$

However, there is no consensus on the form of cross-correlation term (k_{sg}) in literature. Different cross-correlation terms have been proposed and tested in specific,

mostly very dilute, flow regimes [71, 82, 84, 85]. In the present investigation, the particle fluctuations are expected to be unaffected by the details of gas fluctuations in the dilute plume region since the Stokes number is very high [37]. Therefore, a form of cross-correlation proposed by Koch and Sangani [85] that has been applied in dense-phase flows by Srivastava and Sundaresan [66] is employed here, to capture any interaction in the dense phase accurately.

$$\beta k_{sg} = \frac{81 \varepsilon_s \mu_g^2 |u_g - u_s|^2}{g_0 d_p^3 \rho_s \sqrt{\pi \theta}} \quad (4-27)$$

The turbulence interaction model description in the turbulent kinetic energy equation (π_k), on the other hand, tends to be more fundamentally diverse [67, 68, 82]. They differ in the mechanism for energy transfer which could be inter-phase drag or wake formation at the edge of particles, both of which could be significant in the high Reynolds number, dilute jet plume region. A general closure model for π_k , suitable for bubbling beds with jet injection, is currently not available and needs to be determined with the help of specific experimental data.

Boundary Conditions

Finally, the boundary conditions for particle velocity and granular temperature at the wall are obtained from the commonly used equations of Johnson and Jackson [86], who derived a semi-empirical partial slip condition arising from collisional momentum loss at the wall. The value for the specularity coefficient (φ), an empirical constant that estimates the degree of roughness at the wall, is chosen as 0.002 following Bolio [68].

$$\underline{n} \cdot \left(\frac{\underline{\sigma}_s^{kc}}{\underline{\underline{\sigma}}_s} + \frac{\underline{\sigma}_s^f}{\underline{\underline{\sigma}}_s} \right) \cdot \frac{\underline{u}_s}{|\underline{u}_s|} + \left(\underline{n} \cdot \frac{\underline{\sigma}_s^f}{\underline{\underline{\sigma}}_s} \cdot \underline{n} \right) \tan \delta_w + \frac{\pi \sqrt{3}}{6 \varepsilon_s^{max}} \varphi \rho_s \varepsilon_s g_0 \sqrt{\theta} |u_s| = 0 \quad (4-28)$$

$$\underline{n} \cdot (\kappa_s \nabla \theta) = \frac{\pi\sqrt{3}}{6\varepsilon_s^{max}} \varphi \rho_s \varepsilon_s g_0 \sqrt{\theta} |\underline{u}_s|^2 - \frac{\pi\sqrt{3}}{4\varepsilon_s^{max}} (1 - e_w^2) \rho_s \varepsilon_s g_0 \theta^{\frac{3}{2}} \quad (4-29)$$

Here \underline{n} is the unit normal to the wall, δ_w the angle of wall friction, ε_s^{max} the maximum packing fraction and e_w the coefficient of restitution between the particle and the wall.

Standard single-phase wall functions are imposed for the gas phase [87]. The wall boundary conditions are not expected to play a major role in bubbling bed flows unlike pneumatic pipe flows which are significantly influenced by pipe walls.

Model Summary

Appropriate closure models for the present gas-solid continuum framework have been carefully selected from currently available models. Most closure relations agree with the default models (Table 4-1) implemented in the US Department of Energy open source code, MFIx (Multiphase Flows for Inter-phase Exchanges). However, the description for three terms, namely, the multiplier in the frictional pressure expression, frictional viscosity model and gas turbulence modulation term, still remain undetermined. The challenge lies in finding an appropriate way to close these terms before the overall continuum model may be validated in predicting the flow details inside the jet plume of a bubbling fluidized bed.

Simulation Setup

The model equations in the continuum framework were solved using MFIx. The details of the numerical technique can be found in Syamlal *et al.* [51]. The maximum residual at convergence was set to 1e-3 for the continuity and momentum equations combined and 1e-4 for the granular energy, turbulent kinetic energy and turbulent dissipation equations respectively. The particle properties, gas properties and boundary

conditions for the simulations were input in agreement with the real experimental system wherever possible (Table 4-2). A detailed description of the experimental setup can found in Mychkovsky [36]. The main difference between the experiment and simulation parameters was in the column height. Experiments with a vertical jet were made in a short column with a wire screen installed at the top which prevented loss of particles. In simulations, the corresponding prevention of loss of solids from the top of the column was achieved by specifying a very tall domain which allowed the solids to fall back down. Though the experiments were conducted in the presence of acrylic bounding walls (pseudo- 2D arrangement), the development of self-similar velocity profiles for both phases inside the jet plume has been consistent with the analytical Gaussian profile for two-dimensional jets [27, 32, 88]. Therefore, the simulations conducted in this investigation were two-dimensional and the governing equations were not solved along the thickness direction.

Two different domains and three different mesh arrangements have been used for simulations conducted in this work. The simulation domains and boundary conditions are shown in Figure 4-2 and the mesh arrangements are described in Table 4-3 and Figure 4-3. At the pipe inlet ($y = -L_p$, $x = 0$ to $D_j/2$) in Figure 4-2b, turbulence values of $k_j = 21 \text{ m}^2/\text{s}^2$ and $\epsilon_j = 2.5\text{e}4 \text{ m}^2/\text{s}^3$ were specified following standard CFD guidelines corresponding to an inflow velocity of $V_j = 92 \text{ m/s}$. For simulations with non-zero fluidization rates, a wall condition was imposed immediately next to the exit of the inlet pipe for a short distance of approximately $0.5D_j$ ($y = 0$, $x = D_j/2$ to D_j) before fluidization inflow conditions were specified. This ensured that there was no conflict in the ghost cell implementation of boundary conditions and also allowed for the inflow velocity and

turbulence values to decay gradually. The sensitivity of this distance on the results was found to be negligible. All simulations were started from a uniform loosely packed bed, $\epsilon_s = 0.5$, at stagnant conditions to speed up initial convergence.

Results and Discussion

The results are divided into four studies that compare simulation results with experimental data (Table 4-4). The first three studies find ways of describing the unclosed terms in the present continuum framework by benchmarking against available experimental data: Study 1 investigates the simple fluidization curve with the aim of independently determining the multiplier, Fr ; Study 2 investigates the dense emulsion behavior in the presence of a jet to identify an appropriate frictional viscosity description; Study 3 investigates the gas turbulence profile inside the jet plume of a spouted bed to determine the most suitable turbulence modulation expression. Finally, the last study validates the predictive capabilities of the final overall continuum model against detailed mean and fluctuating velocity measurements of gas and particles inside the dilute jet plume region of a bubbling fluidized bed. The experimental data used for benchmarking and final validation are obtained from the works of Mychkovsky [36], Mychkovsky and Ceccio [27] and Rangarajan *et al.* [37].

Study 1: Determining Multiplier in Frictional Pressure Expression

Simulation domain 1 and Mesh 1 were employed for this study as described in Figure 4-2a and Table 4-3, respectively. In this study, there is no vertical jet and hence no descriptions for the gas-phase turbulence and gas turbulence interaction were necessary. The default form for frictional viscosity come from Srivastava and Sundaresan [66]. Fluidization velocities ranging from $V_{fl} = 5$ to 50 cm/s were simulated for different values of the multiplier Fr . Each simulation was run for 3 s of real time, after

which the gas pressure drop across the bed (ΔP) reached a steady value. Mesh insensitivity was ensured. The continuum model pressure drop predictions were normalized and compared against experiment.

The sensitivity of the simulation fluidization curve to the multiplier Fr is shown in Figure 4-4. Increasing Fr decreases the slope of the packed bed pressure drop accompanied by an increase in the minimum fluidization velocity prediction. This is because with increase in Fr , higher frictional forces are estimated between particles, resulting in a decrease in the packing fraction thereby decreasing the gas-solid drag. After attempting a range of values for Fr , it was found that $Fr = 0.05$ Pa predicted closest agreement with experiment in terms of both the slope of the packed bed region, and the point where the packed bed and fluidization lines meet in the fluidization curve (Figure 4-4). However, it can be seen that the simulation is unable to capture the bump in the experimental curve close to minimum fluidization, which is expected since the model neglects cohesive effects between particles. To be consistent with the experiment, the minimum fluidization value in the present investigation is chosen to be $V_{mf} = 29$ cm/s, which falls just after the bump. Finally, it was ensured that the description for frictional viscosity did not affect pressure drop predictions by conducting the fluidization simulations using different viscosity models, including artificially imposing zero frictional viscosity (Figure 4-5). This study also shows how fluidization curves can be a robust tool to validate the empirical constants in the frictional pressure expression without the influence of other uncertainties in the continuum framework, such as the form of frictional viscosity or turbulence interaction.

Study 2: Determining Frictional Viscosity Model

The aim of this study is to qualitatively compare the macroscopic flow pattern predicted by the continuum model in the presence of a jet against the experiment and to ensure that the key dense flow dynamics are captured by the frictional model. The simulation domain is shown in Figure 4-2b. A non-uniform mesh (Mesh 2) with more grids close to the jet orifice, where the gradients are expected to be high, was chosen for the study (Table 4-3). The turbulence interaction term is not expected to influence the qualitative dense phase behavior and was assumed to be zero in the continuum model adopted in this section. From the results of Study 1, the multiplier Fr was chosen to be 0.05 Pa. Fluidization velocities of $V_{fl} = 0$, V_{mf} and $1.5V_{mf}$ were simulated for a period of 15 s of real time, and the macroscopic concentration predictions were compared with digital videos taken from experiment. Frictional viscosity description in the continuum model was changed between that of Srivastava and Sundaresan (Eq. 4-30), and Savage (Eq. 4-31), as implemented in MFIX.

$$\mu_s^f = \frac{p_s^f \sin \delta}{\sqrt{2}} \frac{1}{\sqrt{\frac{S_s}{S_s} : \frac{S_s}{S_s} + \theta/d_p^2}} \quad (4-30)$$

$$\mu_s^f = \frac{p_s^f \sin \delta}{\sqrt{2}} \sqrt{\frac{\mu_s^{kc}}{J_s \varepsilon_s \rho_s}} \quad (4-31)$$

Figure 4-6 to Figure 4-8 show the dynamic flow behavior for the experiment and each of the frictional viscosity models with increasing fluidization velocity, at intervals of approximately 1 s real time. While the absolute time does not matter, a generous period of 5 s was given for the simulations from the start to avoid any effects of initial conditions. It is seen that in the experiment, the spouted bed case, $V_{fl} = 0$, shows a generally steady behavior with a stable plume boundary formation. Upon increasing the

fluidization velocity to V_{mf} , the plume boundary shows instability as it interacts with the fluidized emulsion region. Small, sparse bubbles can be seen in the emulsion region. At a still higher fluidization velocity of $V_{fl} = 1.5V_{mf}$, the plume boundary displays high instability as large bubbles move toward and interact with the jet plume from the emulsion region (Figure 4-6). Similar qualitative behavior is captured by the Savage frictional viscosity expression, Eq. 4-31 (Figure 4-7). On the other hand, corresponding predictions from Srivastava and Sundaresan form of frictional viscosity (Eq. 4-30), show unstable behavior at $V_{fl} = 0$, a stable plume boundary at a fluidization rate of V_{mf} and large bubbles in the emulsion that tend to move in distinct vertical channels away from the jet axis at fluidization rates of $V_{fl} = V_{mf}$ and $1.5V_{mf}$ (Figure 4-8). The poor performance of the Srivastava and Sundaresan model (Eq. 4-30) in predicting the macroscopic flow pattern is estimated to be because this model tends to predict low frictional viscosity that makes the solid phase too liquid-like (Figure 4-9).

Finally the fluidization case of $V_{fl} = V_{mf}$ was simulated with Schaeffer viscosity model (Eq. 4-32) and was found to behave the same way as Srivastava and Sundaresan (Eq. 4-30), form suggesting that the mean strain rate dominates in predicting frictional viscosity in Eq. 4-30.

$$\mu_s^f = \frac{p_s^f \sin \delta}{\sqrt{2}} \frac{1}{\sqrt{\underline{\underline{S_s}} : \underline{\underline{S_s}}}} \quad (4-32)$$

Due to better match with macroscopic dynamics of the experiment, the Savage frictional viscosity expression (Eq. 4-31) is employed in the present overall continuum model.

Study 3: Determining Turbulence Modulation Term

Since the continuum model predicts turbulent kinetic energy and granular kinetic energy, whereas the experimental measurements provide fluctuating velocities only in the streamwise direction, anisotropies in the gas phase and particle phase have to be assumed before fluctuating velocity comparisons can be made. In the present investigation, the anisotropy in the gas-phase turbulence is assumed to be the same as that of a single-phase planar turbulent jet [34]. On the other hand, the granular temperature is assumed to be isotropic based on the work of Jones [89] who found that dilute flows of relatively large particles can be characterized by isotropic particle fluctuations. These assumptions simplify to,

$$v'_g = \sqrt{\frac{k}{1.088}} \quad (4-33)$$

$$v'_s = \sqrt{\theta} \quad (4-34)$$

A spouted bed simulation ($V_{fl} = 0$) was conducted and the gas fluctuating velocity profile at a height $y = 100$ mm was matched with corresponding experimental data inside the jet plume. The frictional pressure multiplier and the closure for frictional viscosity were obtained from the findings of Study 1 and Study 2 respectively. Mesh 3 (Table 4-3), which is a mesh arrangement similar to Study 2, but with double the mesh density was employed after ensuring mesh insensitivity of the results. The mesh insensitivity and the fact that fluctuations were not induced upon increasing grid resolution also ensured that there was no ill-posedness [90] due to the existence of a dense solid-gas interface at the plume boundary. The simulation required 2 s of real time to predict a steady profile. To determine the significant mechanisms for the

enhancement or dampening of gas turbulence due to particles, three forms of gas turbulence modulation term were considered.

$$\pi_k = 0 \quad (4-35)$$

$$\pi_k = \pi_k^{drag} \quad (4-36)$$

$$\pi_k = \pi_k^{drag} + \pi_k^{wake} \quad (4-37)$$

The first form (Eq. 4-35) assumes that there is no influence of particle fluctuations on gas turbulence, the second (Eq. 4-36) assumes that any enhancement or dampening of gas turbulence is only through instantaneous fluctuations in drag, while the third form (Eq. 4-37) includes the turbulence enhancement due to the formation of particle wakes in addition to drag. A widely accepted general expression [16], with cross-correlation function consistent with the interaction term in the granular energy equation, is specified for the drag contribution (Eq. 4-38). The wake contribution description, on the other hand, tends to be mostly ad-hoc in literature and a slightly modified form of Lun [91], which results in turbulence enhancement at high particle Reynolds numbers ($Re_p > 1000$) is employed in this study (Eq. 4-39).

$$\pi_k^{drag} = \beta \left(k_{sg} - \overline{u'_g \cdot u'_g} \right) = \frac{81 \varepsilon_s \mu_g^2 \left| \underline{u_g} - \underline{u_s} \right|^2}{g_0 d_p^3 \rho_s \sqrt{\pi \theta}} - 2\beta k \quad (4-38)$$

$$\pi_k^{wake} = 12 \frac{C_w \mu_t k}{d_p^2}; \mu_t = 0.029 Re_p \mu_g; Re_p = \frac{\rho_g d_p \left| \underline{u_g} - \underline{u_s} \right|}{\mu_g} \quad (4-39)$$

$$C_w = \begin{cases} 0, & Re_p < 1000 \\ 2, & Re_p \geq 1000 \end{cases}$$

From Figure 4-10 it is seen that when the effect of particles on gas turbulence is ignored, abnormally high values of turbulence are predicted in the dense regions.

Including the effect of instantaneous particle drag on turbulence is able to avoid this unphysical behavior but under-predicts the centerline turbulence suggesting that there is turbulence enhancement due to wake formation as one would expect for the relatively large 838 micron particles [92]. Finally, the form of interaction term that includes both the effect of instantaneous particle drag and the enhancement due to particle wakes is able to avoid the unrealistically high turbulence in the dense regions and captures the turbulence near the centerline accurately. Because of the realistic turbulence prediction and good match with experiment, the gas turbulence interaction model expressed in Eq. 4-37 to Eq. 4-39 is employed in the final continuum framework.

Study 4: Validation of the Final Continuum Model

Before comparing detailed velocity profiles predicted by the two-phase model against experimental data, a single phase validation was carried out. Figure 4-11 shows excellent match between simulation and experiment in both mean and fluctuating velocity at heights $y = 70, 100$ and 130 mm. This match validates that the inlet conditions in the experiment are accurately captured in simulations and also confirms that there is no significant shortcoming in neglecting the bounding walls with regard to the single-phase case [93].

Finally two-phase simulations with the same fine mesh employed in Study 3 were conducted for $V_{fl} = 0, 0.7V_{mf}, V_{mf}, 1.3V_{mf}$ and $1.5V_{mf}$. The closure for the frictional pressure multiplier, frictional viscosity expression and turbulence modulation term come from Study 1, Study 2 and Study 3 respectively (Table 4-4). As seen in the earlier studies, while the spouted bed case, $V_{fl} = 0$ predicts steady profiles after 2 s of real time, the higher fluidization rates do not reach a steady state because of the dynamic emulsion phase. Therefore, these simulations were run for a long time, after which the

time average of four quantities - the mean velocity, standard deviation in the mean velocity, turbulent kinetic energy and granular temperature - reached steady values in the region where experimental measurements were made. The time average for these quantities was calculated from $t = 1$ to $t = 30$ s at intervals of 0.1 s. In order to account for the contribution of unsteadiness in the mean velocities to the gas and particle fluctuations as measured in the experiment, the standard deviation with time in the mean streamwise velocities ($v'_{g,mean}$, $v'_{s,mean}$) were added to the corresponding gas turbulence and granular temperature contributions. The role of such a contribution to velocity fluctuations arising from the large-scale motion induced by the bubbling emulsion phase has been noted in the experiments at high fluidization rates [37].

$$v'_{g,total} = v'_g + v'_{g,mean} \quad (4-40)$$

$$v'_{s,total} = v'_s + v'_{s,mean} \quad (4-41)$$

Figure 4-12 to Figure 4-16 show results of the continuum model simulations for the gas and particle mean and fluctuating velocity at heights $y = 70, 100$ and 130 mm. It must be noted that the unsteady mean velocity contribution can be a significant portion of the total fluctuations at higher fluidization cases as summarized in Table 4-5. In general, there is good match between the mean velocity of the simulation and the experiment for both phases with regard to the mean velocity and fluctuations. Deviations from experiment in the predicted centerline gas velocity at $y = 70$ mm for $V_{fl} = 0.7V_{mf}$ and V_{mf} , and the predicted profile spread at $V_{fl} = 0, 0.7V_{mf}$ and $1.5V_{mf}$ can be noted. The shape of the gas fluctuation profiles show deviation at high fluidization rates. To visualize the performance of the continuum model in capturing the bulk flow features associated with increasing fluidization velocity as observed in the experiment i.e. the

velocity half-width ($x_{1/2}$), centerline mean streamwise velocity and centerline streamwise fluctuating velocity are plotted against the level of fluidization at a height $y = 100$ mm (Figure 4-17 to Figure 4-19). The velocity half-width for each phase is defined as the distance in the x direction where the velocity is half the centerline velocity at the given height y . It can be seen that the simulation is able to predict most of the qualitative behavior seen in the experiment. The centerline gas velocity decreases from single-phase to spouted bed, after which both the gas and particle centerline velocities tend to stay the same with increase in fluidization velocity (Figure 4-18). There is a decrease in gas turbulence from single-phase to spouted bed case and an increasing trend in both gas and particle fluctuations with increasing fluidization velocity (Figure 4-19). The main deviation in the qualitative behavior with respect to the fluidization ratio is seen in the model predictions of velocity half-widths for gas and particles. The simulation is not able to capture the increase in gas and particle velocity half-widths with increase in fluidization rate as observed in the experiment (Figure 4-17).

In such a complicated system it is difficult to quantitatively estimate the reason for any mismatches between experiments and model predictions. Experimental repeatability tests estimate uncertainty in the measurements to be less than 15 % [37]. It is likely that the deviation in centerline velocities at a low height of $y = 70$ mm is because of some difference caused by the round pipe in the experiment which has been neglected in the simulation. The electrostatic effects between the bounding walls and particles responsible for the inward sloping top surface at $V_{fl} = 0$, (Figure 4-12), might be causing the sharper velocity profile decay observed in experiment. Since the dynamic instabilities in mean quantities play a significant role in the fluctuating velocity at high

fluidization rates (Table 4-5), it is possible that the deviation in the shape of gas fluctuations is because the sources of fluctuations in the experiment, which are physical, are not precisely captured by the simulation, in which the sources of fluctuations are numerical. The addition of standard deviation in mean velocity to intrinsic turbulence is not entirely warranted, but a more rigorous approach would require deterministic turbulence models which would be computationally very expensive. The narrower spread in the velocity profiles at high fluidization rates obtained in simulation could be because of an insufficient description of the empirically based closure model for frictional stress.

Summary

A turbulent, frictional continuum model has been validated against two-phase mean and fluctuating velocity experimental data inside the jet plume region of a bubbling fluidized bed with a high-speed vertical jet injection. The descriptions for closure were selected from well-established relations wherever possible, and the main uncertainties were identified and determined by benchmarking against specific experimental measurements. In general, the continuum model shows good agreement with the two-phase mean and fluctuating velocities and is able to predict the experimental trends with increasing fluidization velocity reasonably well. Main discrepancies between model prediction and experiment are noted in the spread of velocity profiles and the shape of gas fluctuation profiles at high fluidization rates. Possible reasons for the mismatch are discussed.

In Chapter 4, it has been shown that if the closure relations are appropriately described the continuum model is capable of predicting the turbulent two-phase flow that occurs in bubbling beds with jet injection. In Chapter 5, this continuum model is

applied in a real industry scenario to probe the effect of operating parameters. Due to the lack of experimental data for comparison, the uncertain closure models are chosen in agreement with Chapter 4.

Table 4-1. Comparison of closure models between MFIX and present study.

Closure	Term	MFIX default	Present study
Drag	Drag coefficient	Syamlal <i>et al.</i> [51]	Wen & Yu [65]
Solid-phase kinetic and collisional stress	Pressure, viscosity and granular conductivity	Agrawal <i>et al.</i> [73]	Same
	Collisional dissipation	Lun <i>et al.</i> [72]	Same
	Radial distribution function	Carnahan & Starling [75]	Same
Solid-phase frictional stress	Frictional Pressure	Syamlal <i>et al.</i> [51]	Johnson <i>et al.</i> [79] ($r = 2$, $s = 5$ and $\epsilon_s^{min} = 0.5$) Fr TBD
	Frictional viscosity	Schaeffer <i>et al.</i> [80]	TBD
Gas-phase stress	Turbulent viscosity	Standard k-epsilon	Same
Gas-particle turbulence interaction	Gas turbulence modulation	0	TBD
	Granular temperature modulation	Agrawal <i>et al.</i> [73]	Same

Table 4-2. System parameters.

Parameter	Description	Experiment [37]	Present study
d_p	Particle diameter	838 μm	Same
ρ_s	Particle density	900 kg/m^3	Same
e	Particle-particle coefficient of restitution	-	0.9
e_w	Particle-wall coefficient of restitution	-	0.5
ϵ_s^{max}	Maximum packing fraction	-	0.65
δ	Angle of internal friction	-	27 deg
δ_w	Angle of wall friction	-	13 deg
H_b	Bed height at maximum packing	38 cm	Same
T	Gas temperature	-	298 K
MW	Gas molecular weight	29 (air)	Same
μ_g	Gas viscosity	-	1.8e-5 kg/(ms)
L	Column width	0.457 m	Same
H	Column height	1 m	4.35 m
W	Column thickness	12.7 mm	Neglected
V_j	Vertical jet inlet velocity	92 m/s	Same
D_j	Vertical jet diameter	9.2 mm	Same
L_p	Inlet pipe length	35 cm	Same
V_{fl}	Fluidization velocity	0, 20.3, 29, 37.7, 43.5 cm/s	Same

Table 4-3. Details of the meshes employed. Arrangement shows “(number of cells) size of each cell”.

Mesh Name	Mesh arrangement	
	Along X direction from centerline	Along Y direction from bottom
Mesh 1	(50)9.14e-3 m	(50)1e-2 m, (10)5e-2 m
Mesh 2	(15)1.33e-3 m, (25)3.48e-3 m, (20)1.22e-2 m	(15)2e-2 m, (40)5e-3 m, (60)1.33e-2 m, (55)1e-2 m
Mesh 3	(30)6.67e-4 m, (50)1.74e-3 m, (40)6.08e-3 m	(15)2e-2 m, (80)2.5e-3 m, (120)6.67e-3 m, (110)5e-3 m

Table 4-4. Closure for the undetermined terms in each study.

Study	Flow simulated	Property investigated	Uncertainties in closure		
			Fr	μ_s^f	π_k
1	Fluidization	Pressure drop across the bed	Varied	Does not play a role	-
2	Jet injection into a fluidized bed	Dynamic emulsion behavior	0.05 Pa	Varied	Does not play a role
3	Spouted bed	Gas turbulence profile inside the jet plume	0.05 Pa	Savage [81]	Varied
4	Jet injection into a fluidized bed	Mean and fluctuating velocity profiles inside the jet plume	0.05 Pa	Savage [81]	$\pi_k^{drag} + \pi_k^{wake}$

Table 4-5. Contribution of unsteady mean velocity to the total fluctuations along the centerline at $y = 100$ mm.

V_{fl}/V_{mf}	$v'_{mean}/v'_{total} * 100$	
	Gas	Solid
0.7	29	21
1.0	42	24
1.3	53	35
1.5	47	23

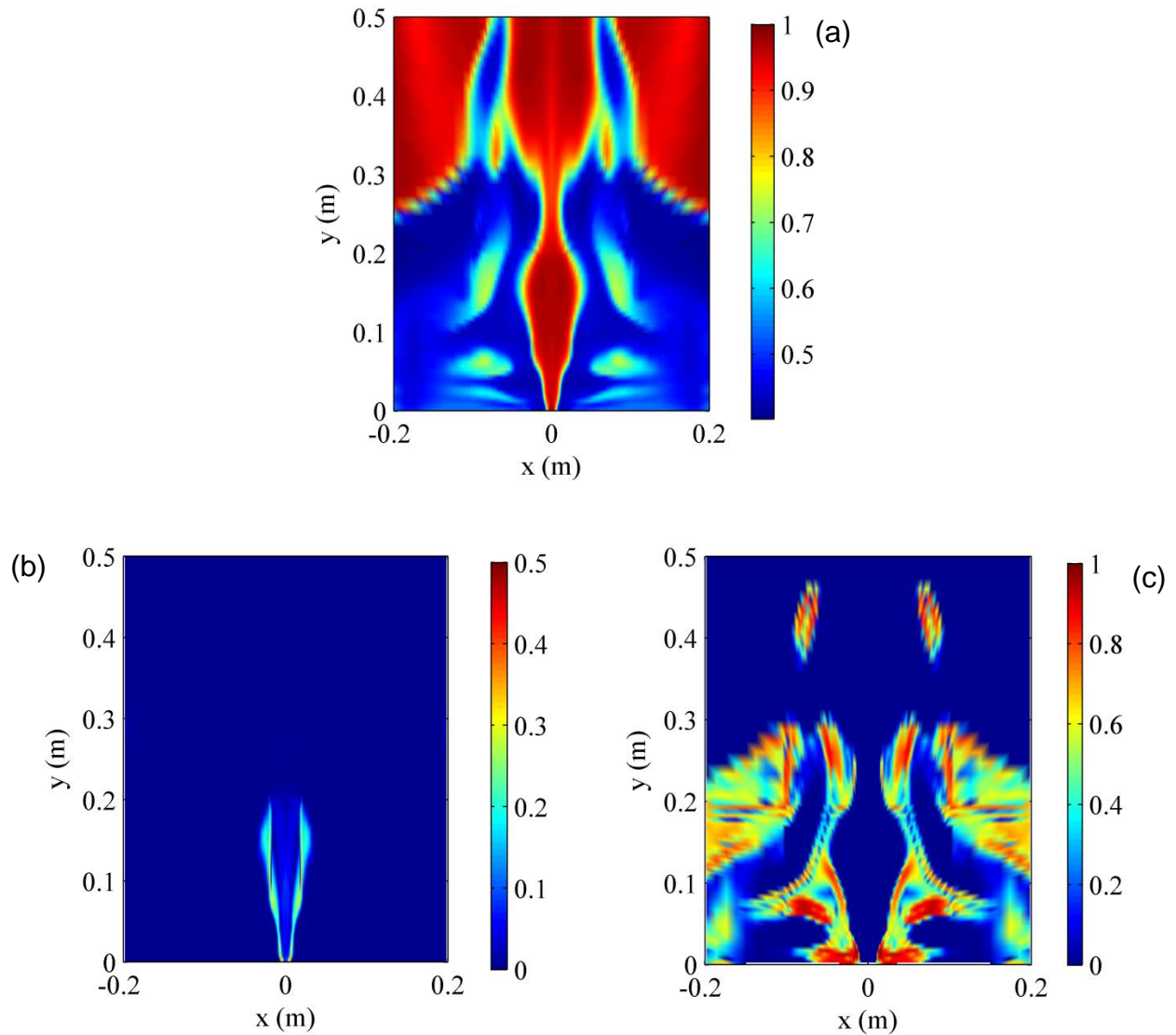


Figure 4-1. The significance of turbulent and frictional, stresses relative to drag, in a bubbling fluidized bed with a jet injection. The simulation conditions are for $V_j = 92$ m/s and $V_{fl} = 1.5V_{mf}$. The continuum model employed is the same as the final model developed in this chapter. (a) Gas volume fraction, (b) Turbulent stress/(Turbulent stress + Drag), (c) Frictional stress/(Frictional stress + Drag).

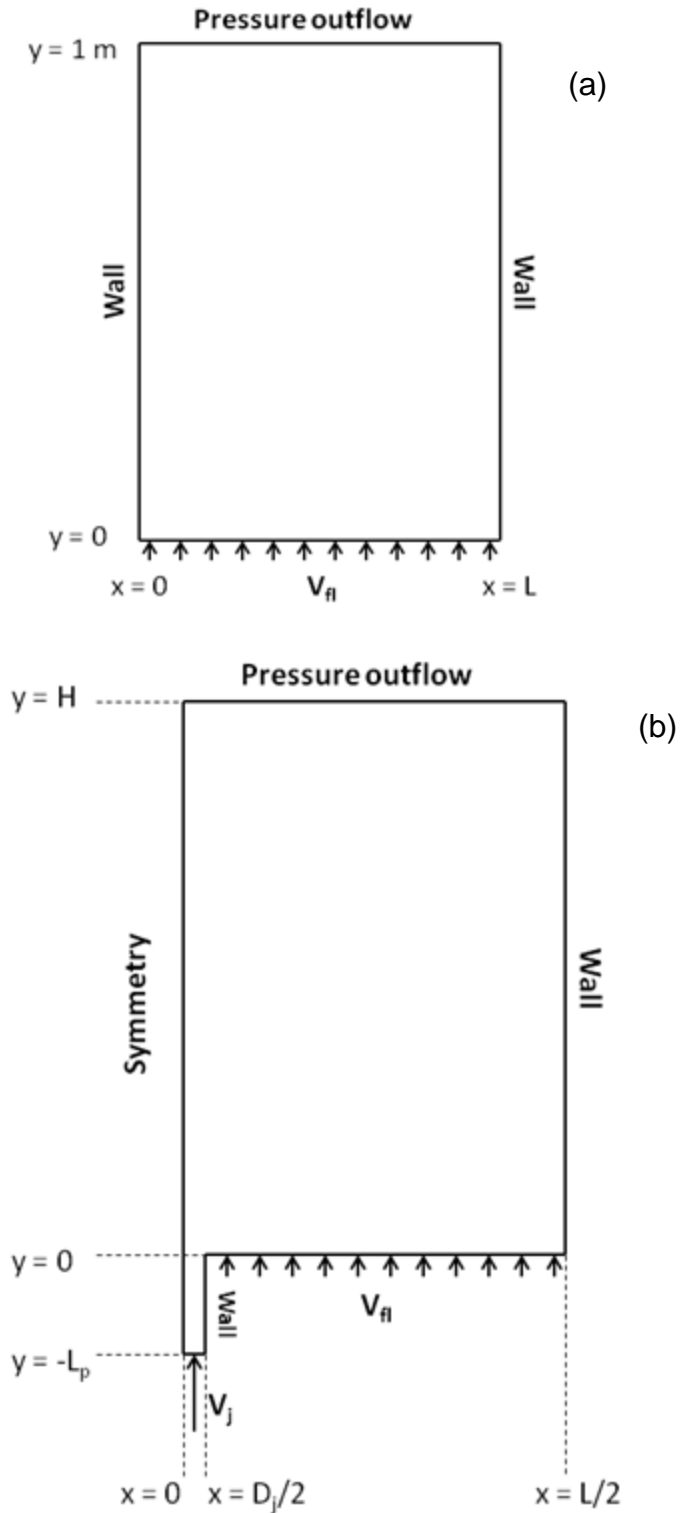


Figure 4-2. Simulation domain and boundary conditions employed. (a) Domain 1. (b). Domain 2. For the case $V_{fl} = 0$, wall boundary conditions were imposed at the bottom distributor plate ($y = 0, D_j/2 < x < L/2$).

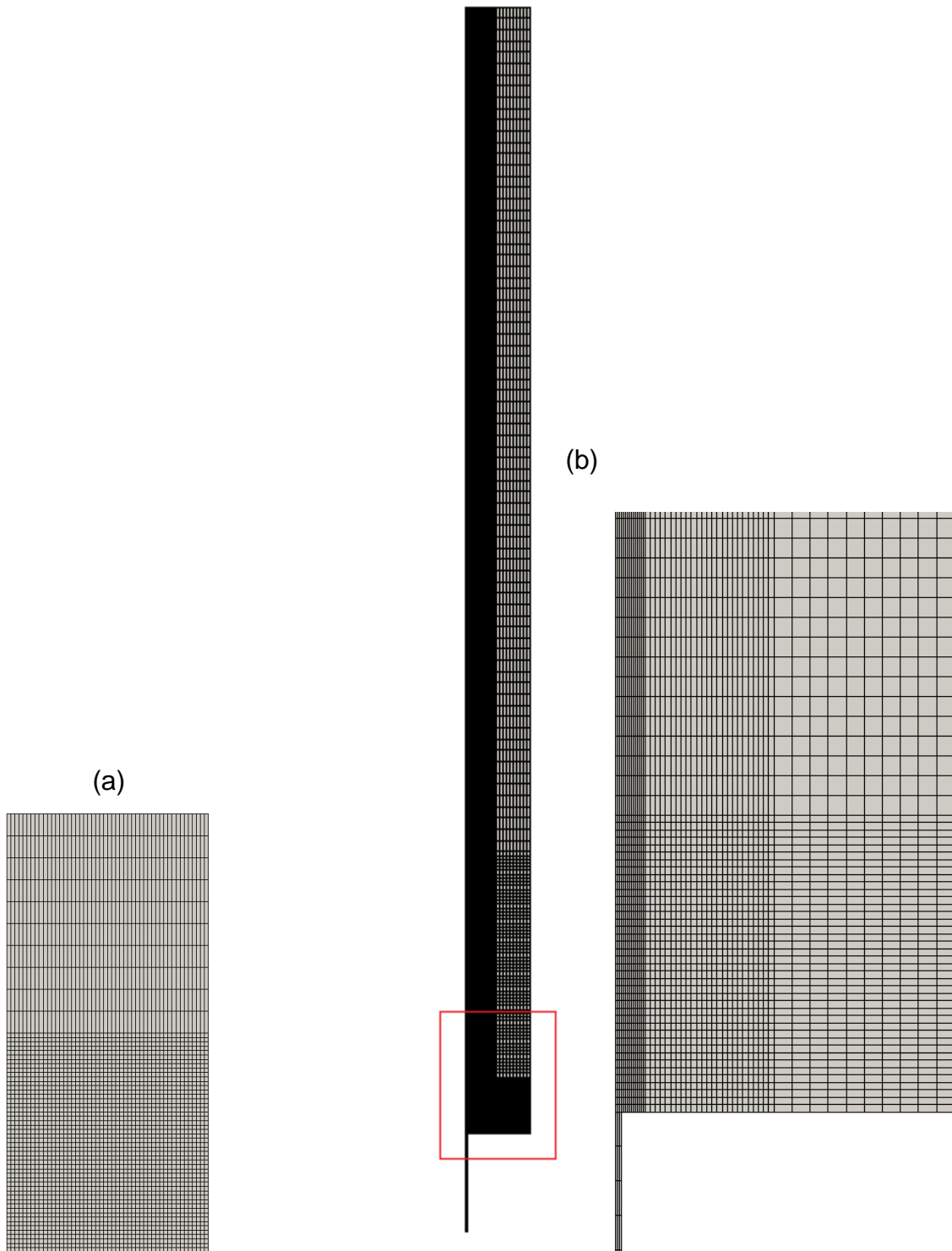


Figure 4-3. Illustration of mesh arrangement. (a) Mesh 1. (b) Mesh 2.

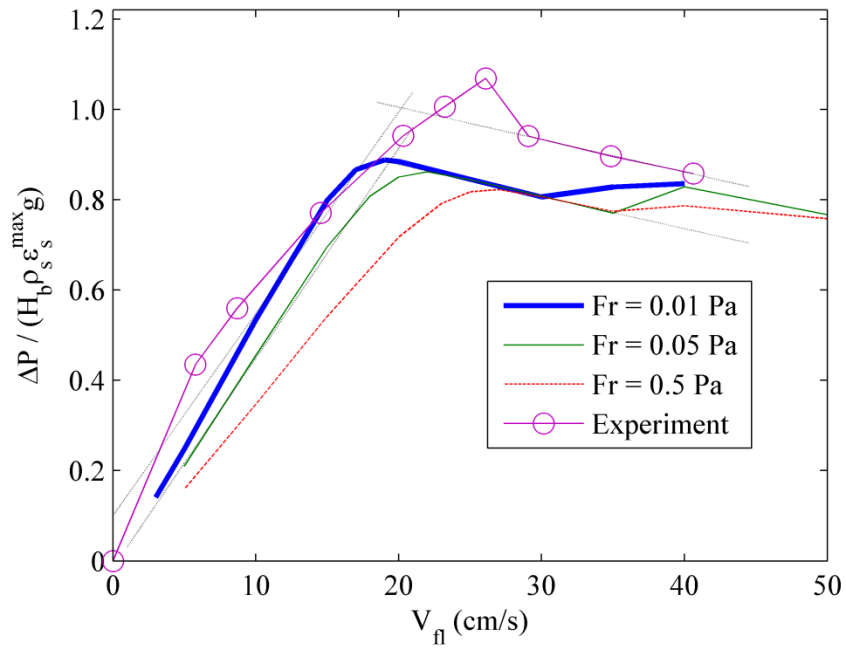


Figure 4-4. Sensitivity of the fluidization curve to frictional pressure multiplier and final match with experiment.

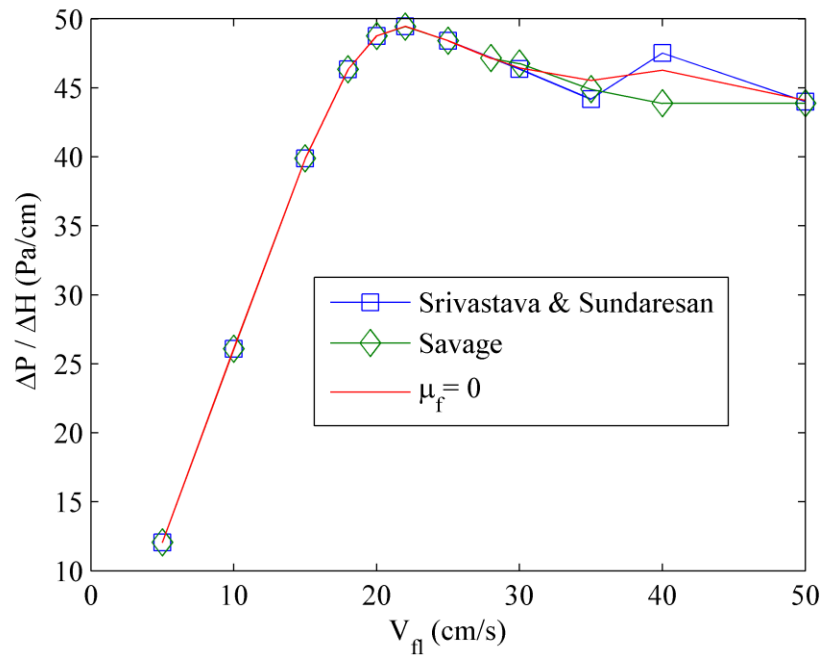


Figure 4-5. Effect of frictional viscosity expression in predicting the fluidization curve. $Fr = 0.05$ Pa.

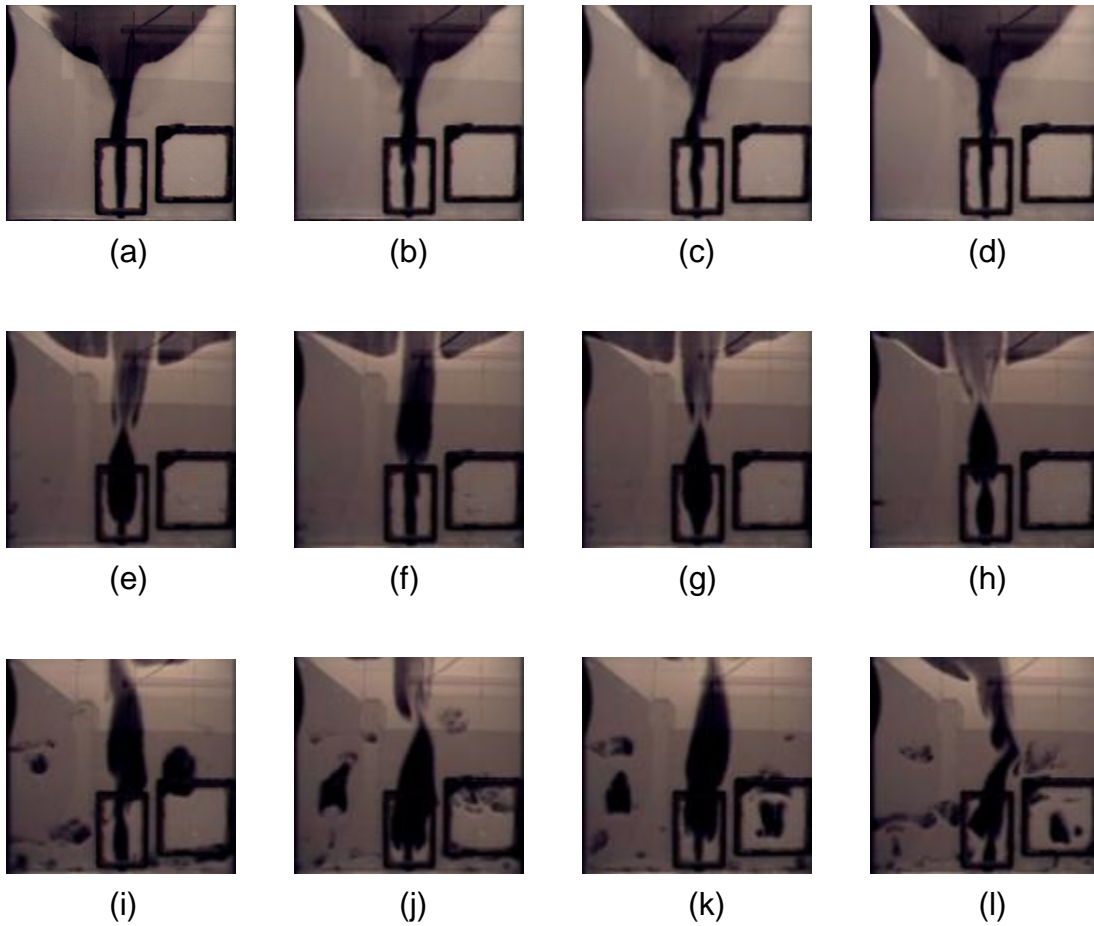


Figure 4-6. Photographs of the experiment at increasing intervals of 1 s. The black portion represents voids and the white portion represents bed particles. (a - d) $V_{fl} = 0$, (e - h) $V_{fl} = V_{mf}$, and (i - l) $V_{fl} = 1.5V_{mf}$.

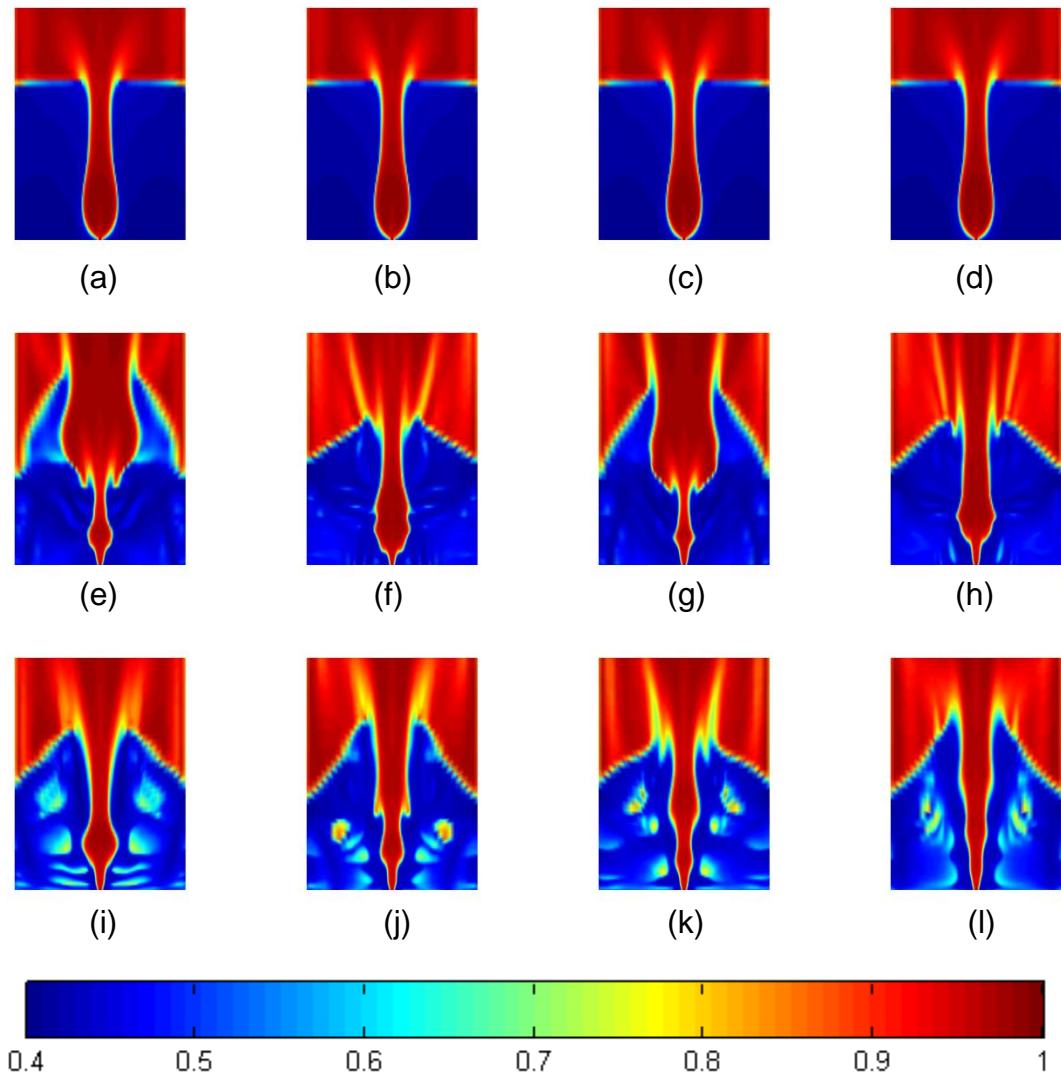


Figure 4-7. Gas volume fraction prediction of Savage frictional viscosity. (a - d) $V_{fl} = 0$ at $t = 5, 5.5, 6$ and 6.5 s. (e - h) $V_{fl} = V_{mf}$ at $t = 5, 6, 7, 8$ s. (i - l) $V_{fl} = 1.5V_{mf}$ at $t = 5, 6, 7, 8$ s.

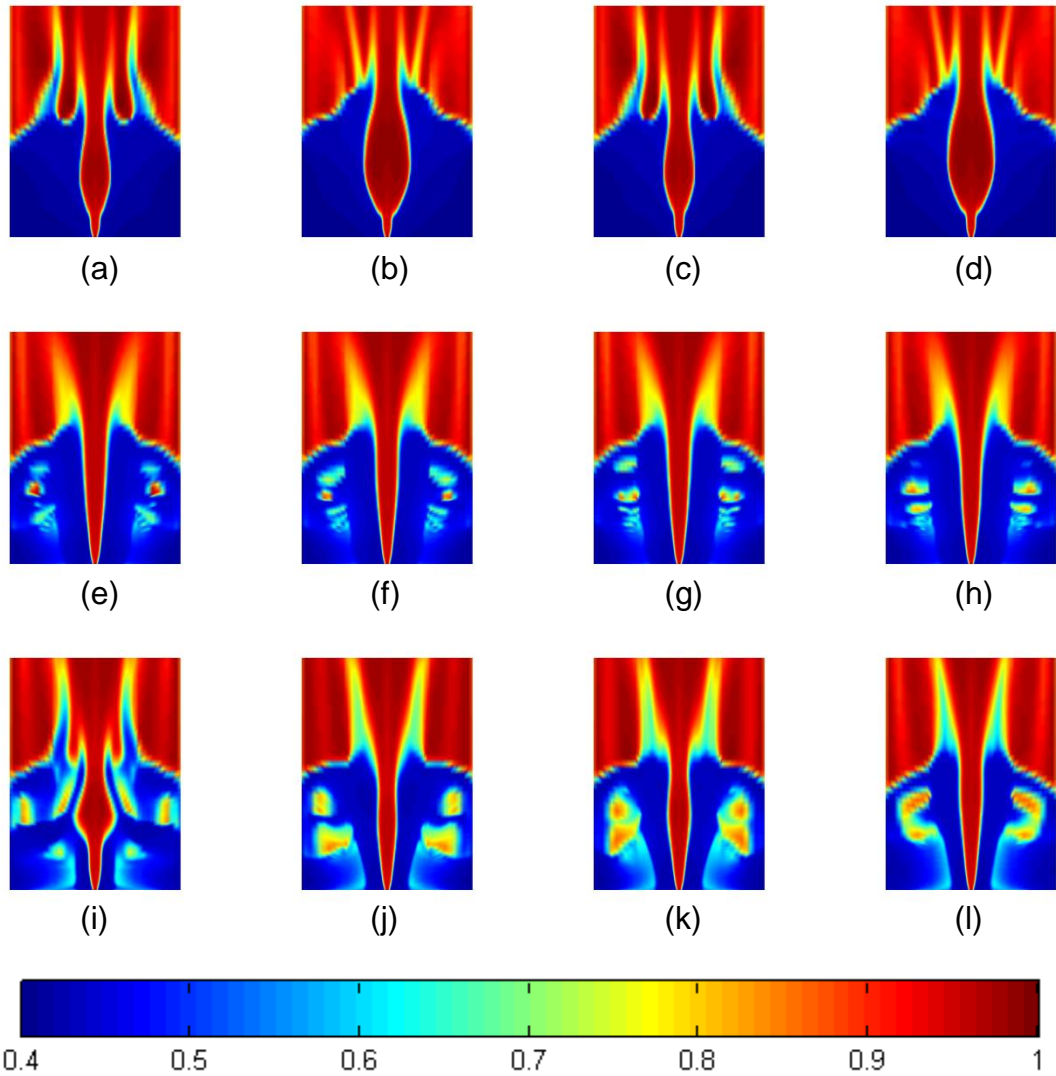


Figure 4-8. Gas volume fraction prediction of Srivastava and Sundaresan frictional viscosity. (a - d) $V_{fl} = 0$ at $t = 5, 5.5, 6$ and 6.5 s. (e - h) $V_{fl} = V_{mf}$ at $t = 5, 6, 7, 8$ s. (i - l) $V_{fl} = 1.5V_{mf}$ at $t = 5, 6, 7, 8$ s.

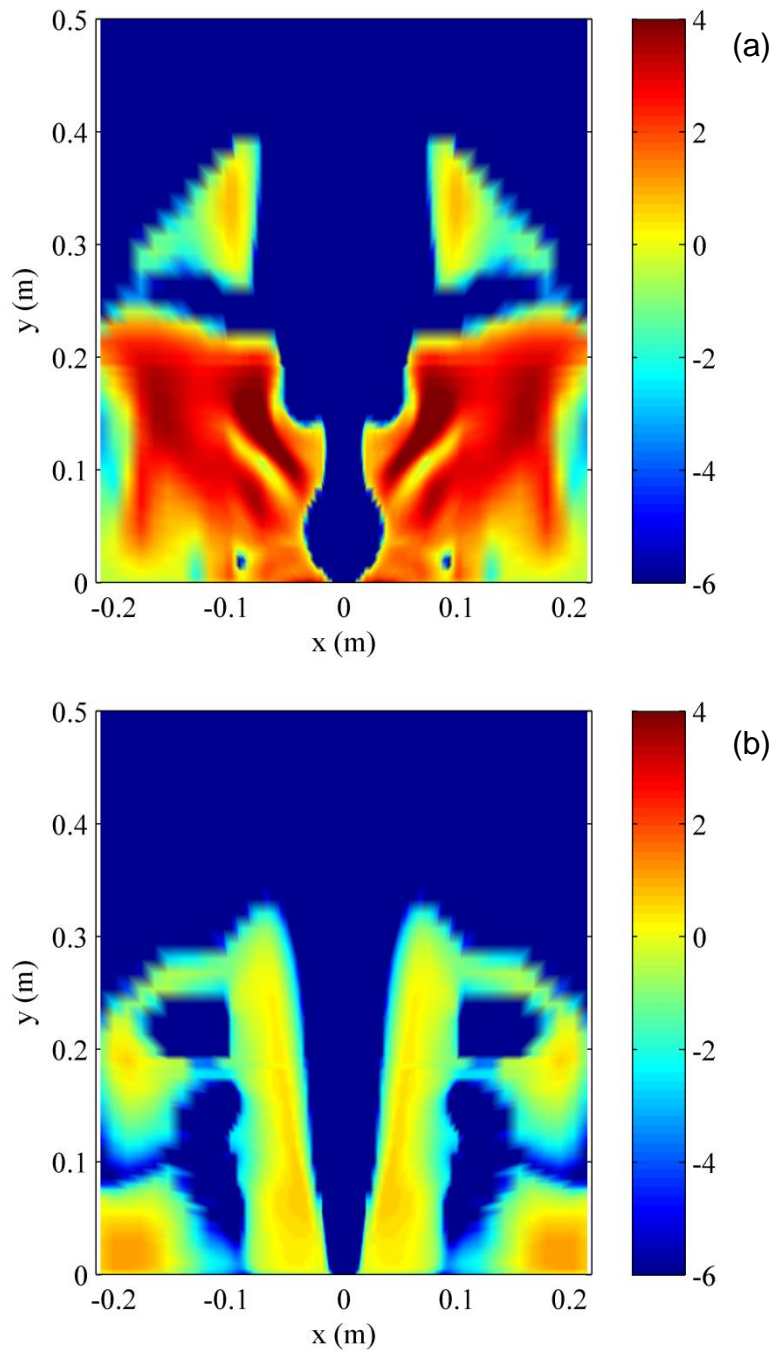


Figure 4-9. Frictional viscosity values on a log scale for $V_{fl} = V_{mf}$ at $t = 15$ s. (a) Predictions by Savage, and (b) Predictions by Srivastava and Sundaresan.

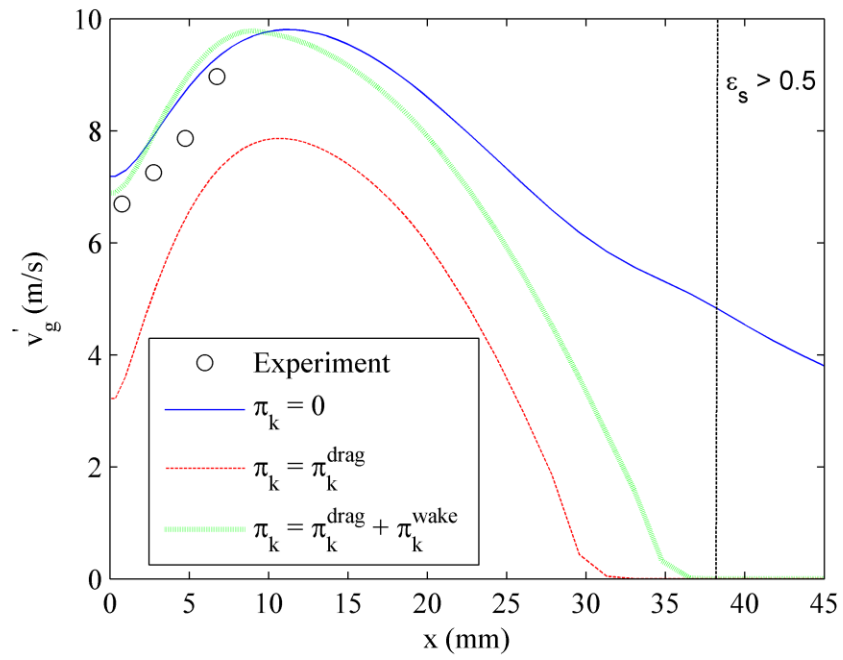


Figure 4-10. Influence of gas turbulence modulation term on the gas fluctuating velocity at $y = 100$ mm for $V_{fl} = 0$.

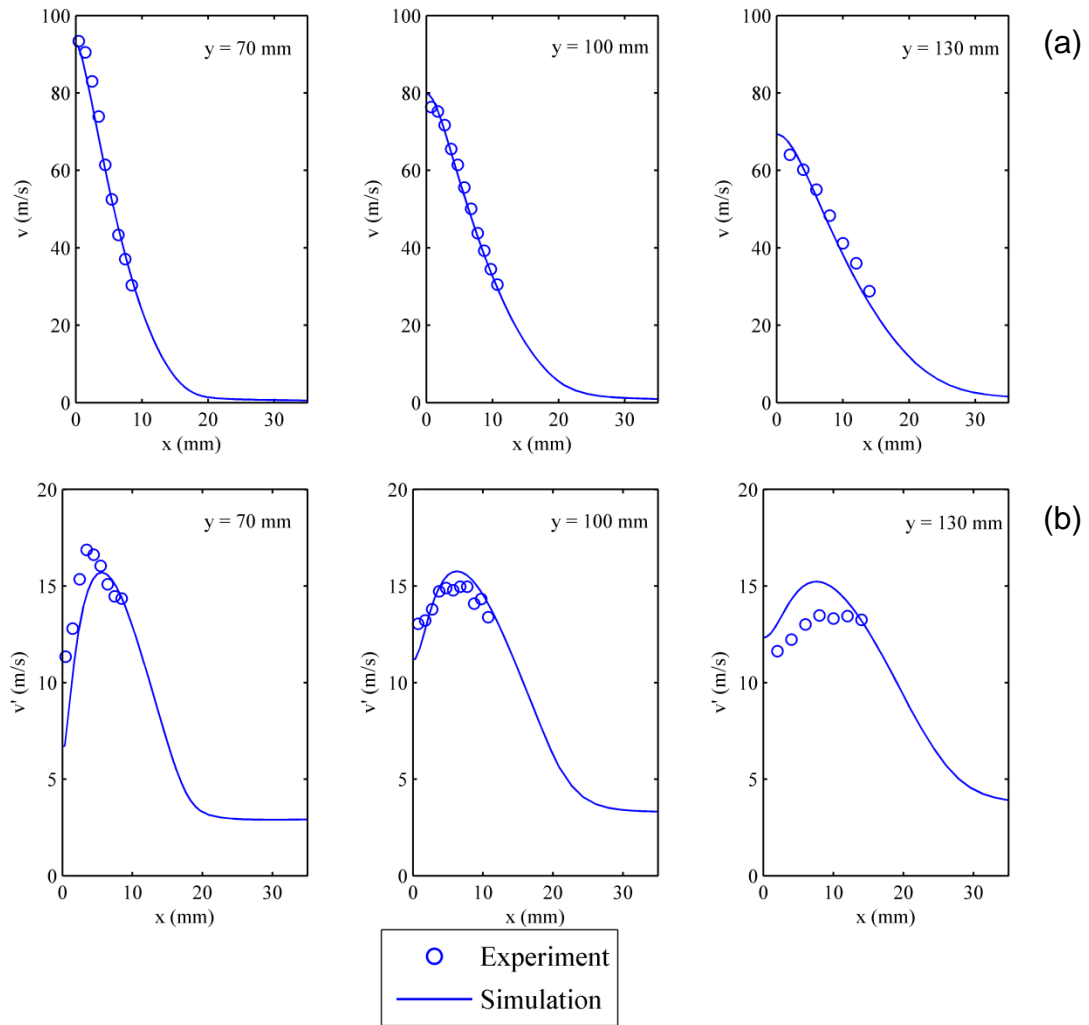


Figure 4-11. Streamwise velocity profiles for single phase jet. (a) Mean velocity, and (b) Fluctuating velocity.

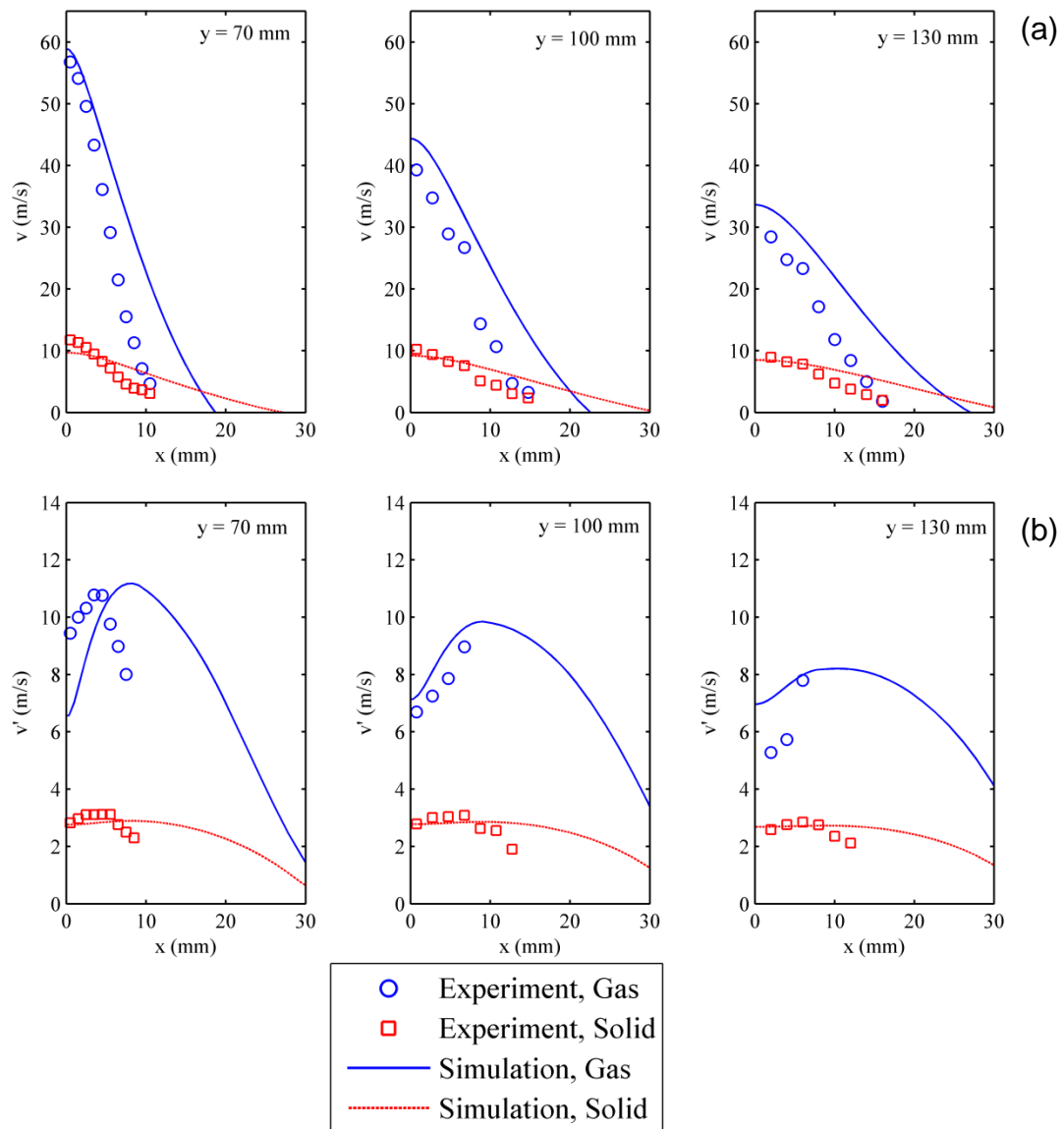


Figure 4-12. Streamwise velocity profiles for $V_{fi} = 0$. (a) Mean velocity, and (b) Fluctuating velocity.

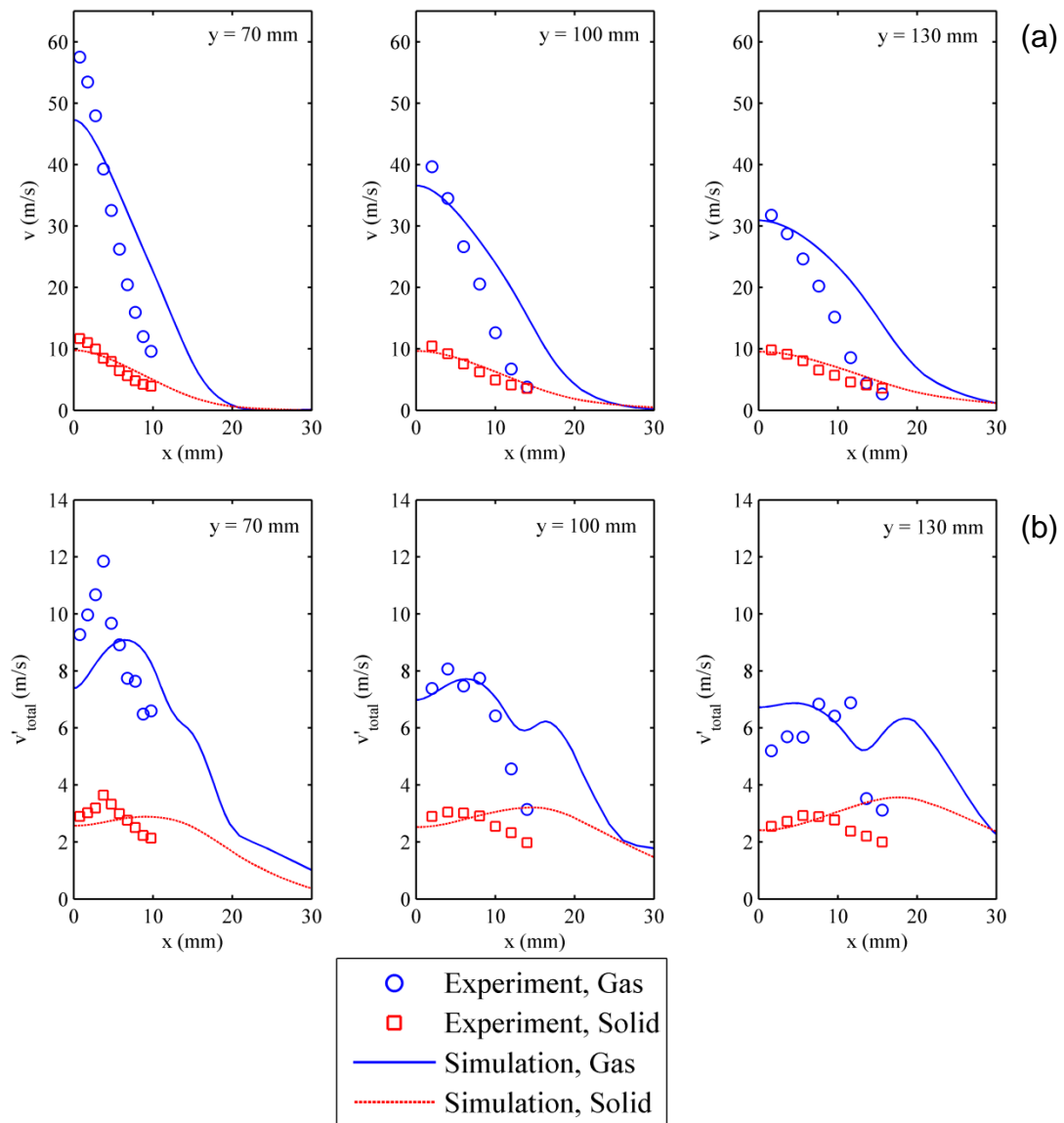


Figure 4-13. Streamwise velocity profiles for $V_{fl} = 0.7 V_{mf}$. (a) Mean velocity, and (b) Fluctuating velocity.

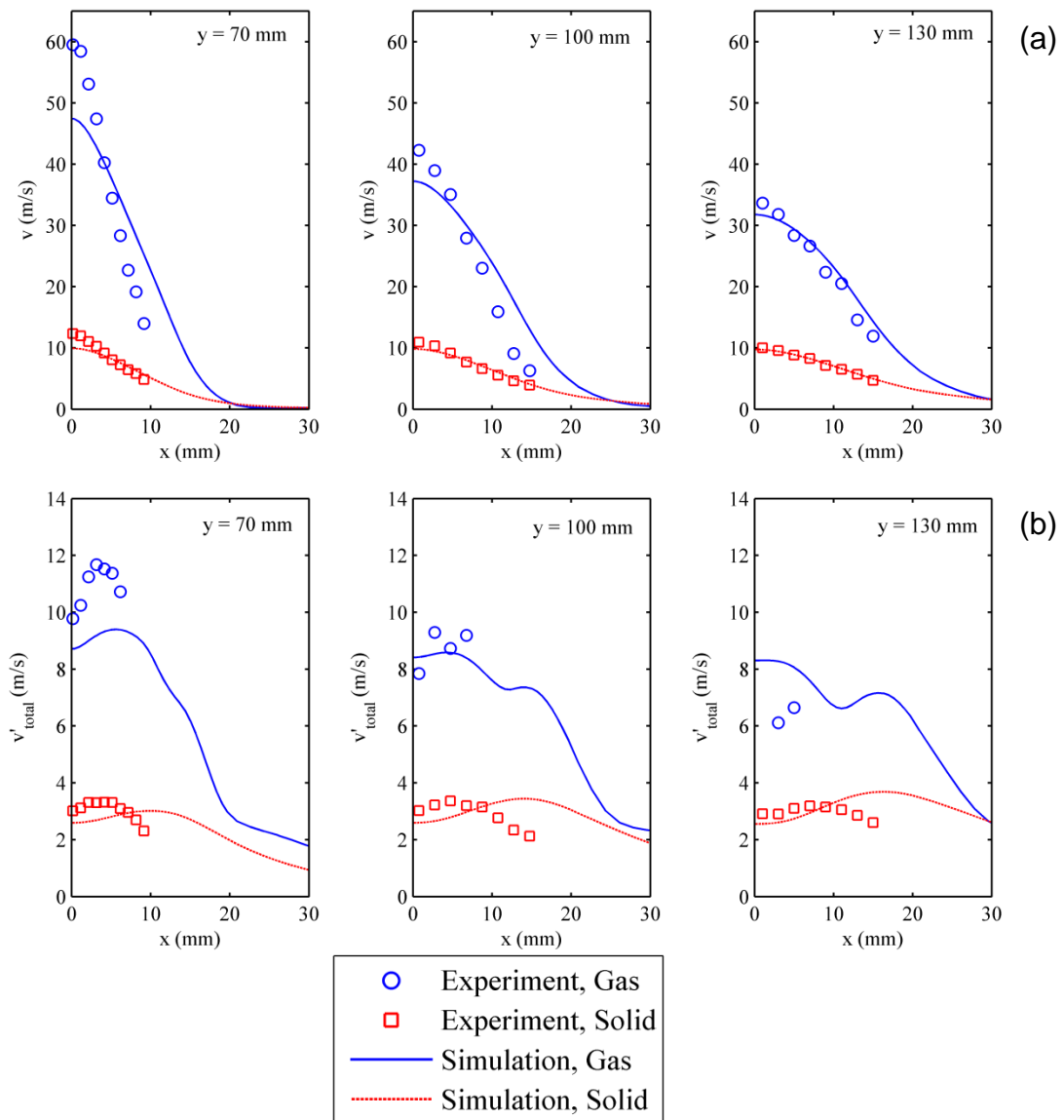


Figure 4-14. Streamwise velocity profiles for $V_{fl} = V_{mf}$. (a) Mean velocity, and (b) Fluctuating velocity.

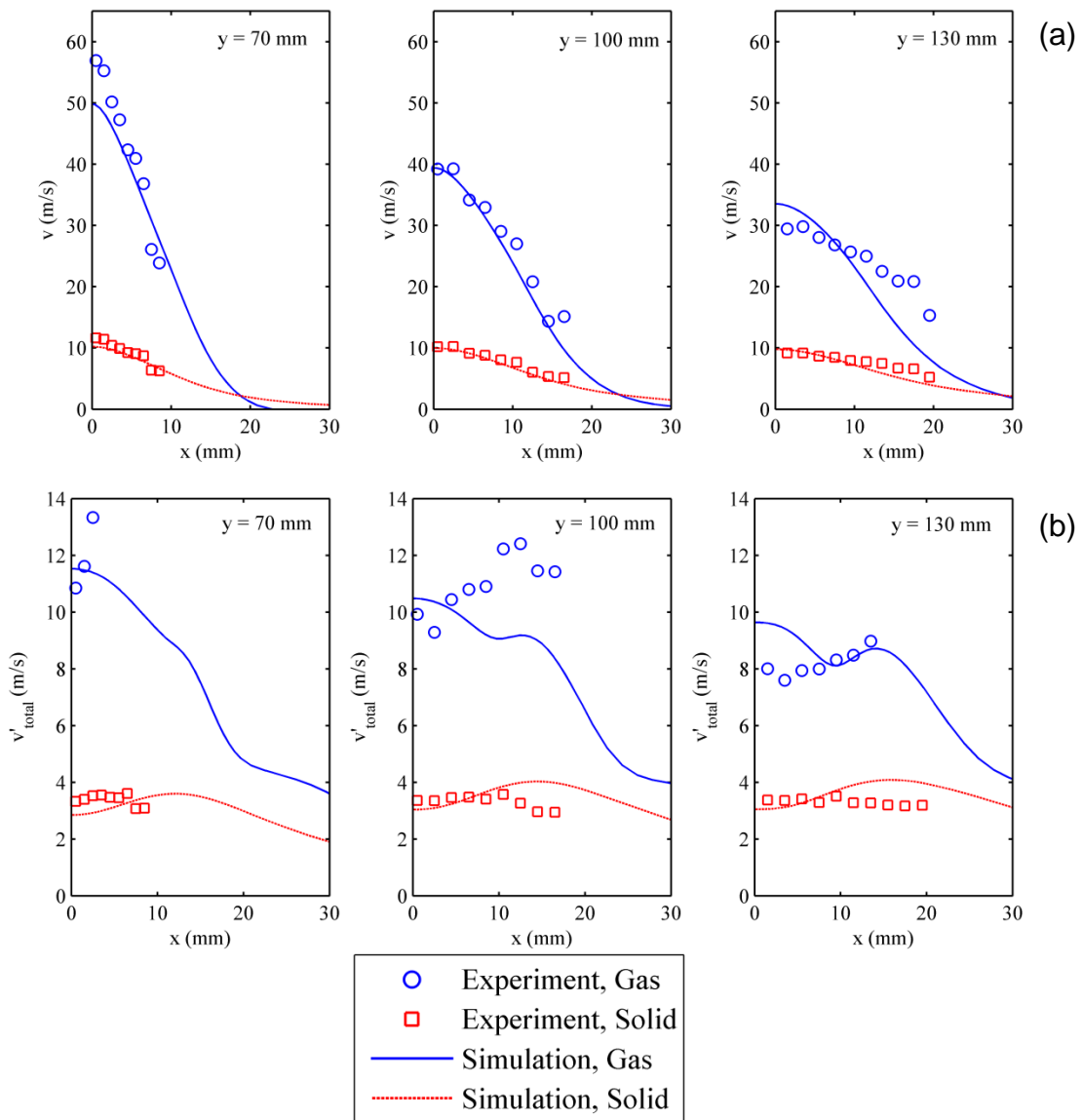


Figure 4-15. Streamwise velocity profiles for $V_{fl} = 1.3V_{mf}$. (a) Mean velocity, and (b) Fluctuating velocity.

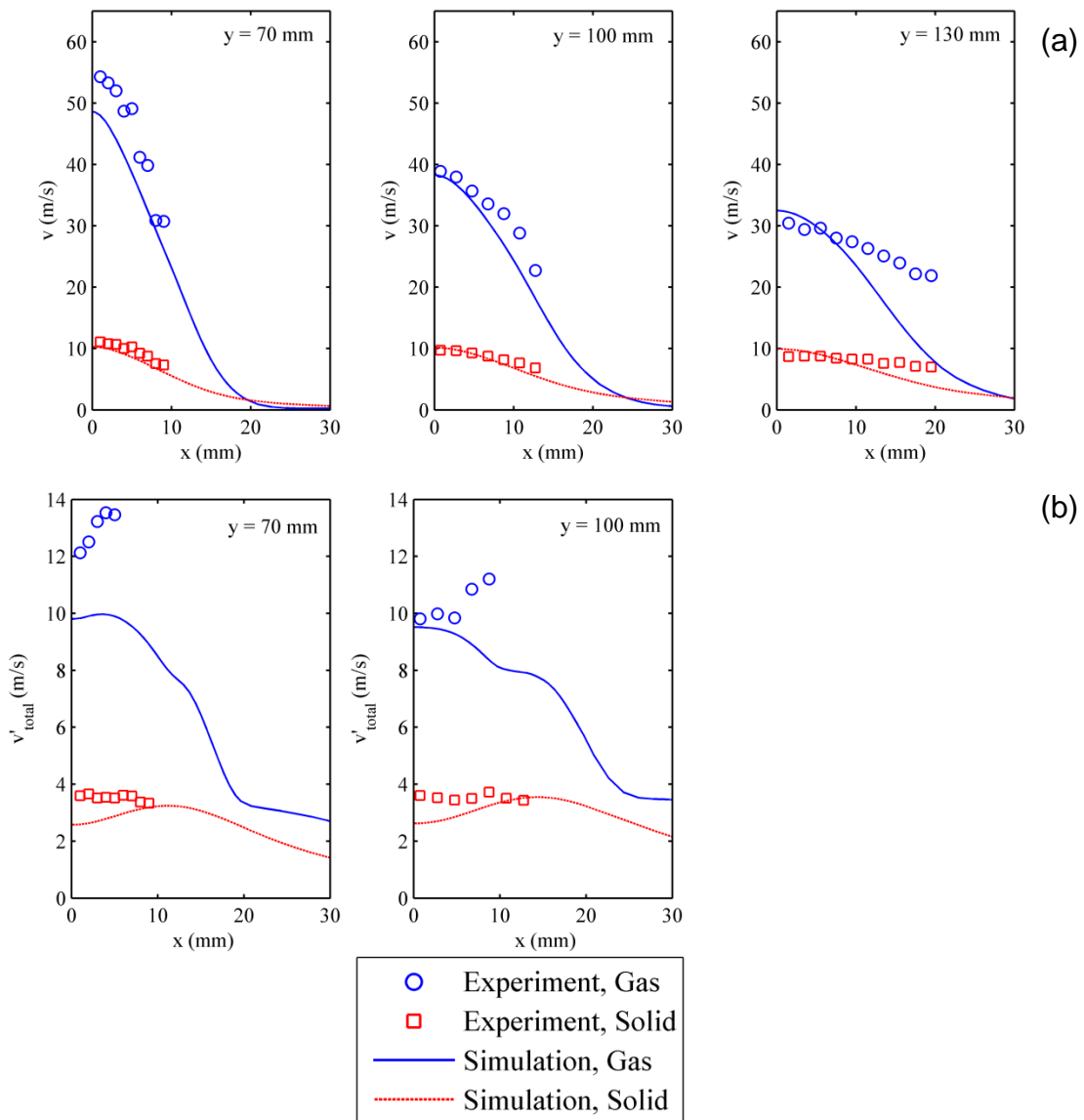


Figure 4-16. Streamwise velocity profiles for $V_{fl} = 1.5V_{mf}$. (a) Mean velocity, and (b) Fluctuating velocity.

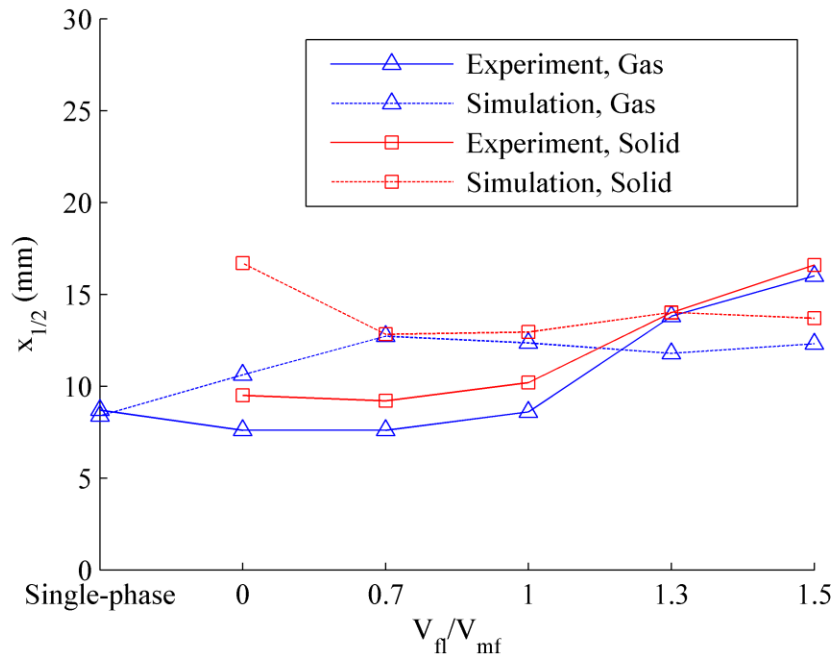


Figure 4-17. Effect of fluidization rate on velocity half-widths at $y = 100$ mm.

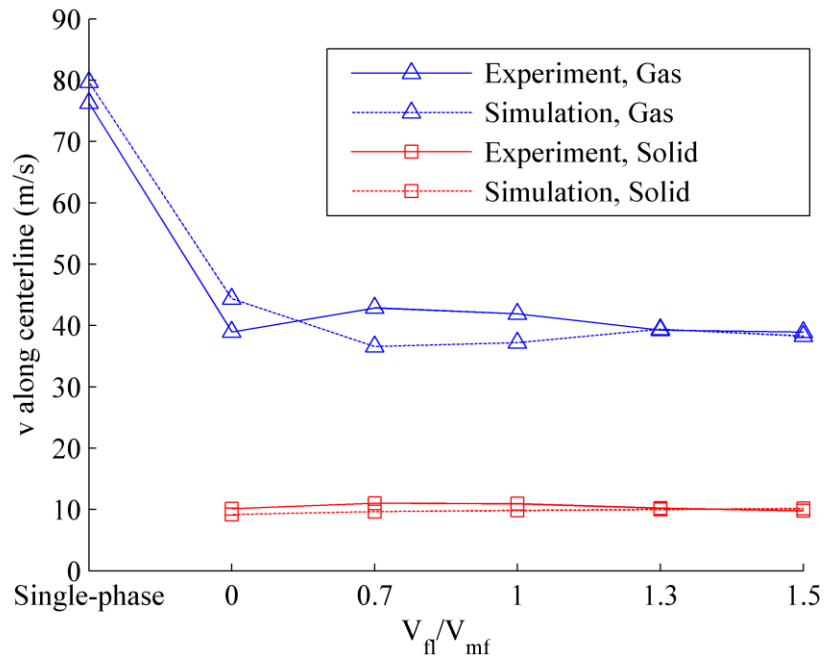


Figure 4-18. Effect of fluidization rate on streamwise mean velocity along the centerline at $y = 100$ mm.

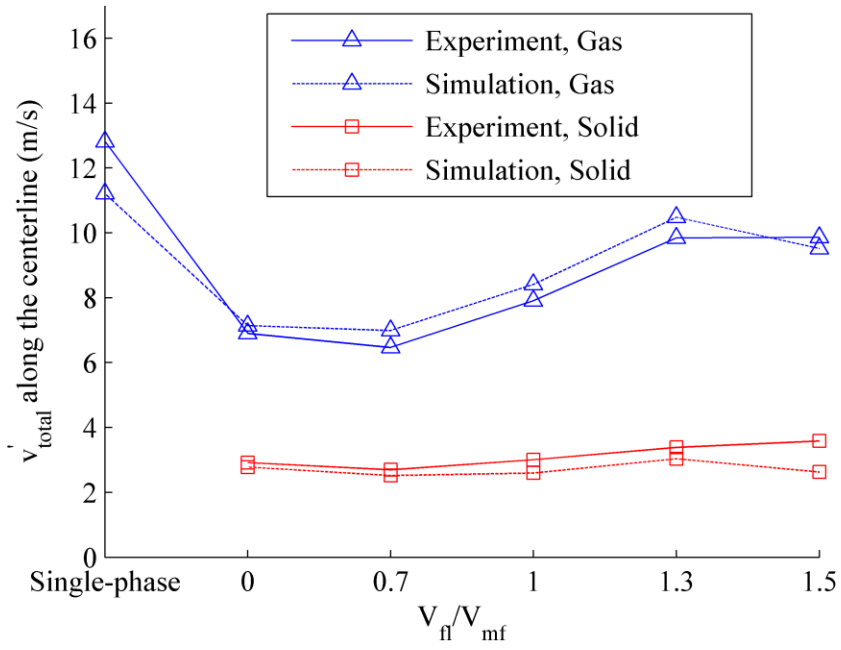


Figure 4-19. Effect of fluidization rate on streamwise fluctuating velocity along the centerline at $y = 100$ mm.

CHAPTER 4 INDUSTRIAL APPLICATION

Background

The ironmaking blast furnace is the dominant route to produce iron. In the lower part of a typical ironmaking blast furnace operation, a hot gas jet at high velocity is injected into a high pressure bed of primarily coke particles forming a cavity in the bed referred to as 'raceway'. The extent of various smelting and reduction reactions that follow is largely determined by the mixing between coke particles and the injected gas, which in turn is related to the size and shape of the raceway formed [28, 29]. Hence, it is important to recognize the key parameters that govern the size and shape of the raceway in order to better understand and predict blast furnace operation.

In-situ experimental investigation is difficult because of the high temperature and harsh nature of the flow. For this reason, physical modeling is widely preferred [30]. A large number of mathematical modeling studies involving prediction of raceway size and shape can be found in the literature [30, 94-103]. Early works describe raceway properties using empirical or semi-empirical correlations [30, 94-96] while, more recently, computational modeling has been the norm [97-103]. In general, the computational modeling studies can be classified into two categories: Combined Continuum and Discrete Modeling (CCDM) and Two-Fluid Modeling (TFM) [28]. In CCDM, the coke particles are treated as discrete entities and their motion is combined with Navier-Stokes equations that describe the continuum flow of the gas phase. CCDM enables one to obtain microscopic information which helps in understanding the movement of individual particles, but is computationally expensive. Most CCDM studies use a small-scale two-dimensional geometry to examine raceway formation. On the

other hand, in TFM, the gas and particles are considered to be interpenetrating continua and conservation equations are solved using closure relations. TFM is preferred for its computational convenience and efficiency which enables one to model a large-scale geometry as encountered in typical industrial blast furnace operations, but its effective use depends on appropriate description of the closure relations.

While CCDM has been used to study raceway properties in a laboratory scale blast furnace [97-101], TFM is relatively less commonly encountered [102, 103]. The most recent work based on TFM is that of Mondal *et al.* [103], who studied the influences of three parameters - jet velocity, initial porosity of the coke bed and the bed height on the shape and size of the raceway zone. The closure for the solid stress in their work included both instantaneous particle-particle interactions (kinetic and collisional regimes) as well as particle-particle interactions due to enduring contacts (frictional regime), which are important in dense regions of the coke bed. A k-epsilon model for the turbulent gas-phase stress was modified to account for the presence of particles. The kinetic and collisional solid stress was described using granular kinetic theory. The frictional shear stress was taken to be proportional to the solids pressure, given by kinetic theory. Such a description for the frictional stress has no conceptual basis, where the frictional shear stress is proportional to the kinetic and collisional pressure, and is not commonly found in published two-fluid, gas-solid flow models. Instead, the frictional stresses, that are significant in dense regions, are commonly described using concepts from soil mechanics as explained in Benyahia [76].

In the present study, the TFM approach adopted by Mondal *et al.* [103] is modified by including an improved description for the frictional stress. The improved friction

model is taken from a widely used expression for frictional pressure based on soil mechanics as proposed by Johnson *et al.* [79], combined with a frictional viscosity that depends on the fluctuations in the solid strain rate as developed by Savage [81]. The influence of six new parameters on raceway predictions are investigated, i.e. particle diameter, outlet pressure, jet location, solids extraction rate, jet angle and domain geometry, in addition to the parameters already investigated by Mondal *et al.* [103].

Model Description

The gas and particle (solid) phases are assumed to behave as interpenetrating continua, as originally proposed by Anderson and Jackson [64]. The governing equations solved in the present study are mass, momentum, granular energy, turbulent kinetic energy and turbulent energy dissipation balances. The closure for the gas-solid drag force is obtained from the drag correlation of Syamlal *et al.* [51] while a standard k-epsilon model is adopted to describe the gas-phase stress. Turbulent gas-particle interaction terms have been neglected in the turbulence equations since including these terms of the form proposed by Simonin [71] produced no significant change in raceway size and shape for the base set of operating parameters tested. The solid stress is assumed to be a sum of kinetic, collisional and frictional contributions, the latter activated above an intermediate solids fraction of 0.5. The kinetic and collisional solid stress is described using granular kinetic theory, which was derived for frictionless spherical particles in a vacuum by Lun *et al.* [72] and slightly modified to account for interstitial gas effects by Agrawal *et al.* [73]. The frictional solid stress is described using soil mechanics concepts with an empirical expression for pressure proposed by Johnson *et al.* [79] and a shear viscosity that depends on the fluctuations in the strain rate, $\mu_s^f \sim D_p \sqrt{\theta}$, as recognized by Savage [81] and modified to blend with the granular

kinetic theory implemented in the present study. The granular assembly has been assumed to deform without any volume change, i.e. at critical state, which has been shown to be an accurate simplification in many dense flows [66]. The boundary conditions for particle velocity and granular temperature at the wall are taken from Johnson and Jackson [86] who considered partial slip arising from collisional momentum loss at the wall. Standard wall functions are imposed for the gas phase. No reaction or thermal energy transfer is considered in this study for simplicity. The TFM model equations used in the present study are summarized in the Appendix and the model parameters specified are shown in Table 5-1.

Method of Solution

The TFM equations are solved by a finite volume approach in a compressible fashion following the ideal gas law, using an open source code - Multiphase Flows with Interphase Exchanges (MFIx). The details of the numerical technique can be found in Syamlal *et al.* [51]. The maximum residual at convergence is set to 1×10^{-3} for the continuity and momentum equations combined and 1×10^{-4} for the granular energy, turbulent kinetic energy and turbulent dissipation equations respectively. The simulation domain is chosen to represent a typical sub-section of an industrial scale blast furnace – a cuboid of length 3.7 m, width 1 m and height 5 m (Figure 5-1). Gravity acts in the negative z direction. The jet orifice is a square of side $D_j = 0.15$ m, located at a height H_j from the bottom. Initially a stagnant, uniform solid phase of porosity ϵ_i is specified to occupy the space from the bottom to a bed height of H_i . The boundary conditions imposed are a constant gas mass inflow corresponding to a horizontal velocity, U_j , and gas density, 1.1 kg/m^3 at the orifice, and a constant pressure outflow corresponding to a

pressure of P_o at the top boundary ($z = 5$ m). Wall conditions are specified on all other boundaries.

The physical properties of gas and particles specified in the present study are summarized in Table 5-2. The operating parameters that were varied are shown in Table 5-3. The inlet values of turbulent kinetic energy and turbulence dissipation at the orifice are fixed at $39 \text{ m}^2/\text{s}^2$ and $2692 \text{ m}^2/\text{s}^3$ respectively. These values have been estimated using standard CFD guidelines corresponding to a jet velocity of $U_j = 165$ m/s.

$$k_j = \frac{3}{2} (0.16 U_j Re_j^{-1/8})^2 \quad (5-1)$$

$$\varepsilon_j = 0.1643 \left(\frac{k_j^{1.5}}{l_e} \right) \quad (5-2)$$

where, k_j is turbulent kinetic energy at inlet; ε_j is turbulent dissipation at inlet; Re_j is Reynolds number at the inlet; l_e is turbulence length scale approximated as 0.1 times the jet diameter D_j .

The sensitivity of the inlet turbulence values on the raceway results was found to be negligible. A structured but non-uniform mesh of $\sim 132,000$ grids with more grids close to the jet orifice was chosen after ensuring that the mesh produced grid insensitive results. Starting from $t = 0$, the simulations took approximately 2 s of real time to reach a steady state after which there was negligible change in raceway size or shape. All results are analyzed after such a stable state was reached. Each simulation took roughly 3 days, running parallel on 2 processors, at the National Computational Infrastructure (NCI) Facility in Australia.

Results and Discussion

The boundary of the raceway region is characterized by a contour of constant porosity equal to 0.5 for all cases considered in this paper. The physical basis for choosing this value comes from the continuum model description which estimates that enduring particles are significant only below a porosity of 0.5, above which the particle movement is governed by instantaneous collisions. The time evolution of raceway formation is shown in Figure 5-2 for the base set of parameters. Since the base conditions correspond to a loosely packed bed, the time evolution shows that as the bed compacts, the raceway size becomes smaller until a steady raceway is formed after roughly 2 s of real time.

To visualize the general nature of flow that occurs after a stable raceway is formed, vector plots of mean gas and particle velocities and the dense phase porosity distribution along the central y slice at $t = 2$ s are shown in Figure 5-3.

From Figure 5-3a it can be observed that a majority of the region beyond the raceway, except very close to the boundary, is a packed bed where the particles do not move to a significant extent, but the gas penetrates through the voids of the packed bed. The gas velocities show that gas enters horizontally from the jet orifice, loses velocity through the raceway, and escapes out of the voids in the packed bed. Two-patterns can be observed - a high-speed central jet and recirculation. That is, there is entrainment of gas towards the jet axis from the top and bottom regions of the raceway very near the orifice; otherwise, the gas flow is predominantly outward of the jet axis. The particle velocities show that while in the region beyond the raceway boundary particles hardly move, inside the raceway there is significant particle movement. Particles move towards the jet axis from the top and bottom regions of the raceway

close to the orifice (entrainment zone). Some of the particles are transported horizontally along the jet axis until they can no longer move upon hitting the boundary of the packed bed, and the rest of the particles are recirculated back towards the orifice along the top and bottom boundaries (recirculation zone). This particle motion is more significant in the top part of the raceway than the bottom. With regard to the forces that govern particle motion inside the raceway, the particle velocity tends to follow the gas velocity along the jet axis. Therefore, the horizontal acceleration near the orifice can be attributed to the gas-solid drag force. Further downstream, particles retard due to collision with the packed bed region. The entrainment of particles near the jet orifice is caused primarily by drag. The weight of the particles enhances entrainment from the top and opposes entrainment from the bottom. The particle recirculation along the top and bottom boundaries away from the orifice is driven by particle-particle interactions. Figure 5-3b illustrates the porosity distribution in the packed bed region of the furnace for the base case. It can be seen that the porosity in the dense-phase region, as predicted by the frictional model, decreases rapidly close to the surface and slower towards the bottom of the particle bed.

The effects of the key parameters on raceway size and shape are discussed comprehensively in the next sections. The effect of each parameter on the raceway size, defined as the penetration depth in the horizontal direction, and shape of the raceway is investigated one at a time, keeping all other parameters fixed at their base values.

Jet Inlet Velocity

Jet inlet velocities of $U_j = 165, 195, 220$ and 250 m/s were simulated. It is found that increasing the horizontal jet velocity increases the raceway size. However, there is

only a small change in raceway shape (Figure 5-4). This can be explained by the increase in horizontal momentum of the gas which is transferred to the particles. The particles are dragged further into the bed before the retardation caused by the packed bed prevents any further horizontal penetration. This trend agrees well with the findings of other authors [101, 103-105].

Particle Diameter

Increasing particle diameter from $D_p = 2$ cm through $D_p = 6$ cm reduces the raceway size, accompanied by a narrowing of raceway shape (Figure 5-5). This behavior is due to a combination of a decrease in the drag force and increase in the particle resistance (solids frictional viscosity) with increase in particle size. The particles are not dragged sufficiently far horizontally, and higher particle resistance to flow prevents a larger region of particles from taking part in the entrainment and recirculation process. This qualitative behavior with respect to particle size is also in agreement with other works [99, 105].

Outlet Pressure

In the ironmaking blast furnace, high top pressure is usually adopted and the top pressure varies with operating conditions. In this study, outlet pressures of $P_o = 2.61$, 4.61 and 7.61 atm were simulated. From Figure 5-6, it can be seen that increasing the outlet pressure decreases the raceway size accompanied by some change in the raceway shape as well. The outlet pressure controls the gas pressure inside the bed, which in turn is directly proportional to the gas density. Hence, for the same mass inflow, the gas velocities decrease with increase in outlet pressure resulting in lower gas-solid drag and shorter, narrower raceways.

Initial Bed Height

In the ironmaking blast furnace, the solid loading above the raceway varies with the furnace shape and operating conditions. In this study, the computational domain does not describe the entire furnace but only the lower part of the furnace. For this reason, it is necessary to investigate the initial bed height. The initial bed height determines the weight of particles in the bed. Figure 5-7 shows that increasing the initial height of the bed decreases the raceway size and narrows the shape at small heights. However, above height $H_i = 4.5$ m of solids, the size or shape of the raceway does not change with further increase in bed height. This behavior is attributed to the variation in local porosity in a packed bed assembly as a function of the height of the bed. At small heights, the porosity decreases significantly with bed height causing smaller raceways, but after a sufficiently large bed height, there is negligible change in porosity upon increasing height. The maximum bed height ($H_i = 6$ m) was simulated in a domain of height $z = 6.5$ m. This behavior with respect to bed height is comparable with the findings of other authors [103, 105].

Jet Location

The jet orifice was located at different heights of $H_j = 2.5$, 1.2 and 0.3 m (Figure 5-8). All the three heights have been plotted in the same figure to enable easier comparison. While there is significant change in raceway size and shape when inlet height is decreased from $H_j = 2.5$ m to 1.2 m, negligible influence on raceway size and shape is observed below height $H_j = 1.2$ m. The reason for such a behavior with change in jet location is because there is no significant change in the packed bed porosity in the region where the jet penetration occurs with further decrease in inlet height. This is the same trend that was seen when increasing the initial height of the bed.

Initial Porosity

Three different initial porosities of $\varepsilon_i = 0.6, 0.5$ and 0.4 were simulated with varying initial bed heights, so as to keep the total mass of particles a constant. The results (Figure 5-9) show only a small change in the size and shape of the raceway with change in porosity. A loosely packed bed of particles simply falls to its randomly packed state ($\varepsilon \sim 0.4$) resulting in a similar steady state configuration for all the three porosities. Narrowing of the raceway at $\varepsilon_i = 0.6$ can be attributed to a small dependence of the steady state solution on initial conditions, a hysteresis phenomenon in raceway formation which has been noted in literature [97]. The maximum porosity case ($\varepsilon_i = 0.6$) was simulated in a computational domain of height $z = 6$ m to accommodate the increased bed height. The results presented here with regards to the effect of the initial porosity do not agree with Mondal *et al.* [103], who found that increasing initial porosity from $\varepsilon_i = 0.4$ to 0.5 significantly narrows the raceway shape, accompanied by a decrease in size. It is to be noted that the other porosities considered by Mondal *et al.*, $\varepsilon_i = 0.2$ and 0.3 , correspond to unphysical conditions of spherical packing densities greater than 0.65 and hence have been neglected in the present comparison. It is also unclear what maximum packing value was used in their work. Hence, the reason for the disagreement in the effect of initial porosity is due to the lack of frictional pressure in the gas-solid flow modeling of Mondal *et al.* [103]. The frictional pressure drives the dense bed to reach the random packing state, without which unphysical porosity distribution may result depending on the initial state, since the dense bed porosity distribution is then governed by the radial distribution function.

Particle Downward Extraction

To describe the slow particle extraction that mimics the solid loss due to coke combustion or carbon dissolution in the lower part of a blast furnace, a constant solids mass outflow condition was specified at the bottom boundary ($z = 0$). Such a method to approximate the effect of loss in solids has been successfully applied in the experimental study of Pinson *et al.* [106]. Solids mass flow rates of $m_s = 0.82$ kg/s and 16.4 kg/s were simulated for a jet velocity of $U_j = 165$ m/s. In order to compensate for the loss in solids with time, the initial bed height was increased from $H_i = 4.5$ m to $H_i = 6$ m, which is above the critical height and hence should not affect the raceway (Figure 5-7). The domain height was increased to $z = 6.5$ m to accommodate the increased bed height. The time to predict a stable raceway formation was longer, 10s of real time, at the highest solids extraction rate. While there is no change in raceway size or shape at a small rate of extraction of $m_s = 0.82$ kg/s, a significant increase in size and change in shape is observed at a downward solids extraction rate of $m_s = 16.4$ kg/s (Figure 5-10). This behavior with respect to solids extraction is attributed to the increase in porosity of the packed bed assembly as solids are extracted downward at high rates. Such a trend with particle extraction was also found in the CCDM work of Feng *et al.* [101].

Jet Angle

In order to simulate the condition where the jet inlet pipe makes an angle $-\alpha$ with the horizontal plane, the inlet boundary conditions were specified as $U_j' = U_j \cos \alpha$, $V_j' = -U_j \sin \alpha$ and the orifice length in the z direction changed correspondingly to $D_j / \cos \alpha$. No significant effect on the raceway size or shape was observed when changing the inlet jet angle from 0 to 15 degrees.

Domain Geometry

In the present study a simplified Cartesian geometry has been assumed, but real blast furnace sub-sections have slanting edges at the sides [107]. To test the effect this could have on raceway properties while still using staircase mesh implementation, the simulation domain was changed as shown in Figure 5-11a. The jet enters the bed of particles via an inlet pipe and there is a cut in the bed at a height of 1.05 m from the bottom.

A simulation with base parameters was performed using this domain and no significant difference was found in the resulting raceway size or shape when compared to the corresponding simulation run using the original domain (Figure 5-11b). This suggests that a simple Cartesian geometry captures the stresses in the coke bed quite accurately.

Summary

There is a lack of two-fluid modeling studies with appropriate closure relations that explore raceway properties in a blast furnace operation. To address this issue, a TFM approach has been undertaken to understand the flow behavior and investigate the influences of various operating parameters on the size and shape of a raceway. The model uses soil mechanics concepts to include the effect of enduring contacts (friction) between particles while describing the solid-phase stress, and employs k-epsilon turbulence equations to describe the gas-phase stress. Simulation results show that increasing jet velocity increases raceway size without considerable change in shape, whereas changing particle size and outlet pressure affects both size and shape considerably. Increasing the height of coke particles in the bed decreases size and narrows the raceway at small heights but produces no change beyond a certain height.

Same trend is observed when decreasing the height at which the jet is located. Varying the initial bed porosity has no significant effect since a loosely packed bed tends to fall to its random packing state, but the narrowing of raceway at high porosity suggests some hysteresis effect. Extracting solids from the bottom has the tendency to increase raceway size and change the shape as the bed becomes more porous. Small changes in the jet injection angle and geometry of the domain were found to have negligible effect on the raceway properties. Work that uses the details of these simulation results, in particular the porosity distribution of coke inside the raceway [108], to quantitatively predict the reaction efficiencies in the lower part of a blast furnace, is currently under progress.

Table 5-1. Model parameters specified.

Parameter	Description	Value
$\sigma_k, \sigma_\varepsilon, C_{1\varepsilon}, C_{2\varepsilon}, C_\mu$	Constants in k-epsilon gas turbulence model	1.0, 1.3, 1.44, 1.92, 0.09
E, κ_v	Constants in standard wall functions for gas	9.81, 0.42
$\acute{\alpha}$	Constant in granular theory	1.6
$Fr, r, s, \varepsilon_s^{min}, \varepsilon_s^{max}$	Constants in frictional pressure expression	0.05 N/m ² , 2, 5, 0.5, 0.65
φ	Specularity coefficient	0.002

Table 5-2. Physical properties specified.

Parameter	Description	Value
MW	Molecular weight of gas	29
T	Temperature of gas	1473 K
μ_g	Gas viscosity	5.37e-5 kg/(ms)
ρ_s	Particle density	900 kg/m ³
e	Particle-particle coefficient of restitution	0.8
e_w	Particle-wall coefficient of restitution	0.8
δ	Angle of internal friction	27 deg
δ_w	Angle of wall friction	27 deg

Table 5-3. Operating parameters that were varied.

Parameter	Description	Value
D_j	Jet orifice diameter	0.15 m
U_j	Inlet jet horizontal (x) velocity	165*, 195, 220, 250, 280 m/s
α	Angle made by jet inlet with the horizontal plane in the downward ($-z$) direction	0*, 5, 15 degrees
H_j	Height of jet orifice from the bottom	0.3*, 1.2, 2.5 m
P_o	Outlet pressure	2.61, 4.61*, 7.61 atm
ϵ_i	Initial porosity of the bed	0.4, 0.5*, 0.6
H_i	Initial bed height	1.8, 3, 4.5*, 6 m
D_p	Particle diameter	2, 4*, 6 cm
m_s	Solids downward extraction rate	0*, 0.82, 16.4 kg/s

* Base parameters.

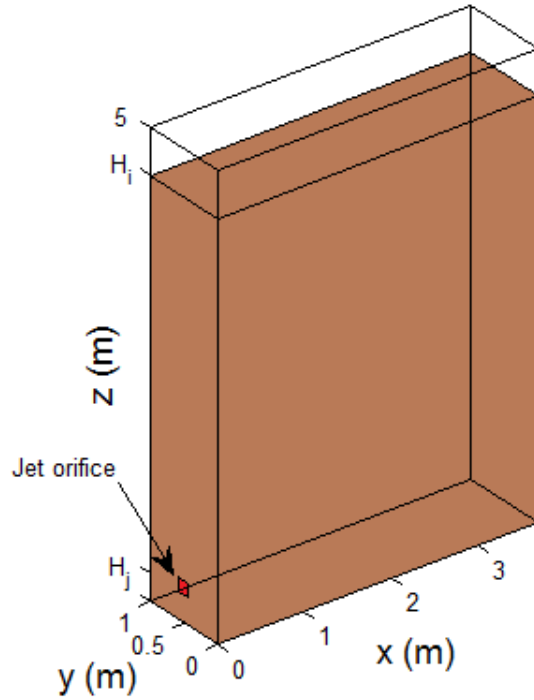


Figure 5-1. Simulation domain for the lower part of ironmaking blast furnace.

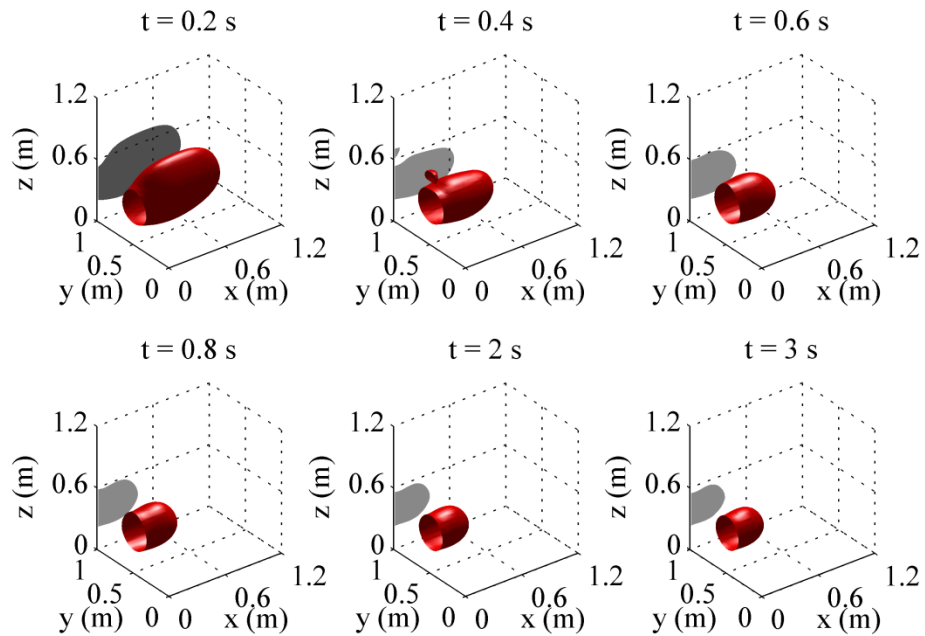


Figure 5-2. Time evolution of raceway size and shape for the base case.

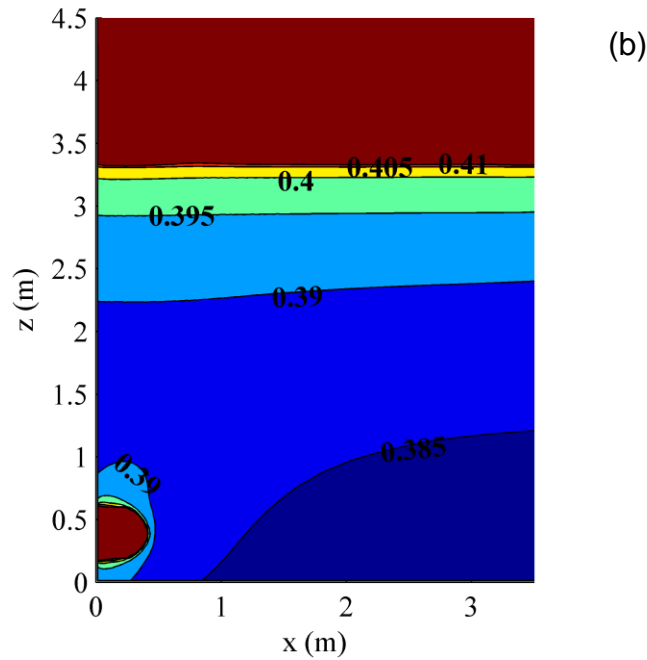
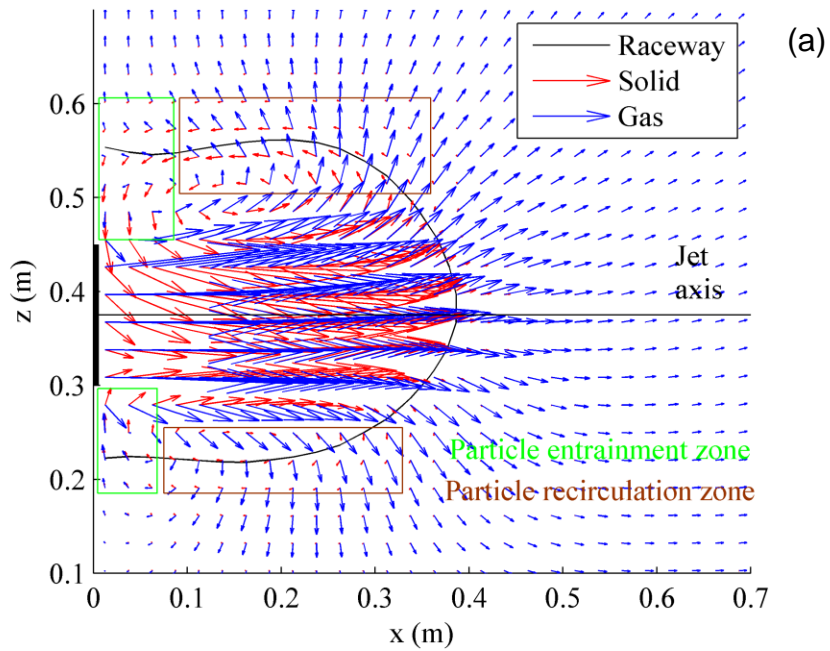


Figure 5-3. Flow visualization along the plane $y = 0.5$ m at $t = 2$ s for the base case. (a) Vector plot of mean gas and mean particle velocity. The magnitude of the gas velocity has been reduced by a factor of 30 compared to solid velocity. (b) The dense phase porosity distribution in the packed region beyond the raceway.

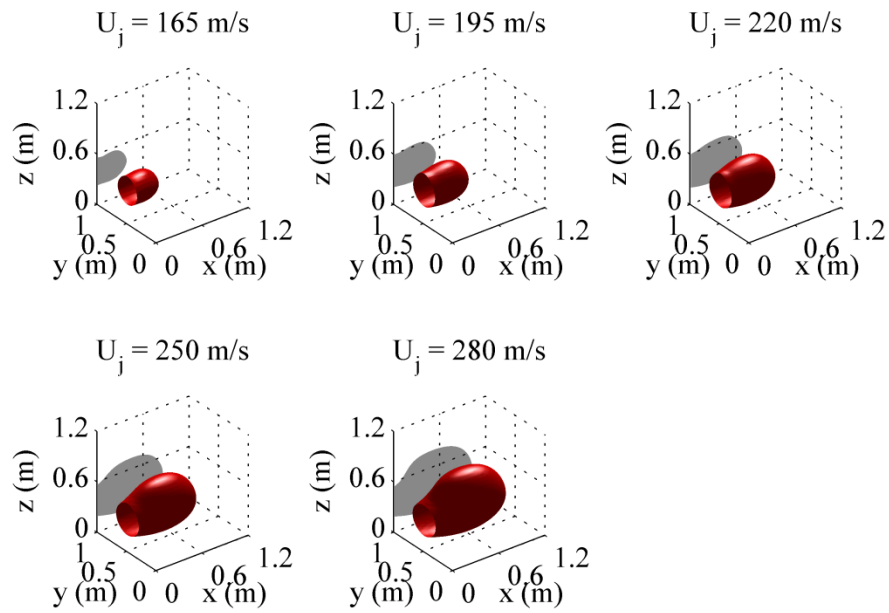


Figure 5-4. Effect of inlet jet velocity on raceway size and shape.

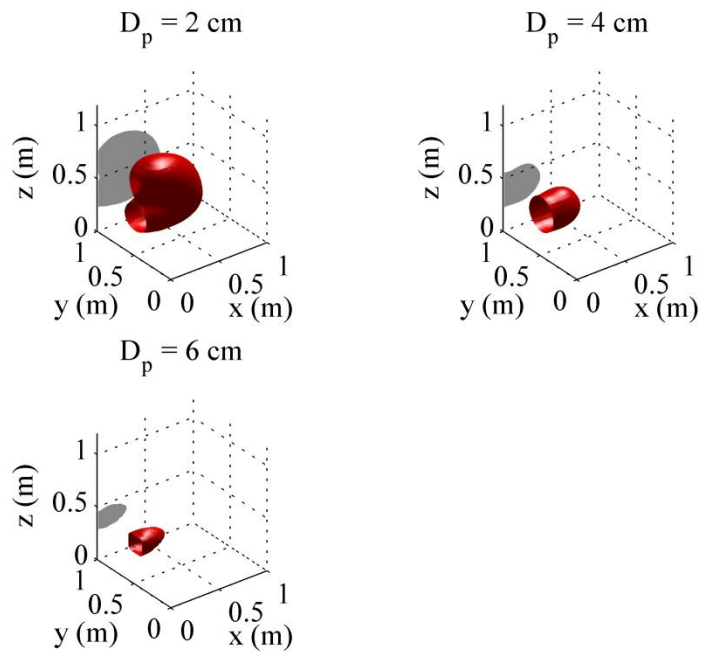


Figure 5-5. Effect of particle diameter on raceway size and shape.

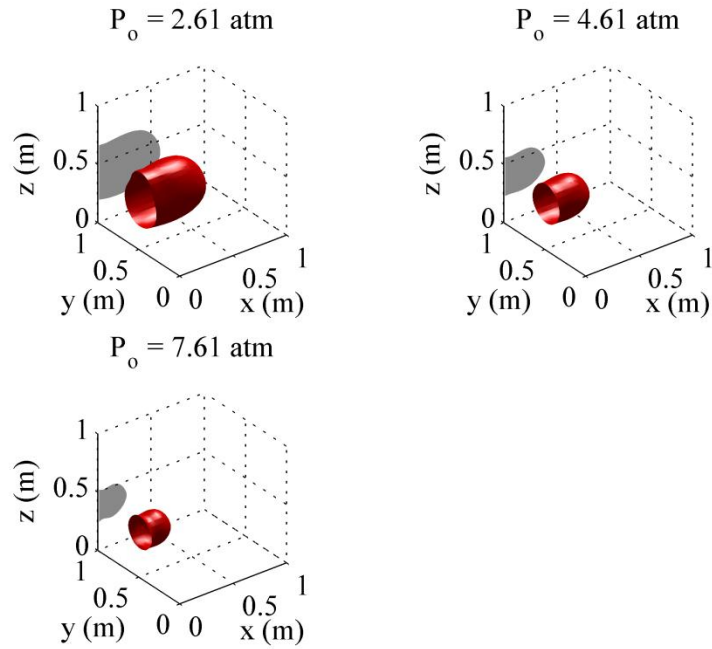


Figure 5-6. Effect of outlet pressure on raceway size and shape.

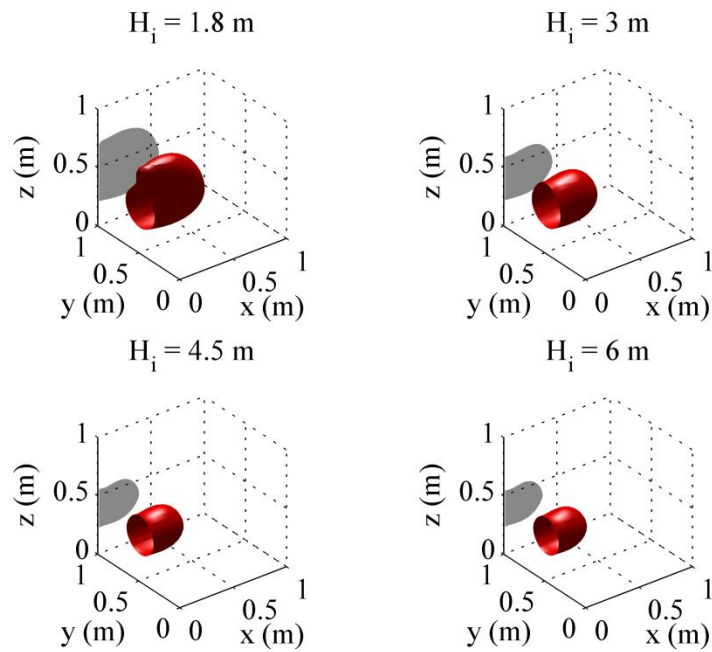


Figure 5-7. Effect of initial bed height on raceway size and shape.

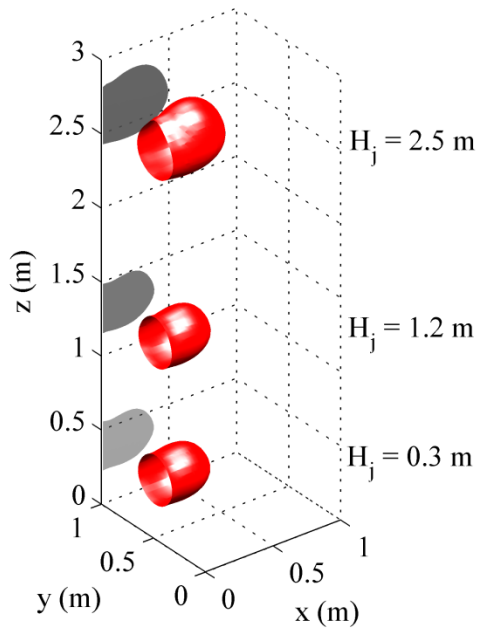


Figure 5-8. Effect of jet location on raceway size and shape.

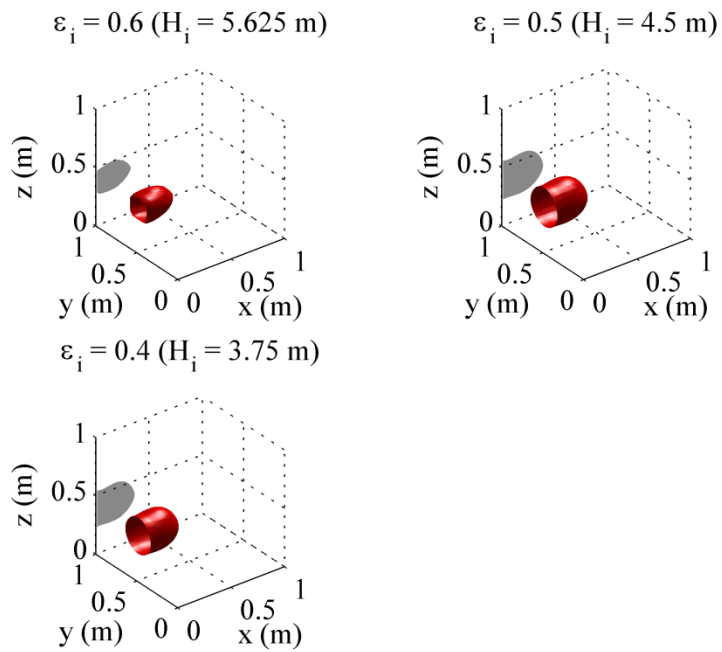


Figure 5-9. Effect of initial porosity on raceway size and shape.

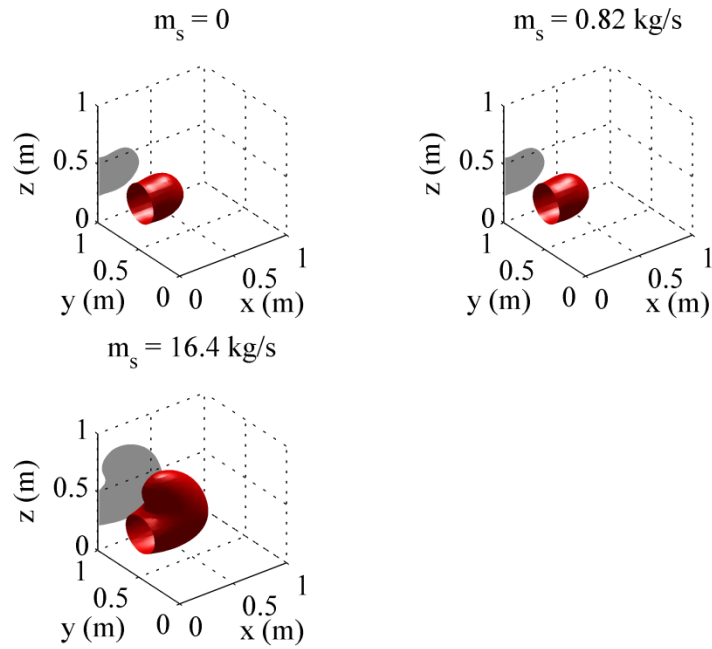


Figure 5-10. Effect of solids downward extraction on raceway size and shape.

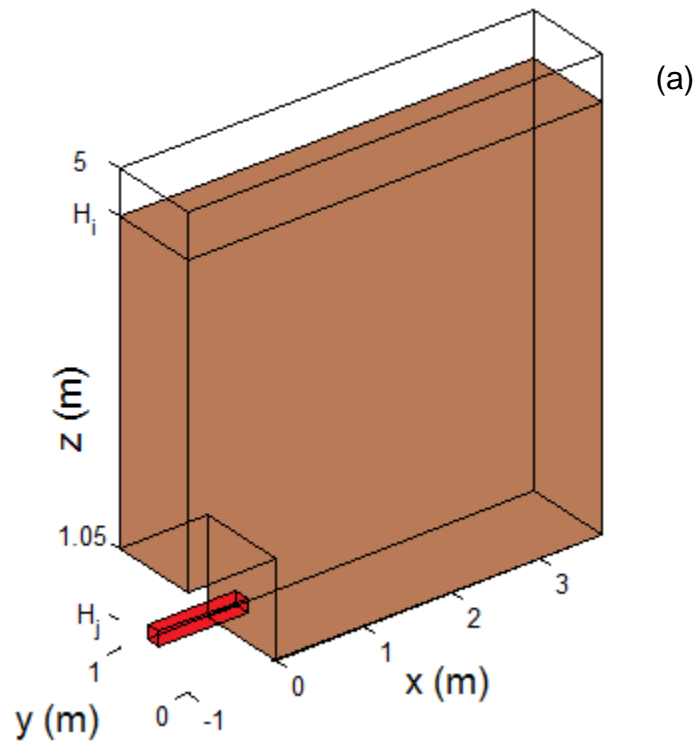


Figure 5-11. Modified simulation domain. (a) Domain dimensions. (b) Influence on raceway size and shape.

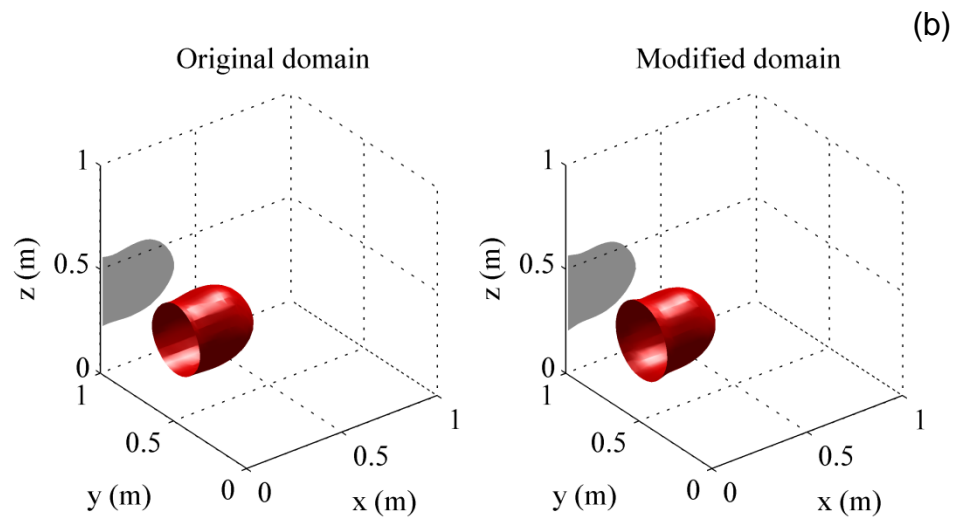


Figure 5-11. continued.

CHAPTER 6 CONCLUSIONS AND RECOMMENDATIONS

Contributions were made in four topics of particulate technology research as identified in Chapter 1, which will help in the modeling and industrial application of bubbling gas-solid flows with jet injection. The main findings in each topic and suggestions for future work are explained below.

Experimental Measurements

The fluctuating velocities of gas and solid phases were obtained inside the jet plume region of a bubbling bed. This was made possible with the non-intrusive measurement technique of laser Doppler velocimetry. The results indicate that increasing fluidization rate above minimum fluidization increases the intensity of fluctuations in both phases. There is also a tendency for the fluctuating intensity to decrease upon increasing distributor velocity when below minimum fluidization. A discussion on the coupling between the two phases that occurs via the mean flow properties of void fraction, plume half-width and centerline mean velocities was proposed to explain the observations. The contributions to the overall fluctuations from the bubbling emulsion action and the turbulent energy transfer were also noted. These fluctuation measurements and analysis provide detailed insight on the two-phase transport inside the jet plume region of a bubbling fluidized bed with jet injection. They also provide valuable data for the validation of computational models.

For future work it is recommended that direct measurements of solids fraction be made to complement the velocity measurements obtained as part of this thesis and Mychkovsky [36]. This would provide more comprehensive data for evaluating computational models. Methods for obtaining direct and non-intrusive concentration

profiles include gamma-ray absorption or x-ray densitometry techniques. Further, particle size distribution and shape effects can also be systematically investigated.

Single-Phase Numerical Study

A CFD study was conducted in Chapter 3 to examine the role of bounding sidewalls in a planar jet experimental setup. The findings show that increasing the aspect ratio decreases the mean velocity decay rate, lowers the turbulent kinetic energy intensity, and decreases jet half-width. The exact downstream location where the bounding wall influence becomes significant was determined as a function of the nozzle aspect ratio. While the study conducted in this thesis is limited to single-phase jets, a similar numerical approach may be extended to examine two-phase particle-laden jet flows confined between bounding walls.

Validating a Gas-Solid Continuum Model

The evaluation of a gas-solid continuum model against comprehensive experimental data was conducted in Chapter 4. This study facilitated a detailed understanding of the continuum framework, especially where the main empiricisms and uncertainties lie. It was seen that while the descriptions for solid kinetic and collisional stress, and gas-solid drag are fairly well-established in literature, there is no consensus on the descriptions for frictional stress and turbulent interaction terms, both of which are significant in bubbling bed flows with high-speed jet injection. Therefore, the descriptions for these two terms were determined by conducting a step-by-step comparison with appropriate experiments. With the help of experimentally measured fluidization curve, the empirical constants in the frictional pressure expression were verified, and the most appropriate frictional viscosity description was determined using experimental videos. The gas turbulence modulation term was then found with the help

of the gas fluctuating velocity profile measured inside the jet plume. The final continuum model was found to predict the mean and fluctuating velocity profiles inside the jet plume reasonably well. A discussion on the reasons for mismatches between the experiment and model prediction was also made in Chapter 4.

While such an approach for modeling bubbling beds is expected to work successfully in industries, it may not always be possible to obtain experimental data which are required to calibrate certain closure relations. Therefore, for future work on this topic, it is recommended that more fundamental turbulence interaction and frictional stress models be developed so that experimental requirements may be reduced. One method of improving frictional model description is by using the more fundamental approach of DEM to develop continuum expressions for solid stress. A more general turbulence interaction description, on the other hand, is a bigger challenge and first requires extensive non-intrusive measurements of two-phase fluctuating velocities at different Reynolds numbers and solids concentrations.

Further, as mentioned in Chapter 4, two-dimensionality has been assumed while solving the two-phase continuum equations in the validation study. While this assumption is reasonable given the results of the single phase numerical study and the fact that the LDV experimental data indicate two-dimensional self-similarity profiles, for future work it is recommended that three-dimensional simulations with the exact experimental geometry be conducted to verify this assumption.

Industrial Application

The continuum approach with suitable closure relations was employed in Chapter 5 to study the influence of operating parameters on the size and shape of the raceway formed in the lower part of an industrial-scale blast furnace operation. The findings

reveal that increasing jet inlet velocity increases the raceway size without much change in the shape, whereas changing outlet pressure, coke particle diameter and particle extraction rate affect the size and shape considerably. Increasing the height of coke particles in the bed decreases size and narrows the raceway at small heights but produces no change beyond a certain height. Same trend is observed when decreasing the height at which the jet is located. Varying the initial bed porosity has no significant effect since a loosely packed bed tends to fall to its random packing state, but the narrowing of raceway at high porosity suggests some hysteresis effect.

While the above study was conducted in the absence of chemical reactions (cold-flow modeling) to study how raceway properties are affected by operating conditions, a more direct application from the industrial point of view would be to estimate how the reaction efficiency of the blast furnace is affected by operating conditions. For this purpose, it is recommended that the results of the cold-flow simulations conducted in Chapter 5, be fed into a reactive model to estimate reaction efficiencies directly.

APPENDIX A
MODEL EQUATIONS FOR CHAPTER 5

Governing Equations

Gas-phase mass balance

$$\frac{\partial \varepsilon_g}{\partial t} + \nabla \cdot (\varepsilon_g \underline{u}_g) = 0 \quad (\text{A1})$$

Solid-phase mass balance

$$\frac{\partial \varepsilon_s}{\partial t} + \nabla \cdot (\varepsilon_s \underline{u}_s) = 0 \quad (\text{A2})$$

Gas-phase momentum balance

$$\rho_g \varepsilon_g \left[\frac{\partial \underline{u}_g}{\partial t} + \underline{u}_g \cdot \nabla \underline{u}_g \right] = -\varepsilon_g \nabla p_g + \nabla \cdot (\varepsilon_g \underline{\underline{\tau}}_g) - \underline{F}_D + \varepsilon_g \rho_g \underline{g} \quad (\text{A3})$$

Solid-phase momentum balance

$$\rho_s \varepsilon_s \left[\frac{\partial \underline{u}_s}{\partial t} + \underline{u}_s \cdot \nabla \underline{u}_s \right] = -\varepsilon_s \nabla p_g + \nabla \cdot \underline{\underline{\sigma}}_s + \underline{F}_D + \varepsilon_s \rho_s \underline{g} \quad (\text{A4})$$

Turbulent kinetic energy balance

$$\rho_g \varepsilon_g \left[\frac{\partial k}{\partial t} + \underline{u}_g \cdot \nabla k \right] = \nabla \cdot \left(\varepsilon_g \frac{\mu_g^t}{\sigma_k} \nabla k \right) + \varepsilon_g \underline{\underline{\tau}}_g : \nabla \underline{u}_g - \varepsilon_g \rho_g \varepsilon \quad (\text{A5})$$

Turbulent kinetic energy dissipation balance

$$\rho_g \varepsilon_g \left[\frac{\partial \varepsilon}{\partial t} + \underline{u}_g \cdot \nabla \varepsilon \right] = \nabla \cdot \left(\varepsilon_g \frac{\mu_g^t}{\sigma_\varepsilon} \nabla \varepsilon \right) + \varepsilon_g \frac{\varepsilon}{k} \left(C_{1\varepsilon} \underline{\underline{\tau}}_g : \nabla \underline{u}_g - \rho_g C_{2\varepsilon} \varepsilon \right) \quad (\text{A6})$$

Granular energy equation

$$\frac{3}{2} \rho_s \varepsilon_s \left[\frac{\partial \theta}{\partial t} + \underline{u}_s \cdot \nabla \theta \right] = \nabla \cdot (\kappa_s \nabla \theta) + \underline{\underline{\sigma}}_s^{kc} : \nabla \underline{u}_s - \varepsilon_s \rho_s J_s + \pi_\theta \quad (\text{A7})$$

Constitutive Relations

Gas-solid drag coefficient

$$\underline{F}_D = \beta (\underline{u}_g - \underline{u}_s) \quad (\text{B1-1})$$

$$\beta = \frac{3\varepsilon_s \varepsilon_g \rho_g}{4V_r^2 D_p} \left(0.63 + 4.8 \sqrt{\frac{V_r}{Re}} \right)^2 |\underline{u}_g - \underline{u}_s| \quad (\text{B1-2})$$

$$V_r = 0.5(A - 0.06Re + \sqrt{(0.06Re)^2 + 0.12Re(2B - A) + A^2}) \quad (\text{B1-3})$$

$$A = \varepsilon_g^{4.14} \quad (\text{B1-4})$$

$$B = \begin{cases} 0.8\varepsilon_g^{1.28}, & \varepsilon_g \leq 0.85 \\ \varepsilon_g^{2.65}, & \varepsilon_g > 0.8 \end{cases} \quad (\text{B1-5})$$

$$Re = \frac{D_p |\underline{u}_g - \underline{u}_s|}{\mu_g} \quad (\text{B1-6})$$

Gas-phase stress

$$\underline{\underline{\tau}}_g = \mu_g^e \left[\nabla \underline{u}_g + \nabla \underline{u}_g^T - \frac{2}{3} (\nabla \cdot \underline{u}_g) \underline{\underline{I}} \right] \quad (\text{B2-1})$$

$$\mu_g^e = \mu_g + \mu_g^t \quad (\text{B2-2})$$

$$\mu_g^t = \rho_g C_\mu \frac{k^2}{\varepsilon} \quad (\text{B2-3})$$

Solid-phase stress

$$\underline{\underline{\sigma}}_s = \underline{\underline{\sigma}}_s^{kc} + \underline{\underline{\sigma}}_s^f \quad (\text{B3-1})$$

$$\underline{\underline{\sigma}}_s^{kc} = \left(-p_s^{kc} + \eta \mu_b^{kc} \nabla \cdot \underline{u}_g \right) \underline{\underline{I}} + \mu_s^{kc} \left[\nabla \underline{u}_s + \nabla \underline{u}_s^T - \frac{2}{3} (\nabla \cdot \underline{u}_s) \underline{\underline{I}} \right] \quad (\text{B3-2})$$

$$p_s^{kc} = \varepsilon_s \rho_s \theta (1 + 4\eta \varepsilon_s g_0) \quad (\text{B3-3})$$

$$\mu_s^{kc} = \left(\frac{2 + \alpha}{3} \right) \left[\frac{\mu_s^{kc*}}{g_0 \eta (2 - \eta)} \left(1 + \frac{8}{5} \eta \varepsilon_s g_0 \right) \left(1 + \frac{8}{5} \eta (3\eta - 2) \varepsilon_s g_0 \right) + \frac{3}{5} \eta \mu_b^{kc} \right] \quad (\text{B3-4})$$

$$\mu_s^{kc*} = \frac{\rho_s \varepsilon_s g_0 \theta \mu^{kc}}{\rho_s \varepsilon_s g_0 \theta + \left(\frac{2\beta \mu^{kc}}{\rho_s \varepsilon_s} \right)}; \mu^{kc} = \frac{5}{96} \rho_s D_p \sqrt{\pi \theta}; \mu_b^{kc} = \frac{256}{5\pi} \mu^{kc} \varepsilon_s^2 g_0; \eta = (1 + e)/2 \quad (\text{B3-5})$$

$$g_0 = \frac{1}{(1 - \varepsilon_s)} + \frac{3\varepsilon_s}{2(1 - \varepsilon_s)^2} + \frac{\varepsilon_s^2}{2(1 - \varepsilon_s)^3} \quad (\text{B3-6})$$

$$\underline{\underline{\sigma}}_s^f = -p_s^f \underline{\underline{I}} + \mu_s^f \left[\nabla \underline{u}_s + \nabla \underline{u}_s^T - \frac{2}{3} (\nabla \cdot \underline{u}_s) \underline{\underline{I}} \right] \quad (\text{B3-7})$$

$$p_s^f = \begin{cases} 10^{25} (\varepsilon_s - \varepsilon_s^{max})^{10}, \varepsilon_s > \varepsilon_s^{max} \\ Fr \frac{(\varepsilon_s - \varepsilon_s^{min})^r}{(\varepsilon_s^{max} - \varepsilon_s)^s}, \varepsilon_s^{max} \geq \varepsilon_s > \varepsilon_s^{min} \\ 0, \varepsilon_s \leq \varepsilon_s^{min} \end{cases} \quad (\text{B3-8})$$

$$\mu_s^f = \frac{p_s^f \sin \delta}{\sqrt{2}} \sqrt{\frac{\mu_s^{kc}}{J_s \varepsilon_s \rho_s}} \quad (\text{B3-9})$$

Granular conductivity and collisional dissipation

$$\kappa_s = \left(\frac{\kappa_s^*}{g_0} \right) \left[\left(1 + \frac{12}{5} \eta \varepsilon_s g_0 \right) \left(1 + \frac{12}{5} \eta^2 (4\eta - 3) \varepsilon_s g_0 + \frac{64}{25\pi} (41 - 33\eta) \eta^2 (\varepsilon_s g_0)^2 \right) \right] \quad (\text{B4-1})$$

$$\kappa_s^* = \frac{\rho_s \varepsilon_s g_0 \theta \kappa}{\rho_s \varepsilon_s g_0 \theta + \left(\frac{6\beta\kappa}{5\rho_s \varepsilon_s} \right)}, \kappa = \frac{75\rho_s D_p \sqrt{\pi\theta}}{48\eta(41 - 33\eta)} \quad (\text{B4-2})$$

$$J_s = \frac{48}{\sqrt{\pi}} \eta (1 - \eta) \frac{\varepsilon_s g_0}{D_p} \theta^{3/2} \quad (\text{B4-3})$$

Turbulence interaction

$$\pi_\theta = -3\beta\theta + \frac{81\varepsilon_s \mu_g^2 |u_g - u_s|^2}{g_0 D_p^3 \rho_s \sqrt{\pi\theta}} \quad (\text{B5-1})$$

Boundary Conditions at Wall

$$\underline{n} \cdot \left(\underline{\underline{\sigma_s^{kc}}} + \underline{\underline{\sigma_s^f}} \right) \cdot \frac{\underline{u_s}}{|\underline{u_s}|} + \left(\underline{n} \cdot \underline{\underline{\sigma_s^f}} \cdot \underline{n} \right) \tan \delta_w + \frac{\pi\sqrt{3}}{6\varepsilon_s^{max}} \varphi \rho_s \varepsilon_s g_0 \sqrt{\theta} |\underline{u_s}| = 0 \quad (C1)$$

$$\underline{n} \cdot (\kappa_s \nabla \theta) = \frac{\pi\sqrt{3}}{6\varepsilon_s^{max}} \varphi \rho_s \varepsilon_s g_0 \sqrt{\theta} |\underline{u_s}|^2 - \frac{\pi\sqrt{3}}{4\varepsilon_s^{max}} (1 - e_w^2) \rho_s \varepsilon_s g_0 \theta^{\frac{3}{2}} \quad (C2)$$

$$\frac{\partial u_g}{\partial x} = - \frac{\rho_g \kappa_v C_\mu^{1/4} \sqrt{k}}{(\mu_g + \mu_g^t) \ln(Ex^*)} u_{g,x^*} = \frac{\rho_g \kappa_v C_\mu^{1/4} \sqrt{k} \Delta x / 2}{\mu_g} \quad (C3)$$

$$\frac{\partial k}{\partial x} = 0, \frac{\partial \varepsilon}{\partial x} = 0 \quad (C4)$$

$$\text{Production of } k \text{ in cell adjacent to wall} = \underline{\underline{\varepsilon_g \tau_g}} : \nabla \underline{u_g} = \varepsilon_g \rho_g \sqrt{C_\mu k} \frac{u_g}{\Delta x / 2 \ln(Ex^*)} \quad (C5)$$

$$\text{Dissipation of } k \text{ in cell adjacent to wall} = \varepsilon_g \rho_g \varepsilon = \varepsilon_g \rho_g \frac{C_\mu^{3/4} k^{3/2}}{\kappa_v \Delta x / 2} \quad (C6)$$

APPENDIX B
EXPERIMENT REPEATABILITY

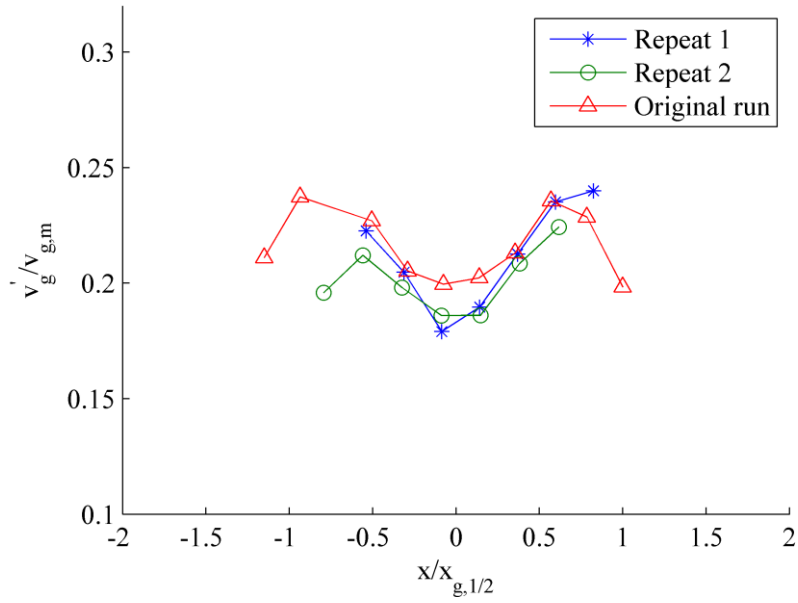


Figure B-1. Repeatability in gas fluctuating intensity at $y/D_j = 10.87$ for Case 5, $V_{fl}/V_{mf} = 1.15$.

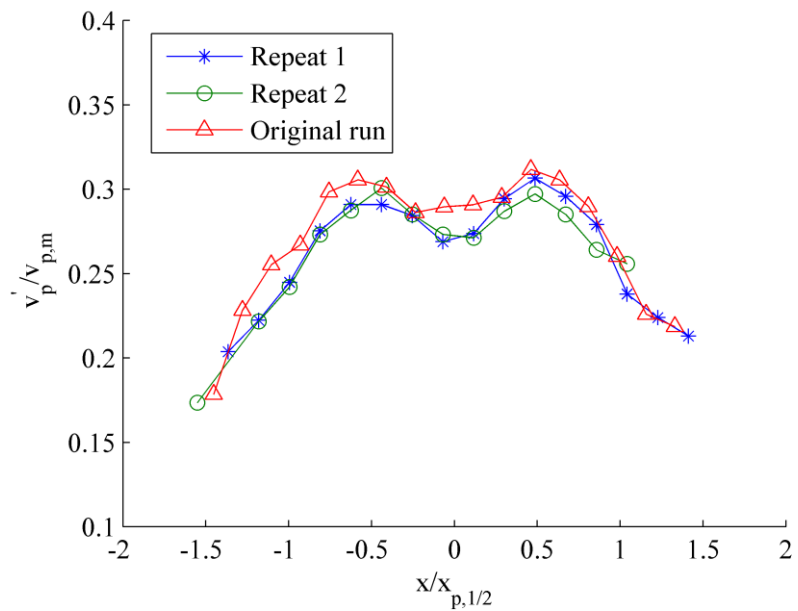


Figure B-2. Repeatability in particle fluctuating intensity at $y/D_j = 10.87$ for Case 5, $V_{fl}/V_{mf} = 1.15$.

LIST OF REFERENCES

- [1] Rhodes, M., 2008, "Introduction to Particle Technology," Second Edition, John Wiley and Sons Ltd, England.
- [2] Geldart, D., 1973, "Types of gas fluidization," *Powder Technology*, 7(5), pp. 285-292.
- [3] Li, T., Pougatch, K., Salcudean, M., and Grecov, D., 2008, "Numerical simulation of horizontal jet penetration in a three-dimensional fluidized bed," *Powder Technology*, 184(1), pp. 89-99.
- [4] Merry, J. M. D., 1971, "Penetration of a horizontal gas jet into a fluidised bed," *Transactions of the Institution of Chemical Engineers and the Chemical Engineer*, 49(4), p. 189.
- [5] Merry, J. M. D., 1975, "Penetration of vertical jets into fluidized-beds," *Aiche Journal*, 21(3), pp. 507-510.
- [6] Roach, P. E., 1993, "The penetration of jets into fluidized-beds," *Fluid Dynamics Research*, 11(5), pp. 197-216.
- [7] van Wachem, B. G. M., and Almstedt, A. E., 2003, "Methods for multiphase computational fluid dynamics," *Chemical Engineering Journal*, 96(1-3), pp. 81-98.
- [8] Sokolovski, A., 1965, *Statistics of Granular Media*, Pergamon Press, Oxford, UK.
- [9] Christakis, N., Chapelle, P., Patel, M. K., Cross, M., Bridle, I., Abou-Chakra, H., and Baxter, J., 2002, "Utilising computational fluid dynamics (CFD) for the modelling of granular material in large-scale engineering processes," *Computational Science-Iccs 2002, Pt I, Proceedings*, 2329, pp. 743-752.
- [10] Silva, M. A., and Nebra, S. A., 1997, "Numerical simulation of drying in a cyclone," *Drying Technology*, 15(6-8), pp. 1731-1741.
- [11] Gu, Z. H., Arnold, P. C., and McLean, A. G., 1992, "Prediction of the flow-rate of bulk solids from mass-flow bins with conical hoppers," *Powder Technology*, 72(2), pp. 157-166.
- [12] Detamore, M. S., Swanson, M. A., Frender, K. R., and Hrenya, C. M., 2001, "A kinetic-theory analysis of the scale-up of circulating fluidized beds," *Powder Technology*, 116(2-3), pp. 190-203.
- [13] Curtis, J. S., and van Wachem, B., 2004, "Modeling particle-laden flows: A research outlook," *Aiche Journal*, 50(11), pp. 2638-2645.
- [14] Lindborg, H., Lysberg, M., and Jakobsen, H. A., 2007, "Practical validation of the two-fluid model applied to dense gas-solid flows in fluidized beds," *Chemical Engineering Science*, 62(21), pp. 5854-5869.

- [15] T Makkawi, Y., Wright, P. C., and Ocone, R., 2006, "The effect of friction and inter-particle cohesive forces on the hydrodynamics of gas-solid flow: A comparative analysis of theoretical predictions and experiments," *Powder Technology*, 163(1-2), pp. 69-79.
- [16] van Wachem, B. G. M., Schouten, J. C., van den Bleek, C. M., Krishna, R., and Sinclair, J. L., 2001, "Comparative analysis of CFD models of dense gas-solid systems," *Aiche Journal*, 47(5), pp. 1035-1051.
- [17] Duarte, C. R., Olazar, M., Murata, V. V., and Barrozo, M. A. S., 2009, "Numerical simulation and experimental study of fluid-particle flows in a spouted bed," *Powder Technology*, 188(3), pp. 195-205.
- [18] Bettega, R., Felkl de Almeida, A. R., Correa, R. G., and Freire, J. T., 2009, "CFD modelling of a semi-cylindrical spouted bed: numerical simulation and experimental verification," *Canadian Journal of Chemical Engineering*, 87(2), pp. 177-184.
- [19] Hosseini, S. H., Ahmadi, G., Razavi, B. S., and Zhong, W., 2010, "Computational Fluid Dynamic Simulation of Hydrodynamic Behavior in a Two-Dimensional Conical Spouted Bed," *Energy & Fuels*, 24, pp. 6086-6098.
- [20] Boemer, A., Qi, H., and Renz, U., 1997, "Eulerian simulation of bubble formation at a jet in a two-dimensional fluidized bed," *International Journal of Multiphase Flow*, 23(5), pp. 927-944.
- [21] Huilin, L., Yurong, H., Wentie, L., Ding, J., Gidaspow, D., and Bouillard, J., 2004, "Computer simulations of gas–solid flow in spouted beds using kinetic–frictional stress model of granular flow," *Chemical Engineering Science*, 59(4), pp. 865-878.
- [22] Markhevka, V. I., Basov, V. A., Melik-Akhmazarov, T. K., and Orochko, D. I., 1971, "The flow of a gas jet into a fluidized bed," *Theoretical Foundation of Chemical Engineering*, 5, p.80.
- [23] Donadono, S., Maresca, A., and Massimilla, L., 1980, "Gas injection in shallow beds of fluidized, coarse solids," *Quaderni Dell Ingegnere Chimico Italiano*, 16(1-2), pp. 1-10.
- [24] Yang, W. C., and Keairns, D. L., 1980, "Momentum dissipation of and gas entrainment into a gas solid two-phase jet in a fluidized bed," *Fluidization* edited by J. R. Grace and J. M. Matsen, Plenum Press, New York, p. 305.
- [25] Ounnar, A., Arrar, J., and Bentahar, F., 2009, "Hydrodynamic behaviour of upflowing jet in fluidized bed: Velocity profiles of sand particles," *Chemical Engineering and Processing*, 48(2), pp. 617-622.

- [26] Xuereb, C., Laguerie, C., and Baron, T., 1991, "Behavior of horizontal or inclined continuous jets introduced to a fluidized-bed by a gas .2. gas velocity profiles in horizontal jets," *Powder Technology*, 64(3), pp. 271-283.
- [27] Mychkovsky, A. G., and Ceccio, S. L., 2012, "LDV measurements and analysis of gas and particulate phase velocity profiles in a vertical jet plume in a 2D bubbling fluidized bed Part III: The effect of fluidization," *Powder Technology*, 220(0), pp. 37-46.
- [28] Dong, X. F., Yu, A. B., Yagi, J. I., and Zulli, P., 2007, "Modelling of multiphase flow in a blast furnace: Recent developments and future work," *Isij International*, 47(11), pp. 1553-1570.
- [29] Shen, Y. S., Guo, B. Y., Yu, A. B., Austin, P. R., and Zulli, P., 2011, "Three-dimensional modelling of in-furnace coal/coke combustion in a blast furnace," *Fuel*, 90(2), pp. 728-738.
- [30] Rajneesh, S., Sarkar, S., and Gupta, G. S., 2004, "Prediction of raceway size in blast furnace from two dimensional experimental correlations," *Isij International*, 44(8), pp. 1298-1307.
- [31] Filla, M., Massimilla, L., and Vaccaro, S., 1983, "Gas jets in fluidized-beds and spouts - a comparison of experimental behavior and models," *Canadian Journal of Chemical Engineering*, 61(3), pp. 370-376.
- [32] Mychkovsky, A., Rangarajan, D., and Ceccio, S., 2012, "LDV measurements and analysis of gas and particulate phase velocity profiles in a vertical jet plume in a 2D bubbling fluidized bed: Part I: A two-phase LDV measurement technique," *Powder Technology*, 220(0), pp. 55-62.
- [33] Miller, D. R., and Comings, E. W., 1957, "Static pressure distribution in the free turbulent jet," *Journal of Fluid Mechanics*, 3(1), pp. 1-16.
- [34] Gutmark, E., and Wygnanski, I., 1976, "Planar turbulent jet," *Journal of Fluid Mechanics*, 73(FEB10), pp. 465-495.
- [35] Hetsroni, G., 1989, "Particles turbulence interaction," *International Journal of Multiphase Flow*, 15(5), pp. 735-746.
- [36] Mychkovsky, A. G., 2010, "LDV Measurements and Analysis of Gas and Particulate Phase Velocity Profiles in a Vertical Jet Plume in a 2D Bubbling Fluidized Bed," PhD, University of Michigan, Ann Arbor.
- [37] Rangarajan, D., Mychkovsky, A. G., Curtis, J. S., and Ceccio, S. L., 2012, "Effect of emulsion fluidization state on the fluctuations in gas and particle velocities inside the plume of a gas jet penetrating a fluidized bed," *Powder Technology*, submitted.

- [38] Heskestad, G, 1965, "Hot-wire measurements in a plane turbulent jet," *Journal of Applied Mechanics*, 32(4), p. 721.
- [39] Bradbury, L. J., 1965, "Structure of a self-preserving turbulent plane jet," *Journal of Fluid Mechanics*, 23, p. 31.
- [40] Everitt, K. W., and Robins, A. G., 1978, "Development and structure of turbulent plane jets," *Journal of Fluid Mechanics*, 88(OCT), pp. 563-583.
- [41] Browne, L. W. B., Antonia, R. A., and Chambers, A. J., 1984, "The interaction region of a turbulent plane jet," *Journal of Fluid Mechanics*, 149(DEC), pp. 355-373.
- [42] Bradshaw, P., 1966, "Effect of initial conditions on development of a free shear layer," *Journal of Fluid Mechanics*, 26, p. 225.
- [43] Bradshaw, P., 1977, "Effect of external disturbances on spreading rate of a plane turbulent jet," *Journal of Fluid Mechanics*, 80(MAY23), pp. 795-797.
- [44] George, W. K., and Davidson, L., 2004, "Role of initial conditions in establishing asymptotic flow behavior," *Aiaa Journal*, 42(3), pp. 438-446.
- [45] Deo, R. C., Mi, J., and Nathan, G. J., 2008, "The influence of Reynolds number on a plane jet," *Physics of Fluids*, 20(7), p. 075108.
- [46] Hitchman, G. J., Strong, A. B., Slawson, P. R., and Ray, G. D., 1990, "Turbulent plane jet with and without confining end walls," *Aiaa Journal*, 28(10), pp. 1699-1700.
- [47] Alnahhal, M., and Panidis, T., 2009, "The effect of sidewalls on rectangular jets," *Experimental Thermal and Fluid Science*, 33(5), pp. 838-851.
- [48] Krothapalli, A., Baganoff, D., and Karamcheti, K., 1981, "On the mixing of a rectangular jet," *Journal of Fluid Mechanics*, 107(JUN), pp. 201-220.
- [49] Deo, R. C., Mi, J., and Nathan, G. J., 2007, "The influence of nozzle aspect ratio on plane jets," *Experimental Thermal and Fluid Science*, 31(8), pp. 825-838.
- [50] Rodi, W., 1982, "Examples of turbulence models for incompressible flows," *Aiaa Journal*, 20(7), pp. 872-879.
- [51] Syamlal, M., Rogers, W., and O'Brien, T. J., 1993, "MFIx Documentation: Theory Guide," U.S. Department of Energy.
- [52] Openfoam, "www.openfoam.org".
- [53] Wilcox, D. C., 1988, "Reassessment of the scale-determining equation for advanced turbulence models," *Aiaa Journal*, 26(11), pp. 1299-1310.

- [54] Launder, B. E., Reece, G. J., and Rodi, W., 1975, "Progress in development of a reynolds-stress turbulence closure," *Journal of Fluid Mechanics*, 68(APR15), pp. 537-566.
- [55] Patankar, S. V., 1980, *Numerical Heat Transfer and Fluid Flow*, Hemisphere Publishing Corporation, New York.
- [56] Acosta-Iborra, A., Sobrino, C., Hernandez-Jimenez, F., and de Vega, M., 2011, "Experimental and computational study on the bubble behavior in a 3-D fluidized bed," *Chemical Engineering Science*, 66(15), pp. 3499-3512.
- [57] Johansson, K., van Wachem, B. G. M., and Almstedt, A. E., 2006, "Experimental validation of CFD models for fluidized beds: Influence of particle stress models, gas phase compressibility and air inflow models," *Chemical Engineering Science*, 61(5), pp. 1705-1717.
- [58] Santos, K. G., Murata, V. V., and Barrozo, M. A. S., 2009, "Three-dimensional computational fluid dynamics modelling of spouted bed," *Canadian Journal of Chemical Engineering*, 87(2), pp. 211-219.
- [59] Gryczka, O., Heinrich, S., Deen, N. G., Annaland, M. v. S., Kuipers, J. A. M., Jacob, M., and Moerl, L., 2009, "Characterization and CFD-modeling of the hydrodynamics of a prismatic spouted bed apparatus," *Chemical Engineering Science*, 64(14), pp. 3352-3375.
- [60] Wu, Z., and Mujumdar, A. S., 2008, "CFD modeling of the gas-particle flow behavior in spouted beds," *Powder Technology*, 183(2), pp. 260-272.
- [61] Wang, Z., Bi, H. T., and Lim, C. J., 2010, "CFD Simulation of Spouted Beds Using a Pressure Source Term," *Industrial & Engineering Chemistry Research*, 49(11), pp. 5053-5060.
- [62] Patil, D. J., Annaland, M. V., and Kuipers, J. A. M., 2005, "Critical comparison of hydrodynamic models for gas-solid fluidized beds - Part I: bubbling gas-solid fluidized beds operated with a jet," *Chemical Engineering Science*, 60(1), pp. 57-72.
- [63] Li, T., Pougatch, K., Salcudean, M., and Grecov, D., 2009, "Numerical simulation of single and multiple gas jets in bubbling fluidized beds," *Chemical Engineering Science*, 64(23), pp. 4884-4898.
- [64] Anderson, T. B., and Jackson, R., 1967, "A fluid mechanical description of fluidized beds," *Industrial & Engineering Chemistry Fundamentals*, 6(4), p. 527.
- [65] Wen, C. Y., and Yu, Y. H., 1966, "Mechanics of fluidization," *Chemical Engineering Progress Symposium Series*, 62(62) pp. 100-111.

- [66] Srivastava, A., and Sundaresan, S., 2003, "Analysis of a fractional-kinetic model for gas-particle flow," *Powder Technology*, 129(1-3), pp. 72-85.
- [67] Rao, A., Curtis, J. S., Hancock, B. C., and Wassgren, C., 2012, "Numerical simulation of dilute turbulent gas-particle flow with turbulence modulation," *Aiche Journal*, 58(5), pp. 1381-1396.
- [68] Bolio, E. J., Yasuna, J. A., and Sinclair, J. L., 1995, "Dilute turbulent gas-solid flow in risers with particle-particle interactions," *Aiche Journal*, 41(6), pp. 1375-1388.
- [69] Benyahia, S., Syamlal, M., and O'Brien, T. J., 2007, "Study of the ability of multiphase continuum models to predict core-annulus flow," *Aiche Journal*, 53(10), pp. 2549-2568.
- [70] Benyahia, S., Syamlal, M., and O'Brien, T. J., 2005, "Evaluation of boundary conditions used to model dilute, turbulent gas/solids flows in a pipe," *Powder Technology*, 156(2-3), pp. 62-72.
- [71] Simonin, O., 1996, "Continuum modeling of dispersed two-phase flows in combustion and turbulence in two-phase Flows," Von Karman Institute of Fluid Dynamics Lecture Series.
- [72] Lun, C. K. K., Savage, S. B., Jeffrey, D. J., and Chepuruiy, N., 1984, "Kinetic theories for granular flow - inelastic particles in couette-flow and slightly inelastic particles in a general flowfield," *Journal of Fluid Mechanics*, 140(MAR), pp. 223-256.
- [73] Agrawal, K., Loezos, P. N., Syamlal, M., and Sundaresan, S., 2001, "The role of meso-scale structures in rapid gas-solid flows," *Journal of Fluid Mechanics*, 445, pp. 151-185.
- [74] Reuge, N., Cadoret, L., Coufort-Saudejaud, C., Pannala, S., Syamlal, M., and Caussat, B., 2008, "Multifluid Eulerian modeling of dense gas-solids fluidized bed hydrodynamics: Influence of the dissipation parameters," *Chemical Engineering Science*, 63(22), pp. 5540-5551.
- [75] Carnahan, N. F., and Starling, K. E., 1969, "Equation of state for nonattracting rigid spheres," *Journal of Chemical Physics*, 51(2), pp. 635.
- [76] Benyahia, S., 2008, "Validation Study of Two Continuum Granular Frictional Flow Theories," *Industrial & Engineering Chemistry Research*, 47(22), pp. 8926-8932.
- [77] Patil, D. J., Annaland, A. V., and Kuipers, J. A. M., 2005, "Critical comparison of hydrodynamic models for gas-solid fluidized beds - Part II: freely bubbling gas-solid fluidized beds," *Chemical Engineering Science*, 60(1), pp. 73-84.

- [78] Passalacqua, A., and Marmo, L., 2009, "A critical comparison of frictional stress models applied to the simulation of bubbling fluidized beds," *Chemical Engineering Science*, 64(12), pp. 2795-2806.
- [79] Johnson, P. C., Nott, P., and Jackson, R., 1990, "Frictional collisional equations of motion for particulate flows and their application to chutes," *Journal of Fluid Mechanics*, 210, pp. 501-535.
- [80] Schaeffer, D. G., 1987, "Instability in the evolution equations describing incompressible granular flow," *Journal of Differential Equations*, 66, pp. 19-50.
- [81] Savage, S. B., 1998, "Analyses of slow high-concentration flows of granular materials," *Journal of Fluid Mechanics*, 377, pp. 1-26.
- [82] Louge, M. Y., Mastorakos, E., and Jenkins, J. T., 1991, "The role of particle collisions in pneumatic transport," *Journal of Fluid Mechanics*, 231, pp. 345-359.
- [83] Crowe, C. T., 2000, "On models for turbulence modulation in fluid-particle flows," *International Journal of Multiphase Flow*, 26(5), pp. 719-727.
- [84] Sinclair, J., and Mallo, T., 1998, "Describing particle-turbulence interaction in a two-fluid modeling framework," *ASME Fluids Engineering Division Summer Meeting*, ASME Press, New York, NY, pp. 7-12.
- [85] Koch, D. L., and Sangani, A. S., 1999, "Particle pressure and marginal stability limits for a homogeneous monodisperse gas-fluidized bed: kinetic theory and numerical simulations," *Journal of Fluid Mechanics*, 400, pp. 229-263.
- [86] Johnson, P. C., and Jackson, R., 1987, "Frictional collisional constitutive relations for antigranulocytes-materials, with application to plane shearing," *Journal of Fluid Mechanics*, 176, pp. 67-93.
- [87] Benyahia, S., Syamlal, M., and O'Brien, T. J., 2006, "Summary of MFIX Equations Version 2005-4."
- [88] Mychkovsky, A. G., and Ceccio, S. L., 2012, "LDV measurements and analysis of gas and particulate phase velocity profiles in a vertical jet plume in a 2D bubbling fluidized bed Part II: Mass and momentum transport," *Powder Technology*, 220(0), pp. 47-54.
- [89] Jones, E. N., 2001, "An experimental investigation of particle size distribution effects in gas-solid flow," PhD, Purdue University, Purdue, IN.
- [90] Liao, J., Mei, R., and Klausner, J. F., 2008, "A study on the numerical stability of the two-fluid model near ill-posedness," *International Journal of Multiphase Flow*, 34(11), pp. 1067-1087.

- [91] Lun, C. K. K., 2000, "Numerical simulation of dilute turbulent gas-solid flows," *International Journal of Multiphase Flow*, 26(10), pp. 1707-1736.
- [92] Gore, R. A., and Crowe, C. T., 1989, "Effect of particle-size on modulating turbulent intensity," *International Journal of Multiphase Flow*, 15(2), pp. 279-285.
- [93] Rangarajan, D., and Curtis, J. S., 2012, "The Effect of Spanwise Width on Rectangular Jets With Sidewalls," *Journal of Fluids Engineering*, 134(3), p. 031202.
- [94] Flint, P. J., and Burgess, J. M., 1992, "A fundamental-study of raceway size in 2 dimensions," *Metallurgical Transactions B-Process Metallurgy*, 23(3), pp. 267-283.
- [95] Gupta, G. S., Rajneesh, S., Rudolph, V., Singh, V., Sarkar, S., and Litster, J. D., 2005, "Mechanics of raceway hysteresis in a packed bed," *Metallurgical and Materials Transactions B-Process Metallurgy and Materials Processing Science*, 36(6), pp. 755-764.
- [96] Sastry, G., Gupta, G. S., and Lahiri, A. K., 2003, "Void formation and breaking in a packed bed," *Isij International*, 43(2), pp. 153-160.
- [97] Xu, B. H., Yu, A. B., Chew, S. J., and Zulli, P., 2000, "Numerical simulation of the gas-solid flow in a bed with lateral gas blasting," *Powder Technology*, 109(1-3), pp. 13-26.
- [98] Yu, A. B., and Xu, B. H., 2003, "Particle-scale modelling of gas-solid flow in fluidisation," *Journal of Chemical Technology and Biotechnology*, 78(2-3), p. 111.
- [99] Nogami, H., Yamaoka, H., and Takatani, K., 2004, "Raceway design for the innovative blast furnace," *Isij International*, 44(12), pp. 2150-2158.
- [100] Yuu, S., Umekage, T., and Miyahara, T., 2005, "Prediction of stable and unstable flows in blast furnace raceway using numerical simulation methods for gas and particles," *Isij International*, 45(10), pp. 1406-1415.
- [101] Feng, Y. Q., Pinson, D., Yu, A. B., Chew, S. J., and Zulli, P., 2003, "Numerical study of gas-solid flow in the raceway of a blast furnace," *Steel Research International*, 74(9), pp. 523-530.
- [102] Aoki, H., Nogami, H., Tsuge, H., Miura, T., and Furukawa, T., 1993, "Simulation of transport phenomena around the raceway zone in the blast-furnace with and without pulverized coal injection," *Isij International*, 33(6), pp. 646-654.
- [103] Mondal, S. S., Som, S. K., and Dash, S. K., 2005, "Numerical predictions on the influences of the air blast velocity, initial bed porosity and bed height on the shape and size of raceway zone in a blast furnace," *Journal of Physics D-Applied Physics*, 38(8), pp. 1301-1307.

- [104] Sarkar, S., Gupta, G. S., and Kitamura, S. Y., 2007, "Prediction of raceway shape and size," *Isij International*, 47(12), pp. 1738-1744.
- [105] Gupta, G., and Rudolph, V., 2006, "Comparison of blast furnace raceway size with theory," *Isij International*, 46(2), pp. 195-201.
- [106] Pinson, D., Shaw, J., Yu, A. B., McCarthy, M., and Zulli, P., 1999, "An experimental study of gas-solid flow in the blast furnace raceway," *Chemeca 99Newcastle*, pp. 192-197.
- [107] Shen, Y. S., Maldonado, D., Guo, B. Y., Yu, A. B., Austin, P., and Zulli, P., 2009, "Computational Fluid Dynamics Study of Pulverized Coal Combustion in Blast Furnace Raceway," *Industrial & Engineering Chemistry Research*, 48(23), pp. 10314-10323.
- [108] Shen, Y. S., Yu, A. B., Austin, P. R., and Zulli, P., 2012, "CFD study of in-furnace phenomena of pulverised coal injection in blast furnace: Effects of operating conditions," *Powder Technology*, 223(0), pp. 27-38.

BIOGRAPHICAL SKETCH

Deepak Rangarajan was born in the year 1986 in Chennai, India. He did his schooling at Padma Seshadri Bala Bhavan, Chennai and went on to earn his bachelor's degree in chemical engineering at the National Institute of Technology, Tiruchirappalli in 2008. He then enrolled at the University of Florida to pursue graduate studies in chemical engineering.